High Resolution Imaging of Photonic Crystals

A diploma thesis (Diplomarbeit) submitted to the
UNIVERSITY OF CONSTANCE

for the degree of
Diploma Physicist (Diplom Physiker)

presented by

Wolfgang Stumpf

born April 20th, 1976
German citizen

accepted on the recommendation of:
Professor Dr. Elke Scheer, examiner
Privatdozent Dr. Peter Marzlin, co–examiner
Professor Dr. Vahid Sandoghdar, ext. examiner

February 2004

The experimental work and the writing of this diploma thesis was performed in 2003 at the Swiss Federal Institute of Technology Zürich to gain the degree of diploma physicist at the University of Constance, Germany.

Dedicated to Uwe Dreger

Abstract

The light propagation inside photonic crystals has a strong similarity to the wave propagation of a conducting electron in a crystalline solid. Photonic crystals are structures with a spatial periodically modulated refractive index. The length scale of the modulation is of the same order as the wavelength of light. Given a sufficient index contrast, Bragg–like diffraction prohibits certain propagation directions and photon frequency ranges.

The localization of light at lattice defects allows one to integrate optic devices on a small scale due to the sub–wavelength scale of the defects. For example line defects may be used to form waveguides and point defects can form frequency selective filters.

Regular microscopy images the light that scatters away from some sample. It is limited by diffraction to a resolution of half a wavelength and cannot reveal the detailed patterns of light confinement in photonic crystal defects.

In the scope of a diploma thesis, scanning near–field optical microscopy has been used on two different photonic crystal types, provided by two collaborating research groups. Images have been taken with sub–diffraction limited resolution. The data was used to study the transmission of photonic crystal junctions and to visualize the changing of optical modes in a photonic waveguide as a function of wavelength.

Contents

Chapter 1

Introduction

> *"[...] Although the NSOM enjoys many of the advantages of conventional optical microscopy [...], ironically it has replaced the instant integrity of microscopically aided eyesight with a myopic groping, collecting information in a spot–by–spot manner [...]"*
>
> From [1], "The Near–Field Scanning Optical Microscope"

What is generally known as optical microscopy has its origin in the 16th century and has experienced a large number of modifications and improvements to this day. The spatial resolution can be increased but it is theoretically limited by the notorious Abbé diffraction limit. Scanning near–field optical microscopy (SNOM/NSOM[1]) offers the ability to overcome that limit. There are numerous motivations to increase imaging resolution. Today's technology deals with smallest integration in different kind of systems for example electrical, optical, fluidic (gases and liquids) integrated circuits (IC) and their combinations. The decreasing length scale requires improved and new fabrication methods. An outstanding example for this is lithography for computer chip industry. Research in life sciences[2] also benefits from higher resolution in fluorescence microscopy. Photonic crystals (PHC) are artificially fabricated and are able to confine and guide light in structures which are smaller than the photon's wavelength. That way they are first choice for applications in integrated optics on a small scale. From taking advantage of the high spatial, sub–wavelength resolution of SNOM, the field pattern, phase, light propagation and confinement properties of artificial defects inside a PHC and therefore the crystal quality itself can be measured. This is very important to study the crystal properties and the tolerance range in the fabrication process with regard to the light guiding properties. Furthermore, the light propagation in a PHC device can be simulated by numerical models and compared to experimental results.

The structure of this work is given by the following short survey of the contents for each chapter, followed on the next page.

---

[1] The two different acronyms in the literature have the reason that in two different research groups, D. W. Pohl at the IBM Research Lab in Zürich, Switzerland and A. Lewis at U.S. Cornell University attended to the issue at the same time without being aware of each other. Basically the order of the letters should emphasize as well the scanning probe technique as the near–field aspect. Here, throughout this work the term SNOM will be used for the sake of simplicity.

[2] In recent years, this name came up for science related to biology, explicitly setting in focus life itself. It merges aspects of the classical disciplines and stresses the overlap of biology, chemistry, medicine and ecology in research, engineering and technology.

- Chapter two gives a historical introduction of the development of microscopy from the first microscopes to scanning probe microscopy and scanning near–field optical microscopy. Its principle and instrumentation is explained and also advantages of near–field optics compared to far–field imaging. It also gives an insight into different techniques and operational modes. A theoretical model for near–field imaging is adumbrated and the issue of resolution elucidated.
- In chapter three, photonic crystals are introduced. The evolution and the principle is elucidated. The theoretical treatment by electromagnetism and the analogy to terms in solid state physics is presented. The concept of the reciprocal lattice is explained an linked to the photonic band structure heading to the photonic Bloch states. Finally the photonic crystals are classified by their dimensionality, the purpose of defect structures elucidated and the investigation by scanning near–field optical microscopy motivated. Additional basics on crystal matter are given in the appendix. Finally the basics of the finite–difference time domain simulation are sketched.
- The fourth chapter starts with probe fabrication for scanning near–field optical microscopy and shows different aspects of the fabrication. Photonic crystals of different material and design are presented and their fabrication process explained. The investigations of both using scanning near–field optical microscopy is given in detail, followed by an analysis and discussion.
- The appendices deal with the Miller indices, artifacts in SNOM imaging, and technical details of the devices. Finally an example for a program that was written for data analysis is given.

Chapter 2

Microscopy

It is quite valuable to have a look back at the history of optical imaging and its development [2] starting from the very simple, up to sophisticated state of the art devices. Some are employed in daily life use, whereas others only become valuable in high end applications. In all cases every microscope has a radiating object and an imaging device to form an image on a screen or eye. But the way it is done depends strongly on the application's purpose.

2.1 Historical background

2.1.1 Imaging and microscopy

The oldest lens is estimated to be 3000 years old and was excavated in the palace of Nimrud in what is nowadays Iraq by the archeologist John Layard in 1850 [3]. Regrettably there is only speculation upon its use.

The Roman writer Gajus Plinius (23–79 AD) mentioned that he had noticed the effect of enlargement by a water filled glass sphere, but without any hint how to use this. Much later the work "Kitab–al–Manazir", in English "The treasure of optics", written by the Arab scientist Abu Ali al–Hasan ibn al–Haitham (965–1039 AD) was fundamental. In literature the author's name is also referred to Alhazen. In his work he reported on the magnifying properties of shaped glass. Based on translations of his scripts, handcraft skilled monks made plano–convex lenses some hundred years later.[1] The scientist Roger Bacon (1214–1294) carried out systematic observations and proposed the use of lenses for magnification to aid natural vision [2].

The further development of lenses brought up spectacles in the end of the 13th century and the first microscopes in the end of the 16th century. Robert Hooke (1635–1703) and Antonie van Leeuwenhoek (1630–1723) are regarded as outstanding persons in this progress. In the beginning, microscopes were used to satisfy curiosity about the surroundings and the revealed fine structure of the objects. By offering the possibility of a detailed analysis, microscopes quickly found their way into many fields of science: This technique allowed to visualize objects on a small length scale and therefore led to important discoveries like biological micro–organisms, organic cells or Brownian motion.

By–and–by the lens–type microscopes spread out in a wide range of application fields and resolution became increasingly better, because of upgrades and improvements over the years. Figure 2.1 by D. W. Pohl in [4] gives a sense for the historical development of spatial resolution. A definition for this term will be given in section 2.2.3.

The hope to improve resolution ad infinitum was dashed in 1873, when E. Abbé published his famous work on the resolution limit of optical imaging dependent from the light wavelength λ and the numerical aperture NA [5]. The development of quantum mechanics and the thereby related concept of matter waves for massive particles that have smaller wavelength than the visible light

---

[1] A finding of aspheric bi–convex lenses in recent years in Gotland, Sweden is very interesting, because these so–called Visby lenses originate from the Viking era on the brink of the 11th century but their source and fabrication is not totally clear and leaves many questions open. It seems that the craft knowledge was lost for at least 500 years and even when the philosopher Descartes calculated the ideal focussing lens shape — he was not able to produce it.

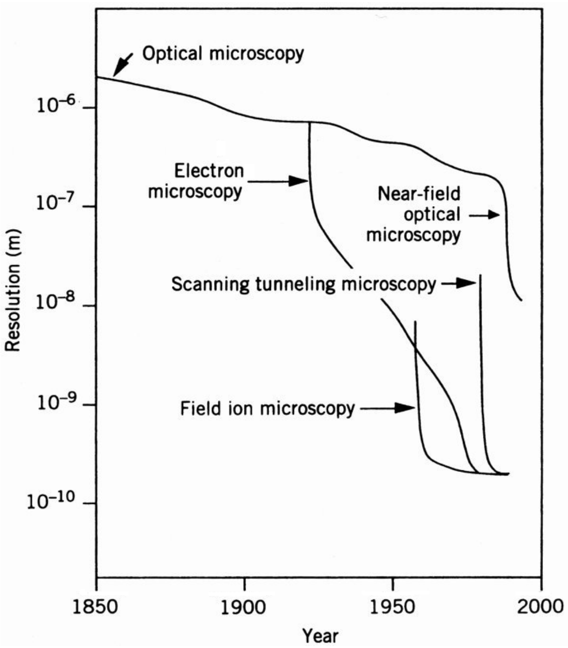

Figure 2.1: The development of spatial resolution for different microscope techniques (taken from [4]).

nevertheless pushed the spatial resolution below one nanometer. Nowadays electron microscopy has become a standard technique in terms of scanning electron microscopy (SEM) and (scanning) transmission electron microscopy ((S)TEM). A drawback of the smaller wavelength is according to the matter wave concept the higher energies and therefore possible destructive impacts on the sample. Besides the fact that the particle techniques have to be performed under vacuum conditions in the millibar regime and below what evidently inhibits for instance in vivo studies. Another limitation of the electron microscope (EM) is, that the NA is often quite small due to the difficulty of making electron optics.

Thus, in summary, there are several possibilities for imaging: One of it is fundamentally limited by the use of lenses, parallel aligned to the object of interest. In this case to cope with the required higher and higher resolution other particles than photons can be used. The collection of the image data can be done serially by scanning. Another possibility is to transduce a signal in the extreme close vicinity of an object where diffraction is no limit. More details and thorough treatments of the topic are reported elsewhere [1, 4, 6–11].

2.1.2 Scanning probe microscopy

A scanning probe microscope (SPM) offers the advantage of non–destructive and low energy processes[2] and can therefore be used for detection and manipulation of individual particles like molecules or atoms. In all cases of scanning probe microscopy[3] a sharp probe or tip is raster scanned over a sample's region of interest. The scan is performed by a precise[4] piezoelectric transducer. The transducer position is controlled using computer software that also allows the collection of a variety of parameters that may vary as a function of tip position. The probe interacts with a local surface field that can be of a different nature for each kind of SPM. One of the SPMs is

---

[2] Nevertheless the probe is a local perturbation that drastically changes boundary conditions and manipulates the particle, but in a controllable way in contrary to just bombing it with smaller particles of high energy in comparison with an electron microscope.

[3] Various operation modes and interaction types exist e.g. tapping, FMM, EFM, MFM etc.

[4] According to specs of the manufacturer [12] down to 1/100 nm, but the resolution of the piezo is limited by the noise characteristics of the driving electronics.

the scanning tunnelling microscope (STM), which has been invented in 1982 by G. Binnig and H. Rohrer [13, 14]. The STM is able to image the surface of conducting materials by a continuous adjustment of the height of the probe to maintain a constant tunnelling current between the probe and the surface.

A SPM that exploits the mechanical nature of the local interaction is the atomic force microscope (AFM) that arrived in 1986 [15]. Here, the amplitude of a very sharp probe is measured as it is repelled or attracted to the surface due to the van der Waals force. Both types of microscopes reveal details on atomic scale and offer the opportunity to detect individual particles and manipulate them [16, 17].

Another SPM is the scanning near–field optical microscope (SNOM). An evanescent optical field which contains high spatial frequencies is probed at the surface. Unlike STM and AFM, SNOM does not seek to measure topography (A separate mechanism is required to control the tip–sample distance which will be discussed in section 2.2.1), instead it measures the strength of an optical field at a surface. It is this technique of great interest to the imaging of PHCs.

2.2 Scanning near–field optical microscopy

Scanning near–field optical microscopy was simultaneously developed in two different research groups. These are the groups of D.W. Pohl [18] at the IBM Research Lab in Zürich, Switzerland and A. Lewis [19, 20] at Cornell University in the United States of America.

Already in 1928 A. Einstein and E. H. Synge discussed an instrument remarkably similar to what is known today as SNOM in a number of letters that were uncovered and published in 1990 by D. McMullan [21]. Synge himself published his ideas [22, 23] of the very first intuition of SNOM in 1928. Later in 1972, the first successful near–field key experiment in the microwave range[5] was performed by E. Ash and G. Nicholls [24]. As one can see, all these early ideas were gradually rediscovered and a series of technical developments lead to the state–of–the–art SNOM. A number of other instruments for near–field optics (NFO) are discussed in [1]: The evanescent wave microscope [25], the frustrated total internal reflection (FTIR) microscope [26], the photon tunnelling microscope (PTM) [27, 28] and the photon scanning tunnelling microscope (PSTM) [29, 30]. These alternative forms of microscopy were developed from the viewpoint to overcome Abbé's far–field diffraction limit and to exploit the near–field optics. SNOM is unique, because it takes advantage of both scanning probe and optical microscopy. Its reliability also depends on a stable tip–sample distance regulation. For that purpose there was a real breakthrough due to the contribution in 1992 by R. Toledo–Crow *et al.* [31] and E. Betzig *et al.* [32] by introduction of the shear–force feedback. In series, a startling report in terms of detection and manipulation smallest particles was about single fluorescent molecule detection at room temperature in 1993 [33]. An overview on different configurations and detection principles as well as probe design concepts during the last decades can be found in [1]. In the scope of this thesis only a few relevant subjects can be touched on. SNOM itself is used in a large field of applications [34], e.g. the analysis of optical properties of materials, surface chemistry, single molecule detection and spectroscopy, lithography, data recording or biologic applications (cells, DNA).

2.2.1 Principle

Indicated as above, a probe is raster scanned relative to the sample and close to its surface (shear–force is typically detected at ≈ 5–20 nm [6]) by means of piezoelectric transducers. The scanning speed has to be chosen appropriate to the system specification, i.e. the system response has to be sufficiently fast, because it is favorable to preserve the probe. The distinction between different operation modes will follow. The scanning speed is usually in the order of a few micron per second[6].

The system used for distance control is depicted in figure 2.2. The lock-in amplifier ensures fast response because of its phase shift sensitivity [34, 35]. Working principle is, that the probe tracks

---

[5] The sub–wavelength resolution was approximately $\lambda/60$ in reference to the period of the imaging wavelength.

[6] In other words: For typical scan parameters of scan speed and pixel size it would take approximately 2 months to record an image of 1 mm^2 what restricts SNOM to fields where it is necessary to have an ultrahigh resolution.

the surface because the signal is fed back in a loop to control the dithering amplitude of the probe respectively the phase shift caused by the damping. The piezo voltage is used to form an image of the surface topography. The same can be done with the looped–back signal coming from the probe leading to a shear–force image [36]. A possible damage of the probe can be seen as a change in the shear–force image, and therefore also in the topography which depends on the feedback.

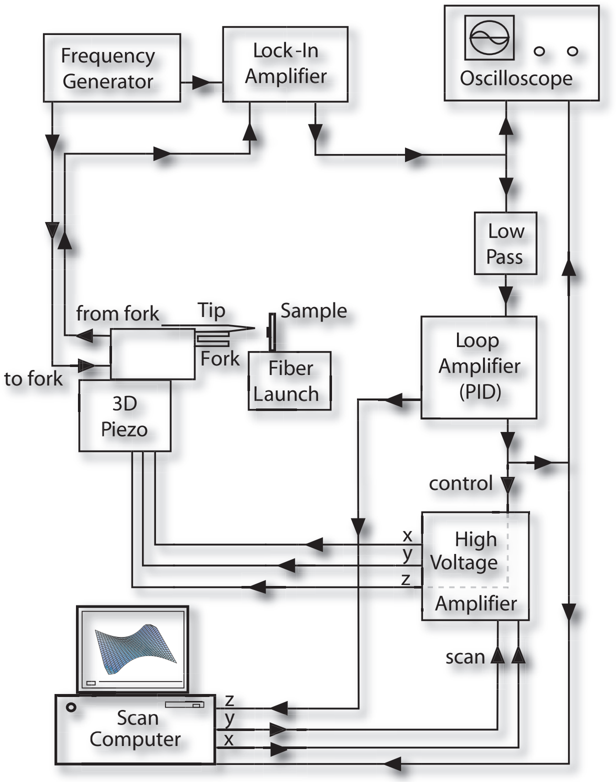

Figure 2.2: Schematic draw of the servo–loop for distance control. Details on the devices are given in appendix C. The self–capacitance of the quartz tuning fork was compensated by a circuit, based on [37, 38].

There is a huge variety of SNOM configurations in the literature distinguished by various adjectives (For an example see 2.3). Additional modes (apertureless, fluorescence) are decribed in [11]. There are combinations of the different modes as well as the different techniques [39].

The sample is considered to be illuminated by some means. Neglecting absorption, the incident light is diffracted on the surface either transmitted or reflected. In *very* close vicinity to the surface there is a non–propagating near–field that consists of an exponentially decaying evanescent field i.e. the high spatial frequencies components of the diffracted light. This light can not be imaged in the field, which is the origin of Abbé's limit. A local probe can, however, scatter light from the surface into the far–field. In this way, the SNOM probe allows visualization of the high spatial frequency field components that normally stay hidden. Thus, the optical image information is achieved, where the optical contrast is directly linked to the strength of the field at the sample surface [40]. Details on the analysis can be found in [41]. Two points turn out to be crucial: First, a finer probe leads on the one hand to a higher resolution, but on the other hand the signal becomes weaker. The aperture acts like a pinhole/Fourier filter i.e. the smaller it is, the higher the spatial frequencies become that can be scattered (and transmitted). Thus, the size of the aperture has to be appropriate. Second, because of the exponential decay of the evanescent field, the probe has come as close as possible to the surface to detect the high spatial frequency components. Therefore,

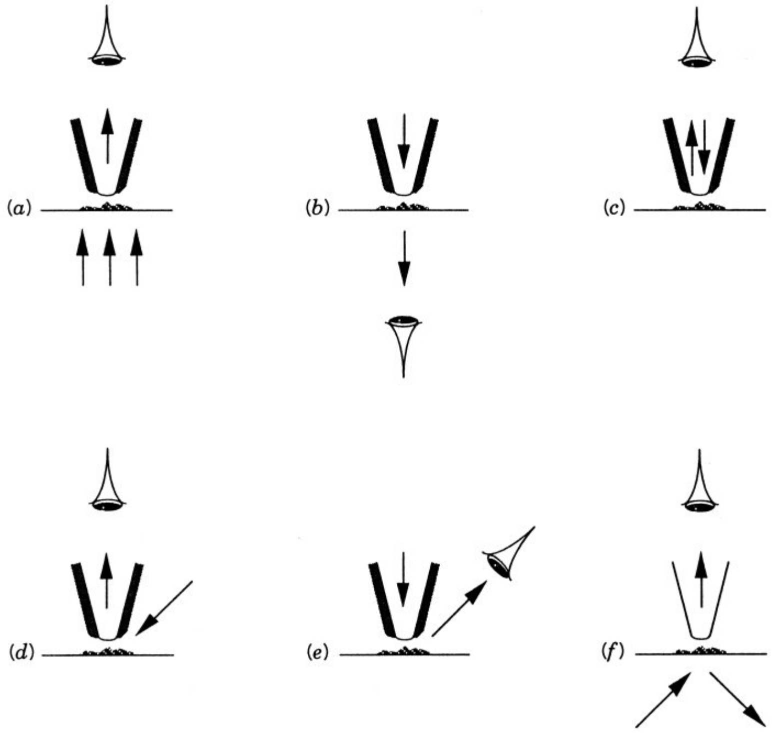

Figure 2.3: Example for different common illumination principles in SNOM, which are described as (a) collection; (b) illumination; (c) collection/illumination; (d) oblique collection; (e) oblique illumination; and (f) dark field (taken from [1]).

the aperture diameter w of the probe requires

$$w \ll z \ll \lambda, \tag{2.1}$$

where z denotes the probe – sample distance. The definition of the term near–field depends on the characterization i.e. for example multipole fields and radiation, antenna theory or microcavities. That is why the following definition is reasonable:

NFO is a branch of optics that considers configurations that depend on the passage of light to, from, through, or near an element with sub–λ features and the coupling of light to a second element located at sub–λ distance from the first [1].

The exact imaging mechanism in SNOM has been and will be still a challenge either for theorists and experimentalists. A 2D scalar model is often used to show the theoretical basics. This concept was introduced by Massey [42], extended by Vigoureux, Depasse and Girard [43, 44], and is discussed in the book of Paesler and Moyer [1]. In short, the field at the aperture from an object (here for example a double slit, formed by an opaque plane with slits of widths $2L$ separated by $2d$) at a certain distance z can be written as

$$f\,(x, z)\,|_{z=0} = E_0\,(\mathrm{rect}\,[-d-L, -d+L] + \mathrm{rect}\,[d-L, d+L]\,), \tag{2.2}$$

where the function $\mathrm{rect}\,[a, b] = 1$ for $a < x < b$ and is 0 elsewhere, is introduced which simplifies the calculation. The function f from (2.2), transformed into Fourier frequency space reads:

$$F\,(k_x, z)\,|_{z=0} = 4\,E_0\cos(k_x d)\frac{\sin(k_x L)}{k_x L}. \tag{2.3}$$

The result, put into the transfer function:

$$
\begin{aligned}
f(x,z) &= \frac{1}{2\pi}\int_{-\infty}^{+\infty} e^{-ik_x x}\, F(k_x,z)\,|_{z=0}\, e^{-iz\sqrt{k_0^2-k_x^2}}\, dk_x \qquad \text{for } k_0^2 > k_x^2 \text{ and} \\
f(x,z) &= \frac{1}{2\pi}\int_{-\infty}^{+\infty} e^{-ik_x x}\, F(k_x,z)\,|_{z=0}\, e^{-z\sqrt{k_x^2-k_0^2}}\, dk_x \qquad \text{for } k_0^2 < k_x^2
\end{aligned}
\tag{2.4}
$$

determines the field amplitude at a distance z. Employing the probe as an aperture of width w in an opaque plane, convoluting it with the field and integrating the far–field yields the results given in figure 2.4 [1] based on calculations [43]. It reproduces graphically the impact and the importance of equation (2.1).

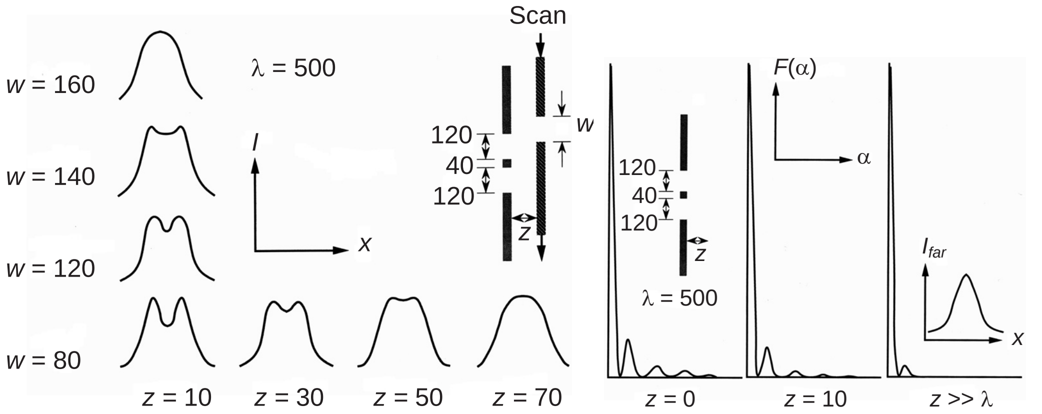

(a) The calculated optical signals represent various probe sizes w and distances z.

(b) The Fourier spectra of the double slit at various distances. Also shown is the far–field image I_{far}.

Figure 2.4: A coplanar aperture is scanned as a probe across a double slit. All units are given in nm. Taken from [1].

From the Fourier spectrum it becomes clear, that the high frequency components fade out at larger distances z between probe and sample. The calculation is straightforward, but nevertheless ignores certain aspects i.e. for example polarization effects. Image artifacts are briefly explained in appendix B.

It may be remarked that Heisenberg's uncertainty principle holds true, even for resolution beyond the diffraction limit, as Vigoureux and Courjon have presented in [44]. For consistency with the uncertainty principle, an arbitrarily small confinement of Δx of the imaged particle in real space implies an increase in the momentum uncertainty Δp_x.

2.2.2 Instrumentation

In general, the highly sensitive SPM techniques requires distances between probe and sample in the nm range, therefore the distance control has to be stable, reliable and protected against any mechanical impact. Vibrations and drifts have to be damped and eliminated. The fragile probe itself also is the most sensitive part representing the interface between sample and observer. The distinction in two different operation modes, constant height mode (CHM) and the constant gapwidth mode (CGM) makes sense in the way as CGM is the normal mode for data collection and CHM can be used to ensure the disappearance of pattern associated to the near–field. Artifacts that creep into the image can complicate the interpretation (see also appendix B). Figure 2.5 shows for example in (a) by lateral refractive index contrast and (b) topography modulations how topography can influence the optical contrast because CHM is fine for (a) but in (b) it will not allow to detect all the evanescent waves of the topography modulations.

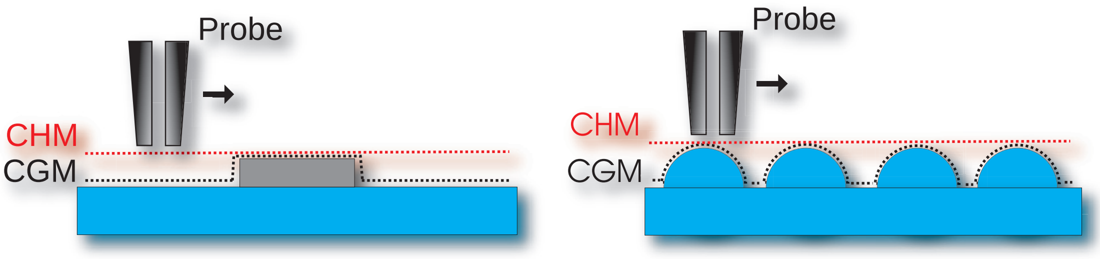

(a) Advantage of CHM (b) Complication in CHM

Figure 2.5: Two different modes in SNOM for scanning.

In the SNOM investigations during this thesis, heat pulled glass fiber [1, 45] tips have been used. Details on the fabrication process are given in section 4.2. The tip – sample distance is controlled by the servo–loop (see figure 2.2), based on the interaction that is commonly known as shear–force [31, 32]. The exact mechanism for this kind of interaction that happens in the range of 5–20 nm from the sample surface is still not yet fully understood.

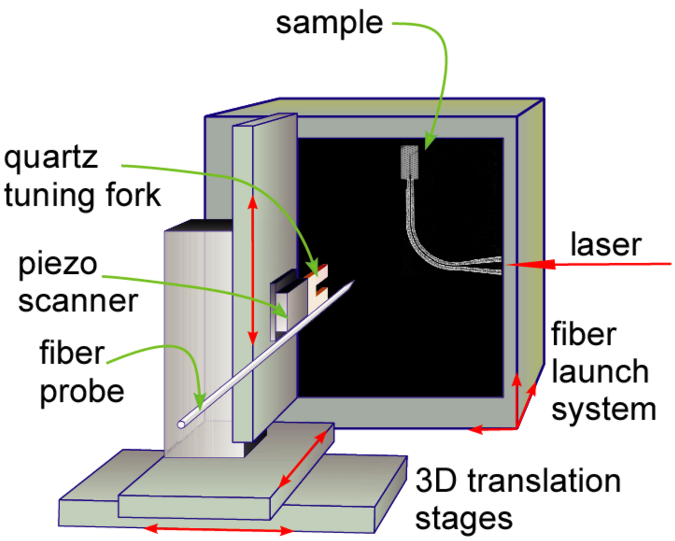

Figure 2.6: Schematic drawing of the essential parts of the SNOM device. The translation stage and the fiber launch system are for coarse and fine positioning, respectively, and for the subsequent adjustment with the piezo scanner to get the full linear range of the piezo for scanning. The figure is based on artwork from C. Hettich [46].

Figure 2.6 shows a schematic diagram of a SNOM. Various methods can be used to excite the omtion of the fiber tip and detect the shear–force damping, see for instance [1]. For this device, the tip is glued to a prong of a quartz tuning fork [47] with a certain protrusion of the fiber tip. It is excited by a sinusoidal voltage, with a frequency slightly below the resonance. The response from the fork and the reference signal are fed into a lock–in amplifier which puts out an error–signal, that is a difference of a nominal/actual signal value comparison which is kept constant: The off–resonance of the driving frequency of the fork means an offset for the error signal that determines the set point for regulation which is performed by the loop–amplifier that drives the input for the distance control voltage of the piezo scanner thus giving a feedback via damping to the fork response (see also 2.2.1). The point resulting from this, is for CGM to keep a constant distance separation between tip and sample surface that is determined by the aforementioned set point voltage. The topographical image that SNOM provides, is the corresponding piezo voltage that is required to track the surface. Examples for the different illumination modes in SNOM are illustrated in figure 2.3 (a)–(f). The topography image allows one to correlate surface features with surface light.

2.2.3 Resolution

Having a look through a microscope, very small things and features are revealed that hide away from the naked human eye. The eye itself is able to see for instance small shining particles that are even much smaller than the notorious stated $\lambda/2$ diffraction limit. So what makes the difference, one could ask. In the first case, at a certain magnification there is need for a suitable strong signal that can be detected, requiring sufficiently enough photons have to be collected by the objective lens. Its aperture angle α (see figure 2.7) determines "how much can be seen", if there is enough contrast between the features to recognize a difference. The next question that rises is how two objects that are very close to each other can be distinguished. That is exactly the point why a definition of spatial resolution is required. The definition can be a little arbitrary (see figure 2.8) and depends on the situation in the application [1].

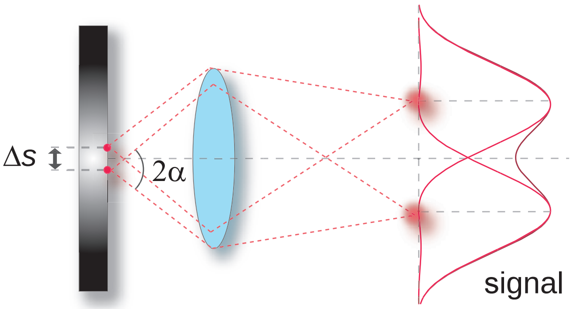

Figure 2.7: Resolution Δs in classical optical microscopy. For near–field optical microscopy $\Delta s \approx w$ holds true, if the distance to the sample $z \gg \lambda$, where w denotes the aperture.

In reference to figure 2.7, the numerical aperture NA of the collecting optics relates as follows to the light cone:

$$\mathrm{NA} = n \cdot \sin\alpha, \tag{2.5}$$

where n stands for the refractive index of the surrounding medium in which the light is emitted and collected. The image of a point (circular) object becomes in terms of Fraunhofer diffraction a finite spot (Airy disc) accompanied by concentric diffraction fringes [48].

The calculation to express the intensity, considers a radial symmetric field that relates to a Bessel function of second kind and yields in numerical approximation the radius of the Airy disc, which is modulo 2π the number in the Rayleigh resolution limit,

$$\Delta s \cong 0.61 \frac{\lambda_0}{n\,\sin\alpha}, \tag{2.6}$$

according to the resolution criterion in figure 2.8. Δs is the minimum distance between two points–like light sources that can be resolved, according to a specific wavelength λ_0. A closer look reveals that Lord Rayleigh's (1842–1919) resolution limit only holds true for incoherent luminescent light sources e.g. stars. The Sparrow criterion is another criterion for resolution, which requires the modulation transfer function (MTF, see appendix F) to become zero.

The diffraction limit after Abbé [5] originates from the resolution of diffraction grating lines of a certain spatial frequency under coherent illumination [49]. Despite peculiarities that may vary

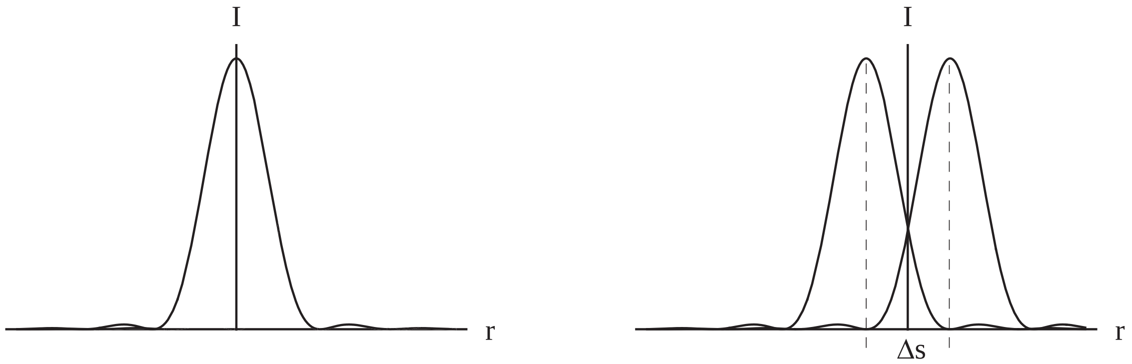

(a) Radial intensity (cross–section of the Airy disc)

(b) Rayleigh criterion for resolving two point–like sources

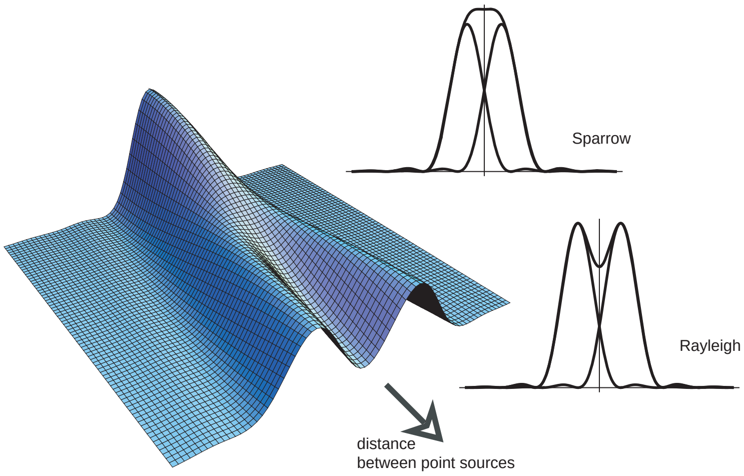

(c) Illustration of the criteria

Figure 2.8: (a) The radial intensity of the Airy disc (b) The Rayleigh criterion is defined by having the main maximum coinciding with the lowest order minimum of the two intensity pattern originating from point–like objects and (c) increase of the distance in between the two objects suggesting both of the criteria, Sparrow and Rayleigh respectively by this simple illustration (For the plots, incoherent light was assumed).

the numerical factor, the ultimate limit is:

$$\Delta s = \frac{\lambda_0}{2\mathrm{NA}} = \frac{\lambda_0}{2\, n \sin \alpha}, \tag{2.7}$$

where NA is the numerical aperture of the collecting optics. The concept of the numerical aperture is due to E. Abbé, who scientifically approached the issue of designing microscope optics under C. Zeiss who ran a microscope factory in Germany at his time [50].

Chapter 3

Photonic crystals

3.1 Introduction

The last decades have been strongly affected by the advances in semiconductor physics and materials. The development of the transistor in 1948 by J. Bardeen and W. H. Brattain [51] truly has led to a revolution with respect to the changes in our daily life. Semiconducting materials were found to be prime candidates for tailoring the electrical conducting properties through doping[1].

Closely related to the electronic properties are also the optical properties. For example in the field of application for high efficiency solar cells, optical semiconductor components or integrated optics for the telecommunication industry and related fields [52]. The shift in the frontier of information processing from electrons to photons had an impact on communication in terms of data transfer that was revolutionized by optical fibers that allow very large bandwidths. The engineering of materials to control the optical properties on a decreasing length scale increasingly became subject of research in the last few years.

3.2 The evolution of photonic crystals

There are a few examples of photonic crystals (PHCs) which occur naturally and can be recognized by its light iridescent effects. By name, two examples are gemstone opal and crystallites on the wings of some butterflies such as for the *Morpho granadensis* ("Blue Morpho") [53] or the *Thecla damo* [54, 55]. Amazing is the fact of the different purpose e.g. light polarization as mating signal [56] or thermal regulation [57]. Apart from the beauty and phenomena of nature and coming to the elegancy of science, V. Bykov [58] already in 1972 predicted the inhibition of spontaneous emission in periodic structures and later in 1987 independently and almost at the same time E. Yablonovitch [59] and S. John [60] published their theoretical evaluations from ideas on a structure, which is today described as PHC. E. Yablonovitch's paper deals with the proposal of the possibility to control spontaneous emission within the photonic band gap (PBG) in a PHC. Today this issue is still in the focus of actual research. Yablonovitch proposed the application of the solid state physics concepts to the field of PHCs for reasons of analogy.

The principle of a perfect PHC is the periodic modulation of the refractive index by ordered dielectric materials in the spatial dimensions. The adjective photonic emphasizes that the modulation length is in the order of the corresponding photon wavelength. The term crystal states the repetition of identical unit structures in the dimensions of space. In solid state physics structure consists of a number atoms or molecules — in terms of a PHC rather a super lattice of material blocks (which naturally again itself consist of atoms or molecules with a smaller lattice structure). The periodic arrangement forms the crystal structure[2]. More details will follow in section 3.3.3.

---

[1] The systematic introduction of impurity atoms into the "pure", that means with respect to the impurity ground level, semiconductor. In terms of the band structure, this leads to defect states for the charge carriers and therefore the conducting properties.

[2] A more detailed insight can be gained from standard works of solid state physics like the book of Ch. Kittel [61] or N. Ashcroft and D. Mermin [62].

Induced defects in the artificially fabricated photonic crystal allow localization of light in a spatially confined to sub–wavelength scale geometry. Just as the wave propagation of a conduction electron in solid state crystals, the propagation of light in photonic crystals is similar. The dispersion relation of a photonic crystal can be described with band structures, the reciprocal lattice and the Brillouin zone concept. Details can be found in [52]. At certain photon energy ranges light propagation may be prohibited simultaneously for all directions analogous to the band gap in a semiconductor PHCs may show a PBG, which has important consequences for quantum optics that are not complete at this stage and still have to be observed: The inhibition [63] or enhancement of radiative processes like spontaneous emission. Point–defects can act as sub–λ cavities that enhance the radiative properties of extremely small light sources. Therefore integrated optical devices and optical components can be realized in different wavelength ranges, suitable materials and lattice structures. The variety of applications (like wave guides, beam splitters, micro–resonators, interferometer, coupler, filter, optical switches etc.) is actually restricted by the realization of an efficient and accurate fabrication at the corresponding wavelength range. An excellent review on the subject of photonic crystal research is given by S. Noda and T. Baba in [64].

An insight into actual research about combinations of integrated optical circuits with applications like e.g. micro systems for fluids can be gained from the work of M. Lončar *et al.* [65].

3.3 Theoretical treatment

As denoted before, there is a strong analogy between the concepts of solid state physics and the artificial electromagnetic crystal structures. Basically, a PHC is the optic analogue to an electronic semiconducting crystal [66] so that a particle of light in a PHC can be treated in the same way like an electron in a semiconductor crystal. In a PHC the refractive index of the material is periodically modulated in space on a length scale comparable to the light wavelength for which the PHC shows its specific properties. That means in terms of a crystal, that the periodicity of its lattice is in the order of the wavelength of the scattered wave–like objects. In a semiconductor, it is the periodic arrangement of atoms that forms the periodic potential that modifies the energy–momentum relation of electrons due to Bragg–like diffraction from the different lattice planes (see appendix A) and therefore leads to the creation of a band structure for the energy and a frequency windows where electrons with certain energies cannot propagate in certain directions (also called stop gap).

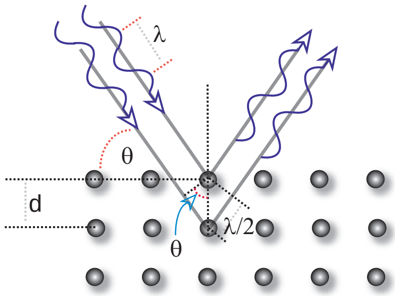

Figure 3.1: The properties of a PHC rely on interference. The Bragg condition [61] reads $2d\sin(\Theta) = m\lambda$ ($m \in \mathbb{Z}$) and determines mirror–like behavior of crystal planes of distance d for an oblique incident plane wave with angle Θ parallel to the plane. It only occurs for wavelengths $\lambda \leq 2d$. If for example the incident wave vector $k = 2\pi/\lambda$ becomes π/d at $\Theta = 90°$ it is reflected, i.e. encounters a forbidden frequency for which it cannot propagate.

A stop gap for all directions and all polarizations in a PHC will be referred to as a photonic band gap. For the example of a semiconductor there is a band gap between the valence and the conduction band that is complete what means that the gap is extended to all directions.

For light these stop gaps are quite familiar from dielectric mirrors[3] or "quarter–wave stacks" ("Bragg stacks") [52, 68], whose structure is a one–dimensional (1D) periodic modulation of the refractive index. Therefore a material with a complete PBG needs a three–dimensional (3D) periodic arrangement of dielectric material contrast.

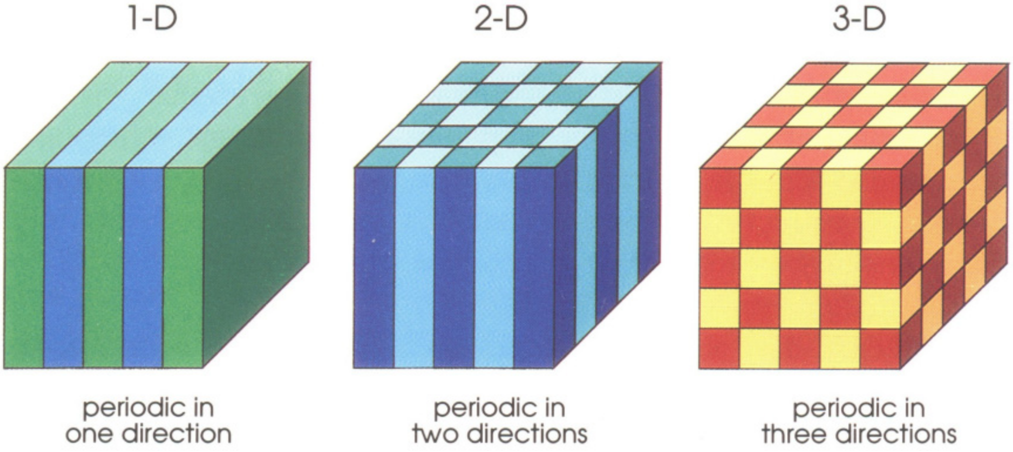

Figure 3.2: Simple sketch for periodic arrangement of dielectric material contrast in an increasing number of dimensions of space (taken from [52]).

For a semiconductor, Schrödinger's scalar time–independent equation has to be solved for a periodic potential caused by the lattice atoms [62]. This is situation in close analogy to the periodic change of the refractive index in a PHC, whereas here the linear Hermitian eigenvalue problem concerns the vectorial Maxwell's equations that have to be solved for electromagnetic waves in a periodic modulated environment. This mathematical formulation comprises some useful properties e.g. the orthogonality of modes, the electromagnetic variational theorem [52] and facilitates perturbational calculations [69]. Further, really crucial differences between electron waves in a semiconductor and electromagnetic waves in a PHC are the non–negative energy eigenvalues in the electrodynamic equation of movement in spite to the time independent Schrödinger equation, because only the squared values of the eigenfrequencies occur. For a semiconductor there is an importance for the transitions between the different energy bands and levels, whereas for a PHC the existence or absence of electromagnetic modes at certain frequencies is the focus of interest.

3.3.1 Basics of electromagnetism

The optical phenomena of PHCs can be described in the framework of electrodynamics like in [52]. In matter, the macroscopic Maxwell equations [70] read in the CGS–system (see appendix F)

$$\begin{aligned} \nabla \cdot \mathbf{B} = 0 \qquad \nabla \times \mathbf{E} + \frac{1}{c}\frac{\partial \mathbf{B}}{\partial t} = \mathbf{0} \\ \nabla \cdot \mathbf{D} = 4\pi\rho \qquad \nabla \times \mathbf{H} - \frac{1}{c}\frac{\partial \mathbf{D}}{\partial t} = \frac{4\pi}{c}\mathbf{J}, \end{aligned} \tag{3.1}$$

where **E** and **H** respectively denote the macroscopic electric and magnetic fields' strengths, **D** and **B** denote the dielectric displacement and magnetic induction fields' strengths, ρ and **J** are the densities of free charges and currents, and c is the speed of light in free space. A derivation of these formulae from the corresponding microscopic counterparts is given in the excellent book from Jackson [70].

---

[3] There is also a couple of different applications like dielectric optic filters, anti–reflection coatings (ARCs) or materials for distributed feedback (DFB) lasers. See, for example, Hecht [48] or Kneubühl [67].

The propagation of electromagnetic waves is assumed to be in a passive material consisting from macroscopic homogeneous domains of different dielectric materials (that are not necessarily periodically arranged), where $\rho = 0$ and $\mathbf{J} = \mathbf{0}$ are valid. Generally, the components of the dielectric displacement field can be expanded in a power series [71]:

$$D_i = \sum_j \epsilon_{ij}\, \mathbf{E}_j + \sum_{j,k} \phi_{ijk}\, \mathbf{E}_j \mathbf{E}_k + \mathcal{O}(\mathbf{E}^3). \tag{3.2}$$

The dependencies of the particular magnitudes are denoted by the position vector $\mathbf{r}$, the frequency ω of the electromagnetic wave and t for time. For the most dielectric materials the following assumptions can be employed:

(i) The field strengths are small enough for linear approximation, i.e. the coefficients of all terms higher than first order in $\mathbf{E}$ vanish. In general those coefficients are tensors.

(ii) The material is macroscopic and isotropic, therefore $\mathbf{E}(\mathbf{r}, t)$ and $\mathbf{D}(\mathbf{r}, t)$ are scalar linked to a dielectric constant $\epsilon(\mathbf{r}, \omega)$. For the anisotropic case, an analog formalism for μ can be applied.

(iii) ϵ does not explicitly depend on the frequency ω of the electromagnetic wave.

(iv) The medium is intended to be lossless, so $\epsilon(\mathbf{r})$ can be taken as a real number: $\epsilon \in \mathbb{R}^+$.

(v) $\mathbf{H}(\mathbf{r}, t)$ and $\mathbf{B}(\mathbf{r}, t)$ relate in $\mathbf{B}(\mathbf{r}, t) = \mu(\mathbf{r}) \cdot \mathbf{H}(\mathbf{r}, t)$ and the magnetic permeability $\mu(\mathbf{r})$ is close to unity[4]: $\mu \simeq 1$.

Taking all these simplifying assumptions into account, for a macroscopic medium, whose physical properties can be assumed to be linear and isotropic, the relations in a dielectric medium read

$$\begin{aligned} \mathbf{D}(\mathbf{r}, t) &= \epsilon(\mathbf{r}) \cdot \mathbf{E}(\mathbf{r}, t) \\ \mathbf{H}(\mathbf{r}, t) &= \mathbf{B}(\mathbf{r}, t). \end{aligned} \tag{3.3}$$

By that, the Maxwell equations (3.1) reduce to:

$$\begin{aligned} \nabla \cdot \mathbf{H}(\mathbf{r}, t) = 0 \qquad & \nabla \times \mathbf{E}(\mathbf{r}, t) + \frac{1}{c}\frac{\partial \mathbf{H}(\mathbf{r}, t)}{\partial t} = \mathbf{0} \\ \nabla \cdot (\epsilon(\mathbf{r})\mathbf{E}(\mathbf{r}, t)) = 0 \qquad & \nabla \times \mathbf{H}(\mathbf{r}, t) - \frac{\epsilon(\mathbf{r})}{c}\frac{\partial \mathbf{E}(\mathbf{r}, t)}{\partial t} = \mathbf{0}. \end{aligned} \tag{3.4}$$

Since the equations (3.4) are linear in $\mathbf{E}$ and $\mathbf{H}$, the temporal and spatial dependency can be separated. This works as follows: The fields are expanded into a set of harmonic modes. In fact, this is a restriction of the fields to vary harmonically (in terms of a sinusoidal pattern) in time, but any solution can be constructed by a Fourier transformation of an adequate combination from these modes that leads to a certain mode profile. Each mode can be written as

$$\begin{aligned} \mathbf{E}(\mathbf{r}, t) &= \mathbf{E}(\mathbf{r}) \cdot e^{i\omega t} \\ \mathbf{H}(\mathbf{r}, t) &= \mathbf{H}(\mathbf{r}) \cdot e^{i\omega t}. \end{aligned} \tag{3.5}$$

Only the real parts of the complex–valued fields correspond to the physical fields. This is quite convenient to simplify arithmetics. The combination of (3.5) in the divergence equations of (3.1) leads to the solenoidal conditions for the fields

$$\begin{aligned} \nabla \cdot \mathbf{H}(\mathbf{r}) &= 0 \\ \nabla \cdot \mathbf{D}(\mathbf{r}) &= 0. \end{aligned} \tag{3.6}$$

---

[4] For diamagnetic ($\mu < 1$) or paramagnetic ($\mu > 1$) matter, the deviations from 1 are in the order of $\pm 10^{-5}$. For ferromagnetic ($\mu \gg 1$) matter the approximation $\mu = 1$ does not hold any more [70].

The fields do not contain any point–like sources or drains within the medium and the electromagnetic waves have to be transverse[5]. Inserting (3.5) in both of the two curl equations from (3.4) yields

$$\begin{aligned}\nabla \times \mathbf{E}(\mathbf{r}) + \frac{i\omega}{c}\mathbf{H}(\mathbf{r}) &= 0 \\ \nabla \times \mathbf{H}(\mathbf{r}) - \frac{i\omega}{c}\epsilon(\mathbf{r})\mathbf{E}(\mathbf{r}) &= 0\end{aligned} \tag{3.7}$$

The equations (3.7) can be decoupled by taking the curl and combining them with each other. As a result, the corresponding wave equations for the magnetic and electric eigenmodes read:

$$\nabla \times \left(\epsilon^{-1}(\mathbf{r})\nabla \times \mathbf{H}(\mathbf{r})\right) = \left(\frac{\omega}{c}\right)^2 \mathbf{H}(\mathbf{r}) \tag{3.8}$$

$$\nabla \times (\nabla \times \mathbf{E}(\mathbf{r})) = \left(\frac{\omega}{c}\right)^2 \epsilon(\mathbf{r})\mathbf{E}(\mathbf{r}) \tag{3.9}$$

It is the idea, to determine $\mathbf{H}(\mathbf{r})$ from equation (3.8), which is also called master equation, at a certain frequency and for a given $\epsilon(\mathbf{r})$. From the rearrangement of the equations (3.7), the electric field $\mathbf{E}(\mathbf{r})$ can be evaluated from the first equation of (3.10):

$$\begin{aligned}\mathbf{E}(\mathbf{r}) &= -\frac{ic}{\omega}\frac{1}{\epsilon(\mathbf{r})}(\nabla \times \mathbf{H}(\mathbf{r})) \\ \mathbf{H}(\mathbf{r}) &= \frac{ic}{\omega}(\nabla \times \mathbf{E}(\mathbf{r})).\end{aligned} \tag{3.10}$$

The valid modes have to satisfy the condition (3.6). In analogy, this can be done for (3.9) in the same manner for the electric field $\mathbf{E}(\mathbf{r})$ with respect to the second equation of (3.10) and condition (3.6). Further analysis shows that this way would be complicated at the point, when the issue is formulated in terms of an eigenvalue problem. This is thoroughly elucidated in [52]. The key point turns out to be that for $\mathbf{E}(\mathbf{r})$ the eigenvalue problem becomes more general and more complicated to solve without offering an efficient way to cope with the arising generalization. Equation (3.8) can be written as

$$\Theta\mathbf{H}(\mathbf{r}) = \left(\frac{\omega}{c}\right)^2 \mathbf{H}(\mathbf{r}) \tag{3.11}$$

$$\Theta\mathbf{H}(\mathbf{r}) \equiv \nabla \times \left(\epsilon^{-1}(\mathbf{r})\nabla \times \mathbf{H}(\mathbf{r})\right) \tag{3.12}$$

to turn its appearance more into an eigenvalue problem. The differential operator defined in (3.12) is linear, i.e. any linear combination of solutions is in turn a solution. The eigenvectors $\mathbf{E}(\mathbf{r})$ are the field pattern according to the harmonic modes and the eigenvalues $(\omega/c)^2$ are proportional to the corresponding squared frequencies of those modes. Furthermore the operator is Hermitian under the standard inner product. For real $\epsilon > 0$ it is positive–definite what implies real eigenfrequencies ω. Further reading on the general properties (harmonic modes, variational principle and scaling properties) is given in [52]. Nevertheless a short look on the scaling properties can be found in subsection 3.3.2.

Inserting (3.3) into equation (3.9) yields

$$\nabla \times \left(\nabla \times \frac{\mathbf{D}(\mathbf{r})}{\epsilon(\mathbf{r})}\right) = \left(\frac{\omega}{c}\right)^2 \mathbf{D}(\mathbf{r}). \tag{3.13}$$

---

[5] This can be easily seen e.g. for a plane wave $\mathbf{H}(\mathbf{r}) = \mathbf{A} \cdot e^{i\mathbf{k}\cdot\mathbf{r}}$. The condition (3.6) requires $\mathbf{A} \cdot \mathbf{k} = 0$.

And in analogy to (3.12)

$$\begin{aligned} \Xi\mathbf{D}(\mathbf{r}) &= \left(\frac{\omega}{c}\right)^2 \mathbf{D}(\mathbf{r}) && (3.14)\\ \Xi\mathbf{D}(\mathbf{r}) &\equiv \nabla \times \left(\nabla \times \frac{\mathbf{D}(\mathbf{r})}{\epsilon(\mathbf{r})}\right) && (3.15) \end{aligned}$$

an operator Ξ can be defined. Ξ is not Hermitian, because of the misplaced $\epsilon(\mathbf{r})$ compared to the operator (3.12). Multiplying (3.15) by $1/\epsilon(\mathbf{r})$ allows to define a generalized eigenvalue equation, which is a more complicated numerical task. Defining a new field $\mathbf{F}(\mathbf{r})$

$$\mathbf{F}(\mathbf{r}) = \frac{1}{\sqrt{\epsilon(\mathbf{r})}}\mathbf{D}(\mathbf{r}) \tag{3.16}$$

would bring the generalized eigenvalue equation back in the form of a simple eigenvalue equation

$$\frac{1}{\sqrt{\epsilon(\mathbf{r})}}\nabla \times \left(\nabla \times \frac{1}{\sqrt{\epsilon(\mathbf{r})}}\right)\mathbf{F}(\mathbf{r}) = \left(\frac{\omega}{c}\right)^2 \mathbf{F}(\mathbf{r}), \tag{3.17}$$

including a Hermitian differential operator, but anyway the field $\mathbf{F}(\mathbf{r})$ is not transverse. Obviously, there is no adequate efficient way to fix this problem without imposing more difficulties.

3.3.2 Scaling properties

Anticipating the result of the calculus, there is no fundamental length scale for electromagnetism in dielectric media and therefore in PHCs. One assumption was that the medium has to be macroscopic for the sake of the corresponding Maxwell equations (3.1). In conclusion, there is also no fundamental value of the dielectric constant $\epsilon(\mathbf{r})$. Hypothesizing a medium whose dielectric constant $\epsilon(\mathbf{r})$ is scaled by a parameter s: $\epsilon'(\mathbf{r}) = \epsilon(\mathbf{r}/s)$. Changing the variables in (3.8) by definition of $\mathbf{r}' \equiv s\mathbf{r}$ and therefrom following $\nabla' = \nabla/s$, gives:

$$s\nabla' \times \left(\frac{s}{\epsilon(\mathbf{r}'/s)}\nabla' \times \mathbf{H}(\mathbf{r}'/s)\right) = \left(\frac{\omega}{c}\right)^2 \mathbf{H}(\mathbf{r}'/s) \tag{3.18}$$

Obviously, $\epsilon(\mathbf{r}'/s) = \epsilon'(\mathbf{r}')$ and therefore equation (3.18) can be written as (s taken to the right)

$$\nabla' \times \left(\frac{1}{\epsilon'(\mathbf{r}')}\nabla' \times \mathbf{H}(\mathbf{r}'/s)\right) = \left(\frac{\omega}{cs}\right)^2 \mathbf{H}(\mathbf{r}'/s), \tag{3.19}$$

i.e. the again the master equation, where $\mathbf{H}'(\mathbf{r}') = \mathbf{H}(\mathbf{r}'/s)$ is the new mode profile and $\omega' = \omega/s$ the new frequency. Also the solutions are scaled by the same factor. Finally, considering the change in a system that holds $\epsilon(\mathbf{r})$ to one, only differing by a global constant factor, e.g. $\epsilon'(\mathbf{r}) = \epsilon(\mathbf{r})/s^2$. The replacement of $\epsilon(\mathbf{r})$ in the master equation (3.8) makes

$$\nabla \times \left(\frac{1}{\epsilon'(\mathbf{r})}\nabla \times \mathbf{H}(\mathbf{r})\right) = \left(\frac{\omega s}{c}\right)^2 \mathbf{H}(\mathbf{r}). \tag{3.20}$$

In the new system, the harmonic modes remain unaffected, but the frequencies are scaled by the factor s. So, if the dielectric constant is multiplied by an overall factor 1/4, the mode patterns do not change although the frequencies double. The pretty example was taken from [52].

3.3.3 Basic principles of a crystal

Referring to the beginning of section 3.3, the general concept to describe a crystal will be explained more. A n–dimensional perfect crystal is an infinite repetition of identical structure units in n dimensions of space. Throughout the document, formulas will be given for the 3D case ($n = 3$), because they simplify for lower dimensions. It is obvious that $1 \leq n \leq 3$.

In the case of a PHC, the structure unit concerns the change of the refractive index on a length scale comparable to the photon's wavelength range for which the PHC shows its specific properties. The crystal structure is described by an infinite matrix of points. If this is abstractly or not depends on the point of view — nevertheless, the concept is useful. The so–called lattice[6] consists of regular, periodically arranged points and a basis, here the structure unit. By the definition of n fundamental translation vectors $\{\mathbf{a}_i\}$ with $i = 1, \ldots, n$ the lattice and the vectors are called *primitive* if the lattice is identical in any point $\mathbf{r}$ to

$$\mathbf{r}' = \mathbf{r} + \sum_i u_i \mathbf{a}_i \tag{3.21}$$

for arbitrary integer values u_i ($u_i \in \mathbb{Z}$). The crystal basis and the set of the translation vectors $\{\mathbf{a}_i\}$ are chosen by the crystal's symmetry. For example, a simple point–to–point translation of the lattice is defined by the vector $\mathbf{R}$:

$$\mathbf{R} = \sum_i u_i \mathbf{a}_i \tag{3.22}$$

and a combination of natural numbers u_i. By the way, (3.22) can be taken as a mathematical definition of the Bravais lattice because $\mathbf{R}$ generates all lattice points.

The set of the primitive vectors $\{\mathbf{a}_i\}$ span the crystallographic axes and the primitive unit cell, i.e. the cell with the smallest volume $\mid \mathbf{a}_1 \cdot \mathbf{a}_2 \times \mathbf{a}_3 \mid$ (with respect to the number of dimension), which exactly fills the Bravais lattice when translated by all vectors $\mathbf{R}$ of (3.22).

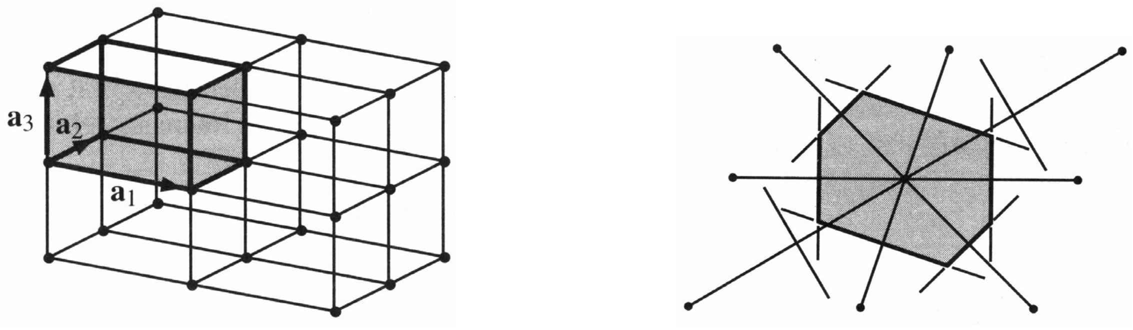

(a) Primitive unit cell

(b) Wigner–Seitz cell

Figure 3.3: (a) Example for a 3D primitive unit cell in a cubic lattice (b) The grey patch is a simple sketch for a Wigner–Seitz cell in 2D (Image source [61])

The choice of a primitive unit cell is not unique and one could think of many other possibilities. A quite convenient and simple concept for a primitive unit cell is the *Wigner–Seitz* unit cell. It exhibits the full symmetry of the lattice and bears a center (an atom, a structure unit etc. for instance). Depending on the task, this description can be very useful. The *Wigner–Seitz* unit cell for a given point of the lattice is the smallest polyhedron that arises from the connection of the given point to all next neighboring lattice points and the bisection of the connecting lines by

---

[6] The Bravais lattice. The different Bravais lattices are classified by the dimension of the lattice and the symmetries of the point groups. Their number is trivial in 1D, 5 for 2D and 14 for the 3D case. The different names and structures (P, C, I, F, R and special like sc, bcc, fcc, hcp) can be found elsewhere [61, 72].

orthogonal planes. To distinguish different lattice planes of the direct lattice, the Miller indices (hkl) are used. For details, see appendix A.

3.3.4 The reciprocal lattice

The concept of a reciprocal lattice is practical for wave propagation in periodic structures. A more mathematical treatment of the background can be found in [62]. In summary, the Fourier transform of a function $f(\mathbf{r}) = f(\mathbf{r}+\mathbf{T})$, that is periodic on a lattice, is taken, where $\mathbf{T}$ is the translation vector (3.22). $f(\mathbf{r})$ is assembled from plane waves with different wave vectors, that turn out to be the reciprocal lattice vectors $\mathbf{G}$ from (3.24). The periodicity requires $\mathbf{G} \cdot \mathbf{T} = 2\pi N$ with $N \in \mathbb{Z}$. For a given set of direct lattice vectors $\{\mathbf{a}_i\}$ and exploitation of the cross product's properties, the set of primitive reciprocal lattice vectors $\{\mathbf{b}_i\}$ (3.23) can be constructed, being pinned down to the condensed condition $\mathbf{a}_i \cdot \mathbf{b}_j = 2\pi\delta_{ij}$, where δ_{ij} is the Kronecker symbol . In short, additional to the lattice in direct space for the real crystal, another one is introduced in reciprocal space, spanned by the primitive reciprocal lattice vectors $\{\mathbf{b}_i\}$. These are defined by

$$\mathbf{b}_1 = 2\pi\frac{\mathbf{a}_2 \times \mathbf{a}_3}{\mathbf{a}_1 \cdot \mathbf{a}_2 \times \mathbf{a}_3}, \quad \mathbf{b}_2 = 2\pi\frac{\mathbf{a}_3 \times \mathbf{a}_1}{\mathbf{a}_1 \cdot \mathbf{a}_2 \times \mathbf{a}_3}, \quad \mathbf{b}_3 = 2\pi\frac{\mathbf{a}_1 \times \mathbf{a}_2}{\mathbf{a}_1 \cdot \mathbf{a}_2 \times \mathbf{a}_3}. \tag{3.23}$$

The reciprocal lattice of a Bravais lattice (defined in section 3.3.3) is itself a Bravais lattice. This can be noticed from the general reciprocal lattice vector:

$$\mathbf{G} = \sum_i v_i \mathbf{b}_i \tag{3.24}$$

for $v_i \in \mathbb{Z}$. For the reciprocal lattice the Wigner–Seitz primitive cell can be constructed as well as for the direct lattice. The primitive cell constructed in this manner is referred to as the first *Brillouin zone*. By a similar construction around the first zone, the second zone can be obtained and so on the higher zones. In 2D, the first Brillouin zone for a square lattice is a square, for a triangular lattice a hexagon rotated with respect to the real space, both of them centered around the origin. In 3D, the first zones become less simple, of course and look like truncated polyhedrons. An insight into the topic from the group theory can be found in [73]. Special points of high symmetry (center, edge, corner, etc.) are labelled by: Γ, M, X, K, . . . For symmetry reasons, the first Brillouin zone can be reduced to the *irreducible* zone, because the rest of the first Brillouin zone contains only redundant copies of it. Examples are shown in figure 3.4.

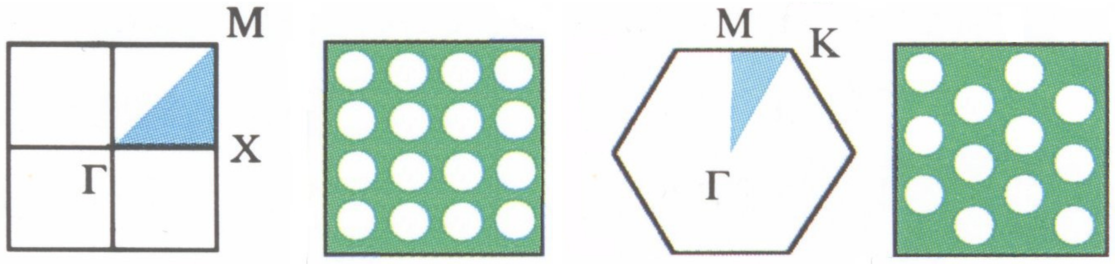

(a) Square lattice

(b) Triangular lattice

Figure 3.4: First Brillouin zones and high symmetry points in larger scale for its corresponding lattice. The different dielectric materials are green and white colored. The light blue shaded area shows the corresponding irreducible Brillouin zone (modified from [52]).

The structure units that build up the PHC will be taken into account for the examination of the "potential" that arises from a periodic array of different dielectrics in wavelength scale, i.e. the dielectric function $\epsilon(\mathbf{r})$ that is periodic on a lattice.

3.3.5 Photonic band structures

Due to the strong analogy between photonic and solid state crystals the methods for electronic band structure calculation can be used to calculate photonic band structures. On the one hand, due to the vectorial character of the Maxwell equations, they are more complicated to solve compared to the scalar Schrödinger's time–independent equation. On the other hand the periodic potential in the solid state problem caused by the periodicity of the atom cores has to be determined self consistently because of fermionic electron–electron interaction whereas the photonic "potential" is fixed to the spatial periodicity of the dielectric function $\epsilon(\mathbf{r})$.

Felix Bloch, a pioneer in the analysis of wave propagation in 3D periodic media [74], based his theorem on an 1D theorem by G. Floquet [75]. The theorem has approved in solid state physics [61] and can be applied to the spatial modulated dielectric constant $\epsilon(\mathbf{r})$ of PHCs, due to the strong analogy: Inside the medium, the wave propagation is a periodic envelope function multiplied by a plane wave [62]. $\epsilon(\mathbf{r})$ can be developed in a Fourier series over the reciprocal lattice vector:

$$\epsilon^{-1}(\mathbf{r}) = \sum_{\mathbf{G}} \kappa_{\mathbf{G}} \cdot e^{i\mathbf{G}\mathbf{r}} \tag{3.25}$$

The spatial periodicity of $\epsilon(\mathbf{r})$ permits the application of Bloch's theorem to the eigenmodes of the eigenvalue problem (3.11) that is the master equation (3.8) rewritten by the operator Θ (3.12)). The eigenmodes or eigenvectors $\mathbf{H}_{\mathbf{k}}(\mathbf{r})$ can be decomposed as a phase multiplied by a periodic function on the lattice

$$\mathbf{u}_{\mathbf{k}}(\mathbf{r}) = \mathbf{u}_{\mathbf{k}}(\mathbf{r}+\mathbf{R}) \tag{3.26}$$

for all direct lattice vectors $\mathbf{R}$:

$$\mathbf{H}_{\mathbf{k}}(\mathbf{r}) = e^{i\mathbf{k}\mathbf{r}}\mathbf{u}_{\mathbf{k}}(\mathbf{r}). \tag{3.27}$$

The modes or Bloch states are labelled by the Bloch wave vector $\mathbf{k}$:

$$\mathbf{k} = \sum_i k_i \mathbf{b}_i. \tag{3.28}$$

where $\mathbf{b}_i$ are the reciprocal lattice vectors defined in (3.23) and $\mathbf{k}$ is inside the Brillouin zone[7]. The periodic boundary condition (3.26) restricts the eigenvalue problem to a unit cell of finite volume yielding to an infinite set of modes with discrete spaced frequencies $\omega_n(\mathbf{k})$, labelled by $n \in \mathbb{N}$. Because of the lattice periodicity that causes redundancy in the label $\mathbf{k}$, it is useful to restrict the analysis to the first Brillouin zone. At the edge of the first Brillouin zone the dispersion relation $\omega_n(\mathbf{k})$ is folded back, thus forming n bands. The structure of the bands contained in $\omega_n(\mathbf{k})$ can be calculated from a given $\epsilon(\mathbf{r})$ of a photonic crystal. To solve explicitly the equation (3.11) with respect to the label n, the eigenvectors (3.27) can be written as

$$\begin{aligned} \mathbf{H}_{n,\mathbf{k}}(\mathbf{r}) &= e^{i\mathbf{k}\mathbf{r}}\mathbf{u}_{n,\mathbf{k}}(\mathbf{r}) \\ &= \sum_{\mathbf{G}} \mathbf{u}_{\mathbf{G}}^{n,\mathbf{k}} e^{i(\mathbf{k}+\mathbf{G})\mathbf{r}}. \end{aligned} \tag{3.29}$$

The insertion of (3.25) and (3.29) in the eigenvalue problem (3.11) leads to an infinite set of linear eigenvalue equations that can be reduced by taking condition (3.6) for $\mathbf{H}$ into account. The numerical approximation deals with matrices of finite size $3m \times 3m$ by a limitation of the number of reciprocal lattice vectors m and also benefits from (3.6) by reducing the matrices dimensions to $2m \times 2m$ because it constricts the development to two orthogonal polarization vectors that are additionally orthogonal to $\mathbf{k}+\mathbf{G}$ and have to be determined in each lattice point $\mathbf{G}$ anew. In conclusion, starting point is the numerical task to approximate the squared eigenvalues $\omega_n^2(\mathbf{k})/c^2$. More details on the procedure can be found in [63, 76]. Further reading is provided by [77–80].

---

[7] All values of $\mathbf{k}$ outside the zone can be obtained from adding $\mathbf{G}$ because the $\mathbf{G}\cdot\mathbf{R} = 2\pi N$ gives no phase difference and the physical mode will remain the same.

In this manner all eigenmodes of a PHC inside the first Brillouin zone can be illustrated in a band diagram. Examples for these band diagrams for PHCs whose periodicity is extended to one or more dimensions will follow in section 3.3.6. Gap maps are plots that show the locations of PBGs as a function of various crystal parameters like lattice structures, dimensionality, r/a ratio, polarization modes, dielectric contrast, etc. [81]. A common distinction for the modes that solve the wave equations (3.8) and (3.9) for some boundary condition, is to speak in terms of two polarization modes, where one has only transverse and no longitudinal field in one of the components **E** or **H**. The former is called transverse electric (TE) mode and the latter transverse magnetic (TM) mode [82]. In general, the TE modes in a 2D PHC have **H** normal to the lattice plane and **E** in the plane. For TM, the situation is vice versa [52].

The Bloch modes have a physical significance in the experiment: Propagating light in photonic waveguides shows modulations that can be related to the Bloch harmonics [83, 84].

3.3.6 Dimensionality

A way to classify photonic crystals is the number of dimensions in which the refractive index periodically changes in terms of a structure without restriction to a certain symmetry.

One–dimensional photonic crystals

In section 3.3 examples were given for applications of 1D structures. It may have a layer structure in the 1D case as depicted in figure 3.2. The different layers must neither have the same thickness nor the depicted arrangement (e.g. Bragg fiber [85]). In the investigations a 1D PHC is used as a resonator structures (see figure 3.7).

Two–dimensional photonic crystals

A sketch for the structure is depicted for the 2D case in figure 3.2. One of the most prominent examples are photonic crystal fibers (PCF) first proposed by T. Birks *et al.* [86]. A state–of–the–art survey is given by T. Hasegawa in [87], applications can be found in [88].

Photonic crystal slabs are build from a layered structure that consists of a high refractive index film sandwiched inside a low refractive index medium therefore confining the light normal to the slab plane by total internal reflection (TIR) [89]. In the slab plane light is confined due to the periodic structure of the drilled air holes (see figure 3.5). In the band structure (see for example the 3D case in figure 3.6 (b)), the upper and the lower band are sometimes referred to as "air band" and "dielectric band" distinguished by the localization of the modal power emphasizing the strong analogy to the "conduction band" and "valence band" above and below the fundamental gap [52].

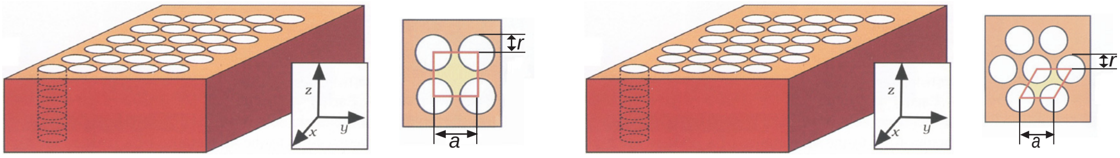

(a) 2D square lattice

(b) 2D triangular lattice

Figure 3.5: Two different lattices in 2D PHC slabs of air columns in a dielectric medium. r denotes the radius of the columns and a the lattice constant i.e. the periodicity (based on figures from [52]).

The 2D slab structure offers the advantage of an easy process compared to 3D PHC fabrication techniques at this stage and possesses a pseudo–PBG, because most angles for TIR are covered. And it is regarded to be the most suitable design for photonic integrated circuits [89].

Three–dimensional photonic crystals

Due to the scale properties given in section 3.3.2 the first 3D photonic crystal build by man was Yablonovite named after Eli Yablonovitch [90] for the micrometer wavelength range based on theoretical studies for a complete PBG [91]. A summary on the present state of development and the different structures in 2D and 3D gives [92].

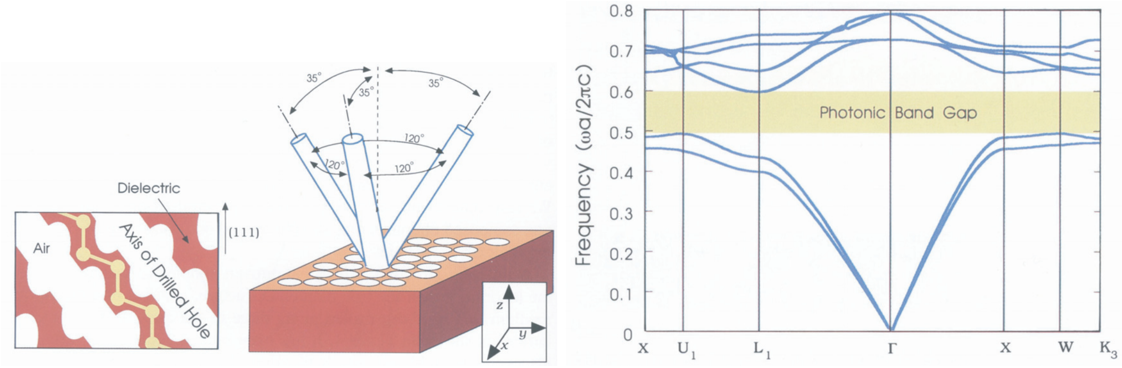

(a) Yablonovite (b) Photonic band structure

Figure 3.6: (a) Construction method: A triangular array of holes is drilled into a bulk material block (b) The photonic band structure of Yablonovite [90] (taken from [52]).

3.4 Defect structures

It is useful to fabricate PHCs with "defects" in the lattices structure. By breaking the translational symmetry the defects are intended to localize modes within the PBG. A point defect (green in figure 3.7) is the most simple by means of variation in the hole size or missing it out. Calculations on the mode structures are given in [52, 93, 94]. Surrounded by reflecting walls the defect forms a resonator which is characterized by the dimensionless quality factor, universally defined by

$$Q = 2\pi \frac{\omega E}{-\frac{\mathrm{d}E}{\mathrm{d}t}}, \tag{3.30}$$

where E is the stored energy in the resonator, ω the resonance frequency and $P = -\mathrm{d}E/\mathrm{d}t$ the dissipated energy of the mode [95, 96] per unit time. More descriptively that means that the resonator can sustain a number of Q oscillations until the energy drops below $e^{-2\pi} = 0.19\%$ its original value [97]. In that sense the quality factor also quantifies the enhancement of the field. Resonators with a Lorentzian profile Q can be written as

$$Q = 2\pi \frac{\omega}{\Delta\omega}, \tag{3.31}$$

where $\Delta\omega$ defines the full width at half maximum FWHM of the resonant peak. A single line defect (SLD) is formed by leaving out a row of point defects, that allows light localization in x–direction and light propagation in y–direction respectively (in reference to figure 3.7). The idea of using defects is to modify the PBG for photonic crystal devices that confine the light at sub–wavelength regimes and therefore have the same length scale. SNOM potentiates the visualization of the optical properties on such a small length scale.

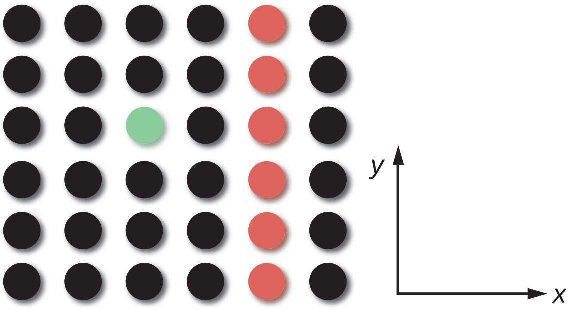

Figure 3.7: Illustration of defect: green – point, red – line

In case of a waveguide where one or more (N) rows of the lattice are missing the waveguide structure abbreviated as W1 (WN). The line defect width affects the waveguiding characteristics and group–velocity dispersion [98]. Theoretical studies on networks with various components (bends, splitters, couplers, crosses, …) can be found in [99, 100]. A survey on various defect structures that have been realized gives [101, 102] and further development in future gives [103]. An example of the the band structure for a crystal modified by a line defect is depicted in figure 3.8.

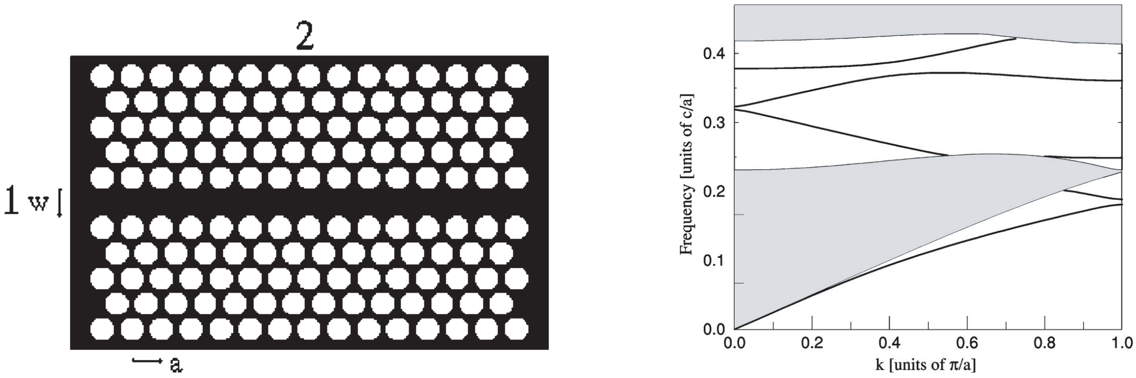

(a) Top view onto the waveguide

(b) Band structure

Figure 3.8: (a) Waveguide in Γ–M direction in a 2D PHC slab. a denotes the lattice constant and w in this image the waveguide width. (b) shows the band structure of the perfect crystal and the introduced defect states (taken from [104]).

The light blue shaded area originates from the perfect crystal and the lines illustrate the allowed waveguide modes. In this case the defect line introduce three bands into the 2D stop gap.

3.5 Finite–difference time–domain simulations

The finite–difference time–domain (FDTD) method has gained popularity for electromagnetic problem modelling like solving Maxwell's equations (3.1) in real space and time. FDTD is used for photonic crystal simulations along other methods. Its algorithm is about 30 years old [105, 106]. The basics in short: Real space is separated in a discrete cubic lattice grid. For the arrangement of the field vectors see figure 3.9.

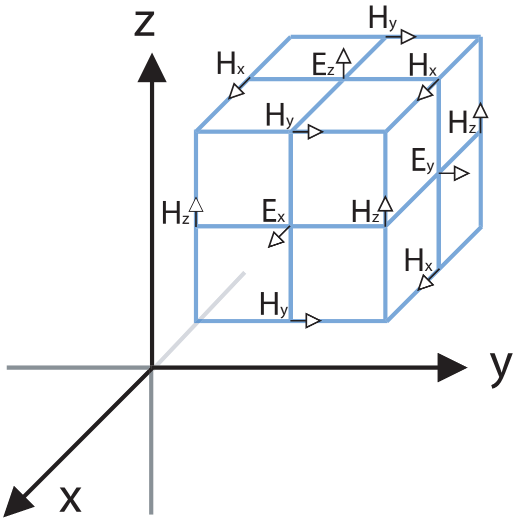

Figure 3.9: Arrangement of the grid points after [105, 106].

This geometry suggests itself to the line integral versions of Maxwell's equations (Faraday's and Ampere's law) makes the treatment suitable. The field distributions are stepwise calculated from a start distribution with respect to boundary conditions [107]. A main application are transmission coefficient calculations. Information on mesh size can be found in [108, 109]. A criterion for numerical stability is given in [106] whose physical meaning is a condition for causality [110]. In the simulations an emitting dipole in adjacency to the front of the waveguide slab was used for light in–coupling.

Chapter 4

Scanning near–field optical microscopy studies of photonic crystals

4.1 Introduction

An investigation of the optical properties of a PHC could be performed by camera of an adequate sensitivity in the specific wavelength range and a microscope–like imaging system with a certain magnification. But this imaging system would be constricted to Abbé's far–field diffraction limit. The use of an ultrahigh resolution device is required to see more of the topological and optical features of a PHC device.

4.2 Probe fabrication

Generally speaking, there is a huge variety of different probes and fabrication techniques. Different materials (glass, semiconductors, metals, . . .), methods of preparation (etching, heat pulling, etc.), coatings, apertures etc. are in common use to make reproducible probes.

The probes for the experiments were all home–made. The fiber tips were made from a standard telecommunication fiber (corresponds to SMF–28), provided by the *Deutsche Telekom*. Reproducible preparation was performed by a *Sutter P–2000 micropipette puller* instrument. Approximately 2 cm of the jacket was removed by a fiber stripper, the fiber clamped and locally heated by a CO_2 laser while pulling the fiber. The procedure was done automatically by the *Sutter* instrument, once the parameters had been programmed and optimized in continuous feedback from the experiment i.e. investigating the tips' properties as a function of different parameter settings. Empirically there was found a drift in the machine's parameters that got noticeable in about half a year.

In the very beginning of the experiment, to get an intuition for the SNOM device, much smaller AFM tips (ca. 10 nm in diameter) were scanned to get information on the SNOM probes (see figure 4.2). In short by scanning a smaller tip with a bigger probe yields the geometry of the latter.

(a) Fiber tip # 17

(b) Fiber tip # 28

Figure 4.1: Fiber tips under the optical microscope. The magnification is 2.5 times.

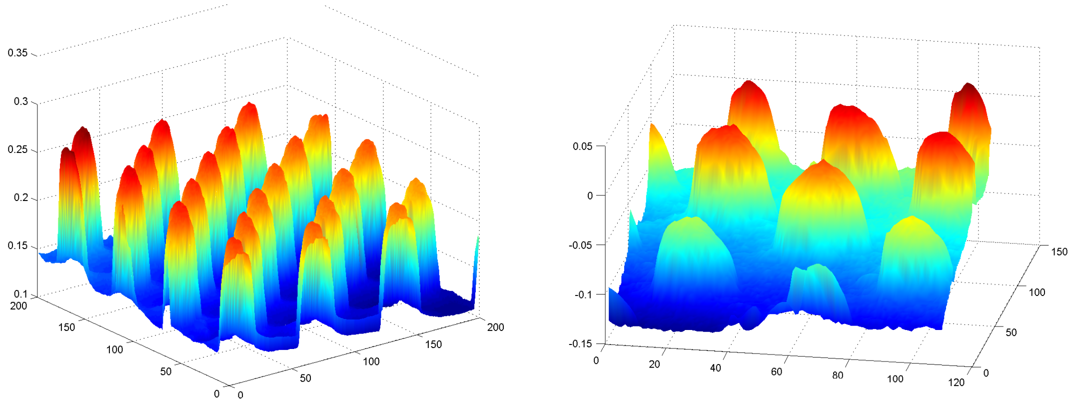

(a) Tip # 04: 260 0.15 s, scan range: 10 x 10 $\mu\mathrm{m}^2$ (b) Tip # 28: 300 0.14 s, scan range: 5.5 x 5.5 $\mu\mathrm{m}^2$

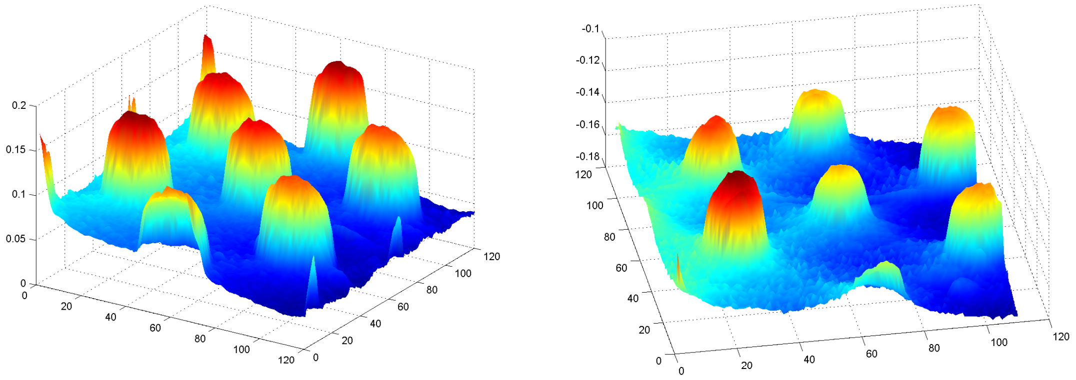

(c) Tip # 17: 310 0.11 s, scan range: 6 x 6 $\mu\mathrm{m}^2$ (d) Tip # 19: 320 0.10 s, scan range: 5.5 x 5.5 $\mu\mathrm{m}^2$

Figure 4.2: Height plot representations at different aspect rations of SNOM tip scans on a sample with AFM tips. The two parameters given after the tip's number are *heat* and *pulling time*. The corresponding optical microscope images are given for two tips in figure 4.1. The endings seemed to be quite blunt, of slightly asymmetric shape like in 4.2 (a).

A systematic procedure has been performed to optimize the heat parameter for the micropipette puller instrument. The programmable parameters of the machine are in brief:

- Heat (Heat) — concerns the laser output power
- Filament (Fil) — controls the scanning of the laser to increase the heated length (This parameter was left at “0” to minimize the heated length.)
- Velocity (Vel) — is defined by the temperature dependent viscosity of the glass and specifies the velocity of the slide that holds the material before the hard pull
- Delay (Del) — relative time delay between laser turn off and hard pull
- Pull — (Pul) defines the force of the hard pull

The pulling time is given (pt) in seconds. Further details on the parameters can be found in the manual [111], on optimization of the parameters there are reports in [45, 112, 113]. It should be noted, that most of the values are determined by the base material.

An introduction on the fabrication technique can be found in [45], including a summary on the theory of small apertures after Bethe [114] and Bouwkamp [115, 116] and the theory of coated glass tips by aid of the multiple multipole method [117]. First choice for details of the fabrication

Heat	Remarks
340	tips are extremely long and straight and become longer with increasing pt; short pt (< 0.09 s) yields sharp and nicely symmetric tips
330	tips are very long, straight and uniformly tapered but the very end is highly fragile
320	long tips, increasing pt yields a long uniformly taper
310	long tips, increasing pt gives a short uniform taper; pt around 0.11 s: robust tips
300	tips get shorter, uniformly tapered
290	short, straight tips; the end is very long and steady–going
280	same as 290, but seems to be independent from pt
270	longer tips; at pt = 0.10 s extremely long and straight, the ends are short and of uniform shape
260	short tapered tips

Table 4.1: Fixed parameters were: Pull only applied from one side, Vel = 18, Del = 126 and Pul = 150.

techniques is [113] and special further reading is provided by [118,119]. For a very good performance the tip has to be controlled after each step of the fabrication.

After successful tip fabrication the fiber probe was glued onto a prong of a tiny quartz tuning fork (see figure 4.4). These forks are commercially available from a distributor (*Farnell*) of electronic parts and are commonly used to clock watches as shown in figure 4.3. Usually the delivery is in a small vacuum sealed can hosting the two harmonic oscillators with a Q up to 10^5 and a nominal resonant frequency of 32.768 kHz ($= 2^{15}$). In air, the Q slightly drops and further down to a few 10^2–10^3 after gluing. Due to the increased stiffness from the attached glue and fiber also the resonance frequency is shifted up to 33–35 kHz. It was very interesting to observe that superglue needs a few days to harden out i.e. the resonance frequency increased during the next days after gluing when all got more stiff.

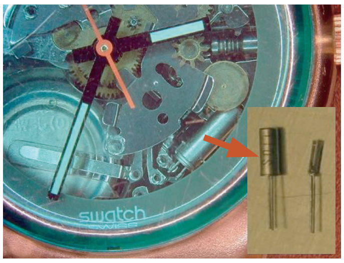

Figure 4.3: Watch crystal (based on a figure from [120]). The insert shows a photo of both of the tuning forks within the can and removed from the can.

Several glues have been tested for sticking the tip to the quartz prong: The best turned out to be a cyanoacrylate superglue for the prong and a two–component epoxy glue (*Uhu® plus schnellfest*) for the strain relief, that was just a droplet of glue on the plastic mount (see figure 4.4).

Figure 4.5 (a) displays schematically what can be also seen from the photo in figure 4.4: A tuning fork with an attached fiber tip. The capitals L, W and T denote length, width and thickness respectively (from a measurement: L = 3 mm, W = 370 µm and T = 230 µm). The protrusion length of the fiber is not arbitrary [46, 121] and should be chosen in the order below 100 µm, if possible.

The tips were examined on a test bench, that was build up in our laboratory for that purpose. The details of the devices used in the test setup can be seen in chapter C from table C.1. The test setup was used to check the quality factor of the tuning fork after the glue hardened out and the properties of the aperture of the tip in transmission by the diffraction pattern [124]. Similar technique for screening describes T. Cloninger *et al.* [125] and is also treated in detail in different

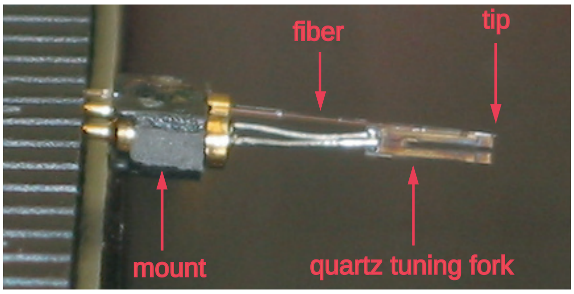

Figure 4.4: Uncoated tips were glued to a prong of a quartz tuning fork that is soldered on a two pin mount.

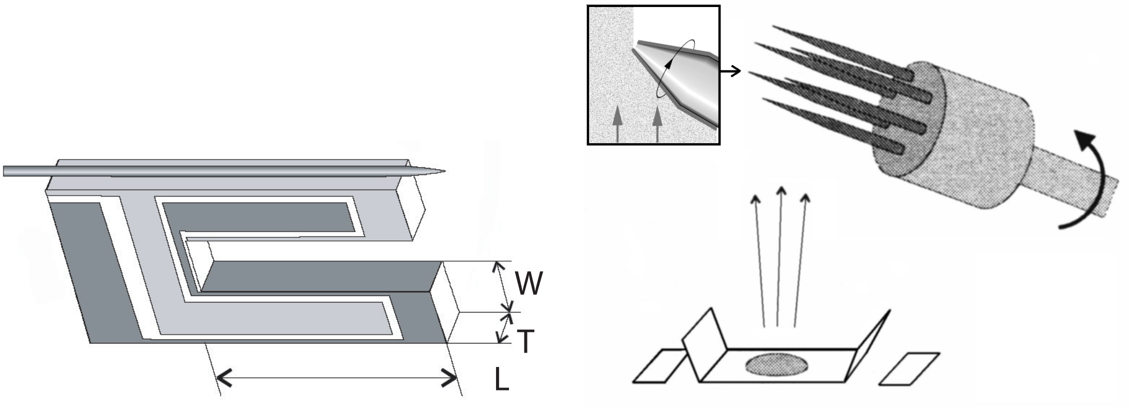

(a) Tuning fork dimensions (b) Tip coating process

Figure 4.5: (a) Tuning fork and its dimensions schematically. Based on figures from [47, 122]. (b) Schematic draw of the coating process (image sources: [45, 123]).

theses [122, 126].

Both coated and uncoated tips have been used in the experiment. The coatings were self–made in our laboratory in a *BAL–TEC BAE250* coating system depicted in figure 4.5 (b). Aluminium coatings as well as gold on chromium (as an adhesion layer) have been used.

SEM pictures of various coated and uncoated home–made SNOM probes are shown figure 4.6. The minimum aperture corresponds to the skin depth of the coating metal. A typical value for the tip curvature is around 50 and 100 nm. The taper optics in SNOM is described in detail elsewhere [127]. For throughput maximization a concentrator geometry is preferred [128–130], according to [1] a compound parabolic concentrator (CPC) that looks like a truncated parabola. Further reading for NFO probes and theory concerning metal coatings is summarized in [131].

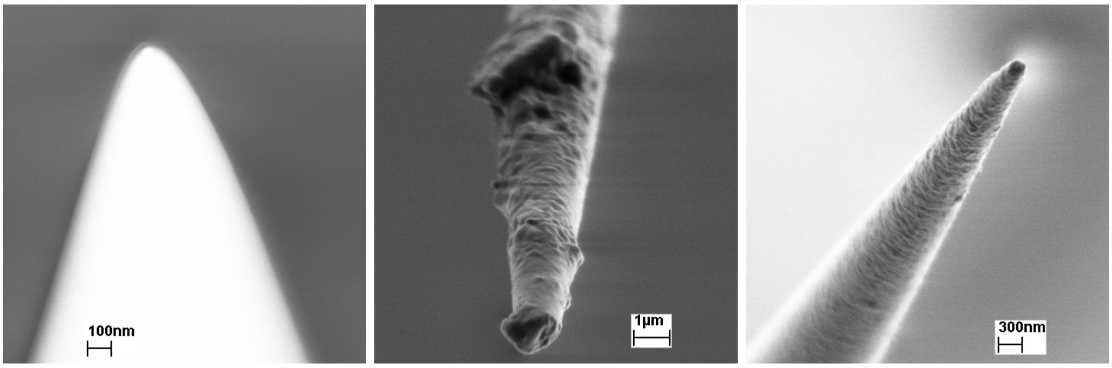

(a) Uncoated tip (b) Totally coated tip (c) Well coated tip

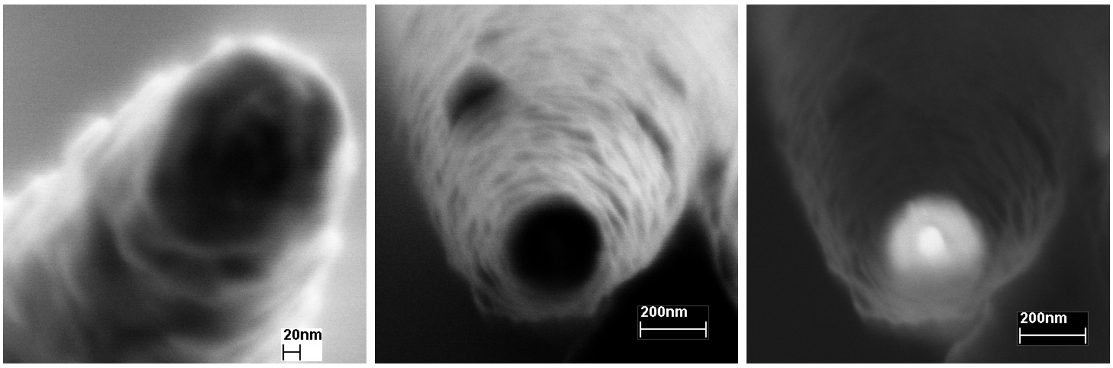

(d) Very end of tip in (c) (e) Apertured tip (1) (f) Apertured tip (2)

Figure 4.6: SEM investigation of the tips before (a) and after metal coating (b)–(f). (e) and (f) show the same image with different detectors. Typical values were ≈ 100 nm for the curvature (a) and ≈ 50 nm for the aperture (f).

4.3 Former studies of photonic crystals

Choo *et al.* in 1994 [132] reported a study of optical channel waveguides and directional couplers by SNOM. Besides the near–field measurements, also an investigation of the guided mode intensity distribution was included. It indicated the utility of ultrahigh resolution for photonic devices. A survey of SNOM applied to photonic devices can be found in [133]: SNOM has been used to characterize and map whispering–gallery modes (WGM) in microspheres [134, 135], the light confining properties of waveguides [136–138], laser diodes [139], vertical cavity surface emitting lasers (VCSELs) [140], microdiscs [141], microrings [142], fibers [143] and last but not least: photonic crystal devices [40, 83, 84, 144–156]. Actually, in SNOM there is even more potential for information by interferometric field amplitude and phase measurements [137, 157–159] and time resolved light propagation [138] as these researchers show. Further highlighted issues are the local second harmonic generation (SHG) in microcavities [160, 161] and optical antennae [162]. After this general introduction the experimental results of the thesis will follow in the next sections.

4.4 Indium phosphide technology based samples

4.4.1 Photonic crystal samples from the ETH

In collaboration with different institutes two different kinds of samples were investigated. First, there are the samples from the *Communication Photonics Group* of the *Swiss Federal Institute of Technology* in Zürich [163]. The different phases of the sample fabrication process are described in detail in [164, 165] and a short summary is depicted in figure 4.7. The crystals are based on InP technology, i.e. established semiconductor technology for dense integration and combination with electronics. More reasons for the use of InP are the transparency at $\lambda = 1500$ nm [166] i.e. the telecommunication wavelength and the low refractive index contrast in an InP/InGaAsP–system. The substrate is an InP wafer, followed by an InGaAsP layer, which is grown by metal organic chemical vapor deposition (MOCVD) of 400 nm thickness. Also shown in figure 4.7 is an InP top cladding of 200 nm thickness, which reduces plane loss, but was not present in the investigated samples to allow direct access of the SNOM probe to the evanescent field.

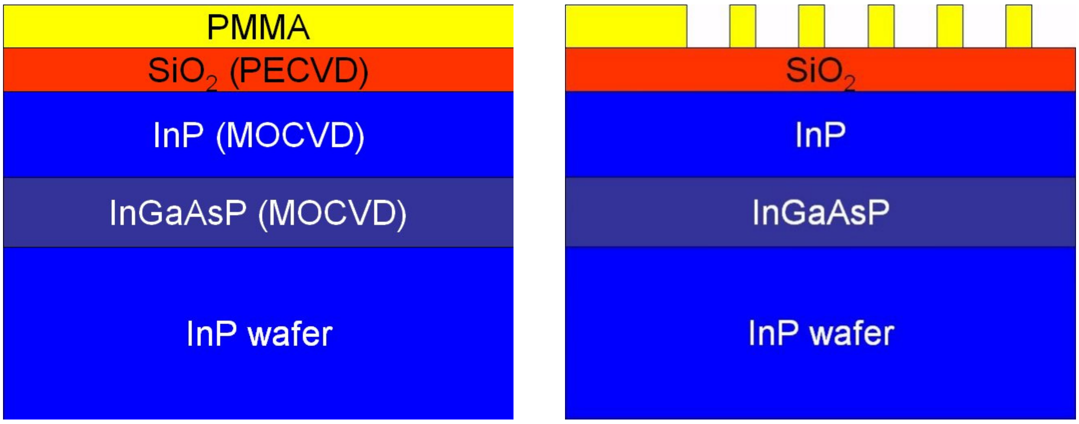

(a) Slab structure growth: MOCVD, PECVD

(b) E–beam lithography: Patterning of the PMMA mask

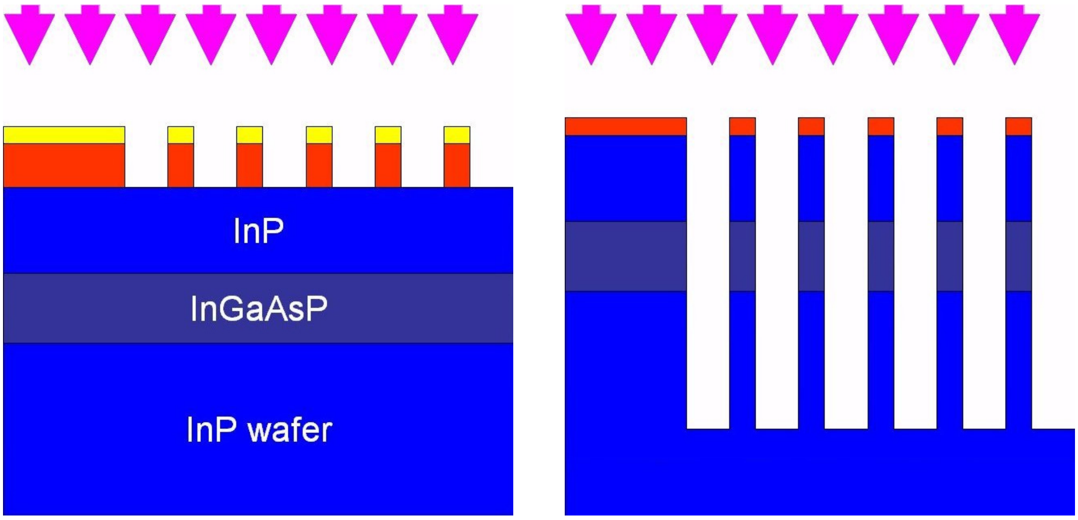

(c) Pattern transfer into silica mask via RIE etching

(d) Deep anisotropic RIE/ICP etching of the holes

Figure 4.7: The fabrication process described in the text depicted schematically in 4 steps. The original images appeared in [165]. EM pictures of the etching results for both samples are given in figure 4.12 (b) and (c).

On top there is a silica hardmask (SiO_2 or SiN_x) for etching, deposited by plasma–enhanced chemical vapor deposition (PECVD). The top finish forms a cover of PMMA electron beam resist that has a thickness of 220 nm. This resist is patterned by proximity–effect corrected (PEC) electron–beam lithography [164,167]. The pattern transfer into the silica mask is done via reactive ion etching (RIE) with CHF_3/Ar or CHF_3/O_2, followed by an inductively coupled plasma (ICP) anisotropic etching with $Cl_2/CH_4/H_2$ of the InGaAsP/InP layers.

The refractive indices are 3.15 for InP and 3.45 for InGaAsP in the NIR (near–infrared) wavelength range and bulk material [168]. For a better overview, the refractive indices are compiled in table 4.3 (see page 45).

4.4.2 Investigation of the ETH PHC samples

The geometry of the samples from the ETH had the slab structure described above. One side of the sample had a cleaved facet which had a ridge waveguide for the laser coupling either straight towards the PHC structure (see on the right in figure 4.10) bent by 90° respectively. An explanation for the choice of this geometry will follow.

The coupling area on the cleaved edge was 400 nm x 10 µm, therefore the laser always overfilled the edge because the focus size of a Gaussian laser beam is limited by diffraction to $\approx$ 1 µm. Figure 4.9 shows schematically the setup and the beam path for the ETH PHC samples. The details of the optical components are listed in the tables D.3 and D.4, respectively the devices in table C.2. A schematic sketch for the servo loop depicts figure 2.2. The sample itself was mounted on a single mode fiber launch system.

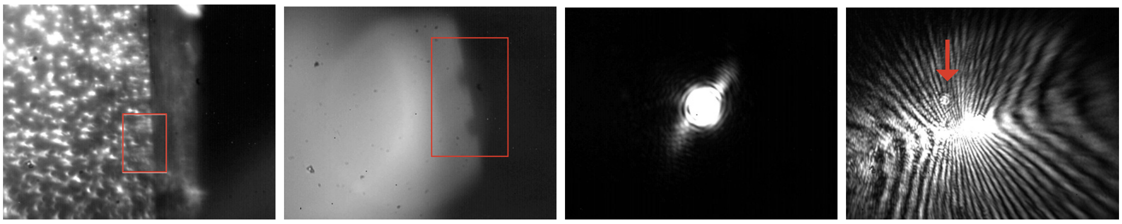

(a) Top view of the ridge waveguides (b) Ridge waveguide at the cleaved side (c) Focus at $\lambda = 1510$ nm (d) Top view of the ridge waveguide and the PHC

Figure 4.8: Far–field images of various parts of the sample during the optical alignment and laser in–coupling. The pictures were taken with the NIR CCD camera. The magnification is 10x for (a), (d) and 36x for (b), (c).

The back reflected light from the input facet was collected by the focussing lens L1.2 and sent through the polarizing beamsplitter cube, some mirrors and L3.2 to the NIR camera to image the focus on the sample. Once aligned, this became an useful tool for the laser focussing and coupling into the ridge waveguide and also for skipping to the next structure on the sample.

In figure 4.8 (a) a top view of the ridge waveguides in the white box is shown. The huge amount of stray light comes from the the sample on the left originating from the white light illumination. In (b) there is a side view on the cleaved edge showing the ridge “entrance”. (c) shows the focus and (d) a top view of the sample after successful in–coupling. The hyperbolic shaped stray originates from the sample edge. Note the small concentric circles slightly above the bright, concentrated spot due to scattered light from the PHC.

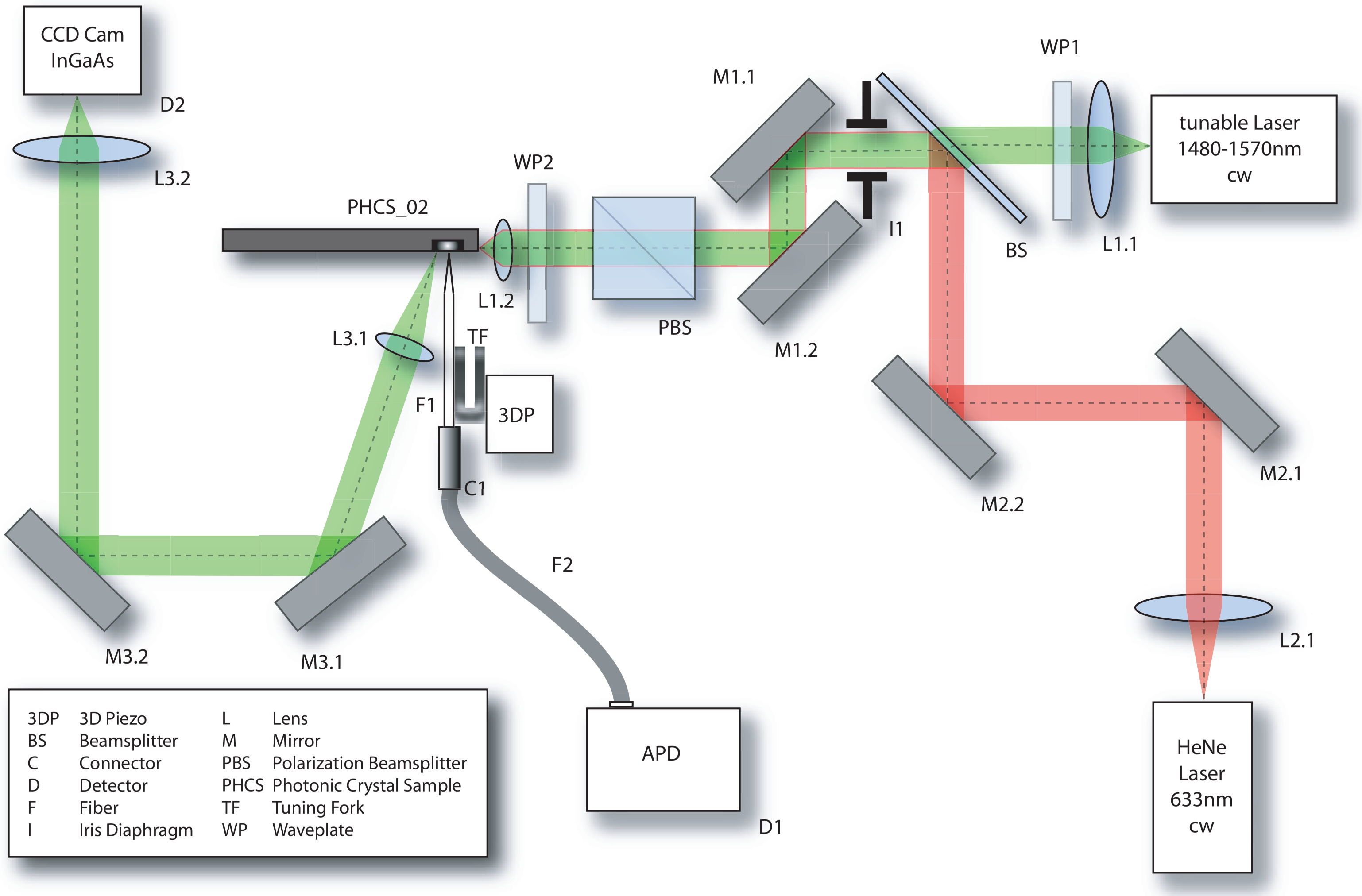

Figure 4.9: Beampath of the experimental setup in configuration for edgeways coupling

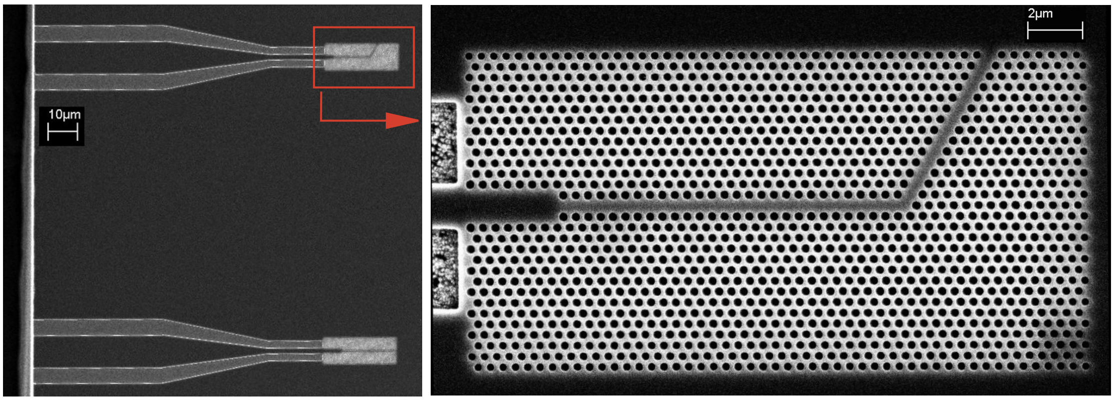

(a) Top view of the sample (b) Bent 2D waveguide

Figure 4.10: Electron microscope images of the ridge waveguide and the photonic crystal. The images were taken and provided by R. Wüest.

Figure 4.10 (a) shows a SEM image of an early sample from the ETH collaborators. Int this example the PEC was not fully optimized yet whereby an inhomogeneous depth profile of the holes resulted. The sample was not expected to possess a PBG for the wavelength range accessible by our laser and the core also did not have a cladding. This can be seen for $r/a = 0.3$ and the dimensionless frequency $\omega a/2\pi c \approx 0.32$ ($\widehat{=}\ \lambda = 1550$ nm) from a 2D–PHC gap map [169] (finite system, only TE shown) or [52, 170] (infinite system, TE and TM shown).

$a = 500$ nm was chosen for the lattice constant and 300nm for the hole diameter (i.e. radius $r = 150$ nm). The figures 4.11 show a SNOM measurement with an uncoated tip and a diode laser at $\lambda = 1550$ nm that was coupled into the sample by a lens. Technical details can be found in table D.3 and D.4. Figure 4.11 (a) shows the topography, (c) the recorded optical signal and (b) one upon the other.

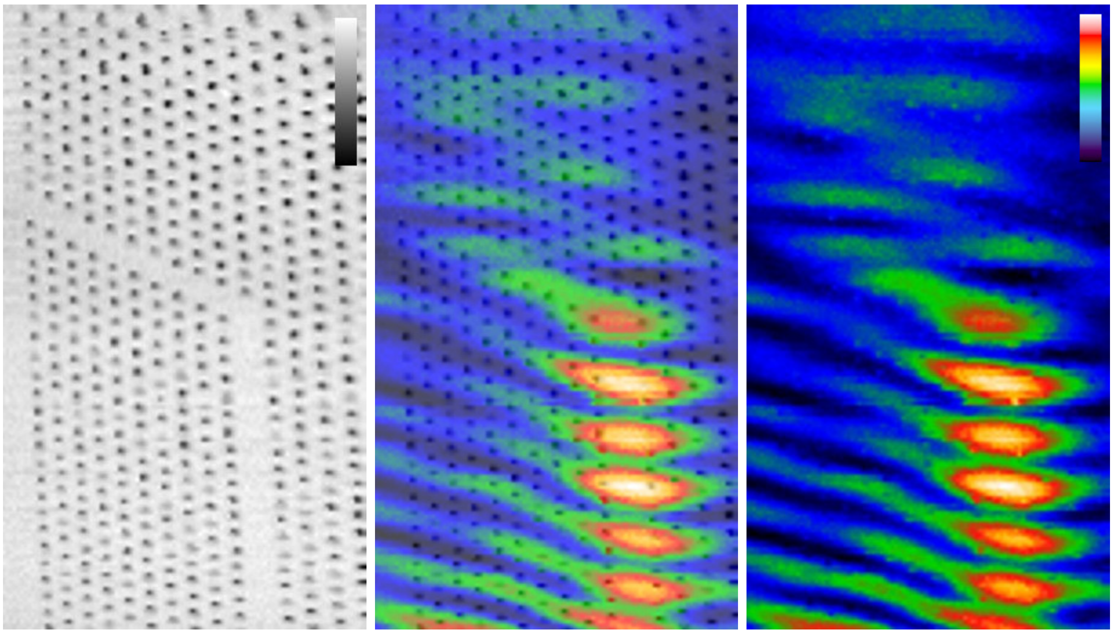

(a) Topography (b) Combination of the two (c) Optical image

Figure 4.11: SNOM optical and topographical image of a bent W1 waveguide.

The standing wave pattern can be explained from a reflection of a large part of the light at the bend of the structure. This pattern fits 2.8 times the lattice constant of the topography image. The light that is guided, is expected to be index guided [171], periodic modulated by the structure. Note, that the light is leaking into the area of the PHC. The same sample also included the straight waveguide (see figure 4.10 (b)) that also revealed in the measurements light guiding properties although the recorded images are spoilt by artifacts induced by the topography. This issue will be discussed later in appendix B.

Due to limited amount of space the SNOM device and the NIR CCD camera could not be used at the same time and by that a problem occurred by the stray light from in–coupling region: Either scattered light from the crystal area like in 4.8 (d) was not observed or in–coupling was not provided since a distinct signal in the SNOM was lacking. To improve the signal–to–noise ratio (SNR) the stray light was screened by a sharp blade. Having the opportunity to interfere in the fabrication process, the in–coupling design was modified. The 90° bend ridge waveguide should prevent light scattered from the in–coupling region reaching the crystal. An electron microscope image of the new design is shown in figure 4.12 (a). In addition, the crystal parameters were slightly changed: A lattice constant a of 450 nm and a hole diameter of 320 nm was chosen. The results after etching can be read from figure 4.12 (c).

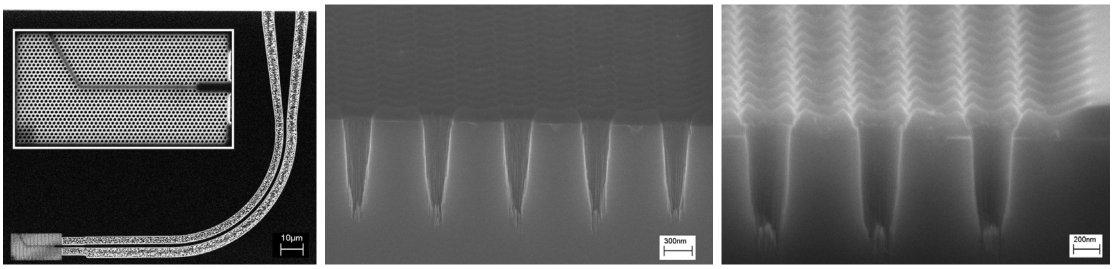

(a) Top view of the bent ridge waveguide (Second sample)

(b) Side view of the hole profiles for the first ETH sample

(c) Side view of the depth profile after PEC for the second ETH sample

Figure 4.12: (a) Electron microscope top view of the ridge waveguide bent by 90° of the second sample. The insert of the bent waveguide is not the same scale. (b) The etched holes from the preliminary etch process. (c) Improved results with PEC. Images kindly provided by R. Wüest.

The next step was the use of coated tips thereby reducing effectively the volume of light collection. Figure 4.13 shows the bend waveguide structure using a diode laser at $\lambda = 1550$ nm for both of the polarizations, TE and TM. The scans were recorded by use of a coated tip. Although there is no PBG for the TM mode, the sample shows light guiding properties [171].

The slight slant of the light pattern in the figure for TM polarization is due to measurement perturbations. This becomes obvious by looking at the control and the shear–force signal that reveal shifts corresponding to the optical signal. In the case of large scans like these, with size of 14×23.5 µm^2 each, it took about half an hour of recording to get the whole image. The sample itself is expected to have a bandgap for TE mode, therefore the light should be confined, what can be seen from figure 4.13. Figure 4.13 (d) shows the cross section in x–direction from the corresponding figure in 4.13 (c). It shows light confinement that has a FWHM of 1.65 µm. Figure 4.13 (e) shows the cross section in y–direction and the light undulations inside the W1 (see section 3.4). The undulations have a period of 5.6, 3.2, 2.5 and 1.4 times the lattice constant (see figure 4.13 (f)). This results from a FFT analysis calibrated to the lattice. An example for a program

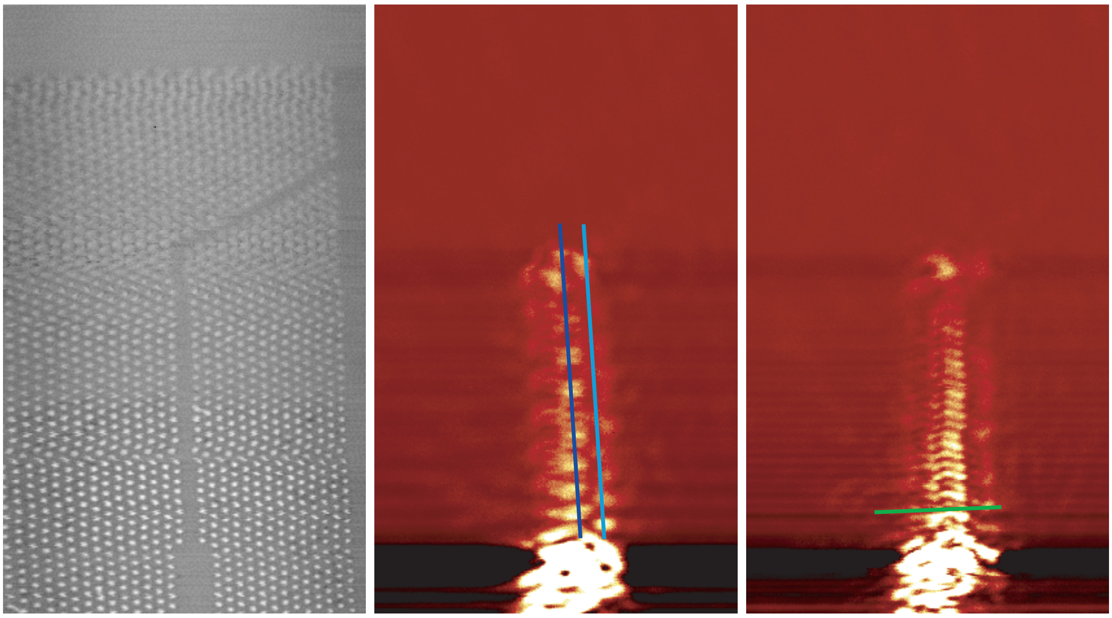

(a) Top view of the topography (b) TE polarization and cross section in y direction (c) TM polarization and cross section in x direction

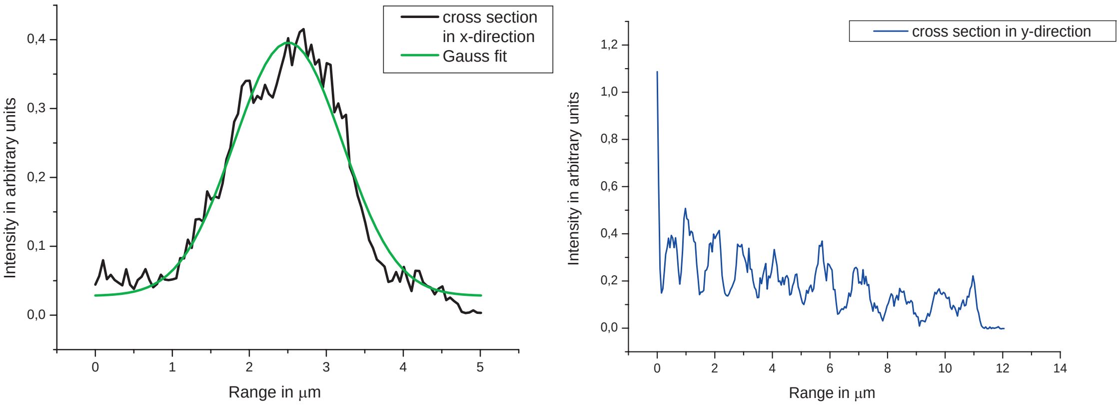

(d) Cross section in x direction (e) Cross section in y direction (W1)

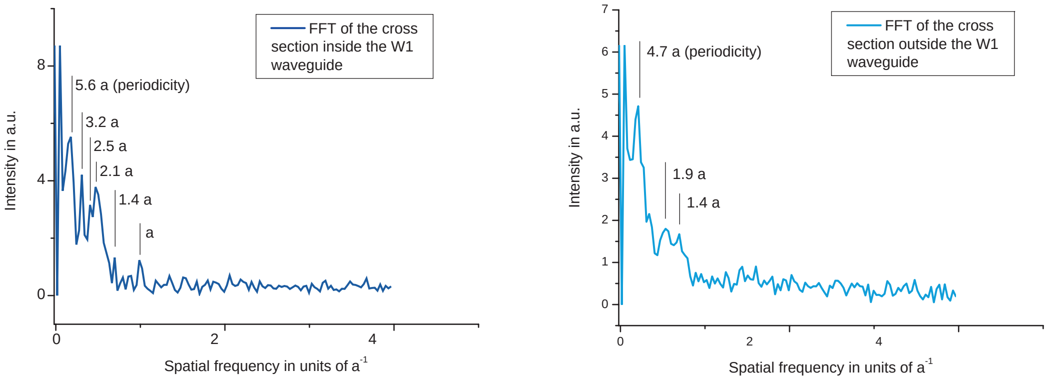

(f) FFT inside the W1 (g) FFT parallel to the W1

Figure 4.13: (a) Topography of the bend waveguide associated to the same area of the bend waveguide. (b) and (c) show the optical images (contrast enhanced) in both of the polarization modes. The dark blue line in (b) and the green in (c) denote where the x and y cross sections were taken. The light blue line sketches one of the parallel cross section outside. (d) shows the cross section in x– and (e) in y–direction. (f) and (g) are FFTs of the optical signal inside and parallel to the W1 waveguide.

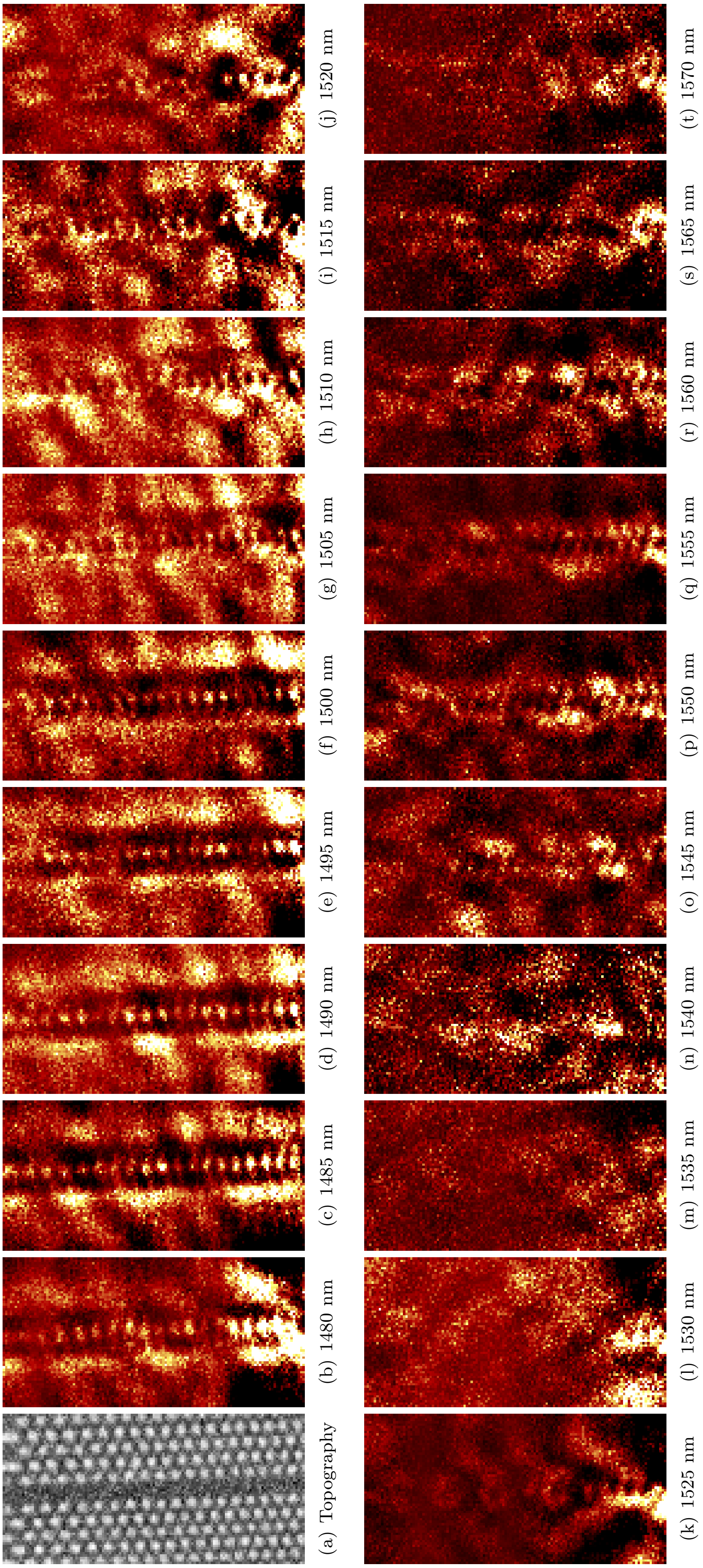

(a) Topography (b) 1480 nm (c) 1485 nm (d) 1490 nm (e) 1495 nm (f) 1500 nm (g) 1505 nm (h) 1510 nm (i) 1515 nm (j) 1520 nm

(k) 1525 nm (l) 1530 nm (m) 1535 nm (n) 1540 nm (o) 1545 nm (p) 1550 nm (q) 1555 nm (r) 1560 nm (s) 1565 nm (t) 1570 nm

Figure 4.14: Series of scans from the same area of a W1 waveguide by varying the wavelength from 1480 nm to 1570 nm in 5 nm steps. The scanned area is 5 x 10 μm^2 and the polarization mode TE. The tip was coated with gold. It shows clearly, that there is strong light confinement for several wavelengths and short undulations within the W1 region accompanied by longer undulations parallel to the waveguide in the region of the PHC. The images are contrast enhanced by different intensity cutoffs.

list for Matlab® can be found in appendix E. Also evident are the light undulations parallel next to the waveguide — more clearly in the contrast enhanced figure 4.13. A FFT of the cross sections taken along the W1 waveguide show periodicites of 4.7, 1.9 and 1.4 times the lattice constant (see figure 4.13 (g)). The cross section of the undulations outside the waveguide, represented by the light blue line in figure 4.13 (b), were taken approximately 1.1 µm parallel to the dark blue line (cross section of the W1) on both sides. The images were recorded with a gold coated tip.

The issue of light undulations became more interesting when using a tunable laser source that was available at the time when the second sample had been fabricated. The figures in 4.14 show SNOM images of a W1 waveguide for different wavelengths using a gold coated fiber tip. The corresponding topography 4.14 (a) is representatively for the optical images 4.14 (b)–(t).

To analyze the light undulations in figure 4.14, cross sections of the optical signal along the W1 waveguide were taken and Fourier transformed. Figure 4.15 (a) shows the Fourier transformations of the optical signal for each wavelength in a 2D diagram to illustrate the trends of the undulation periods. For $\lambda \geq 1525$ nm the high spatial frequencies fade out in the spectrum. The low spatial frequencies vanish in between $1530 \leq \lambda \leq 1540$ nm what corresponds to the figures 4.14 (l)–(n) where the undulations rinse out. Close around $\lambda = 1555$ nm the low frequencies up to $1/a$ again get stronger. At 1535 nm the spectrum does not seem to contain light undulations.

A record from an uncoated tip in figure 4.19 shows a minimum at 1530 nm and a maximum at 1550 nm, i.e. each 5 nm below the wavelength corresponding to the figure series 4.14.

In figure 4.15 (b) the FFT spectrum for a W1 is shown from 3D FDTD simulation data (performed by K. Rauscher [172]) by only taking the wavelength 1480, 1485, 1500, 1505, 1535, 1550 and 1560 nm into account for reasons of calculation time. Missing data points are interpolated in the figure. The simulated data shows much higher spatial frequencies. This will be discussed later (see section 4.4.3).

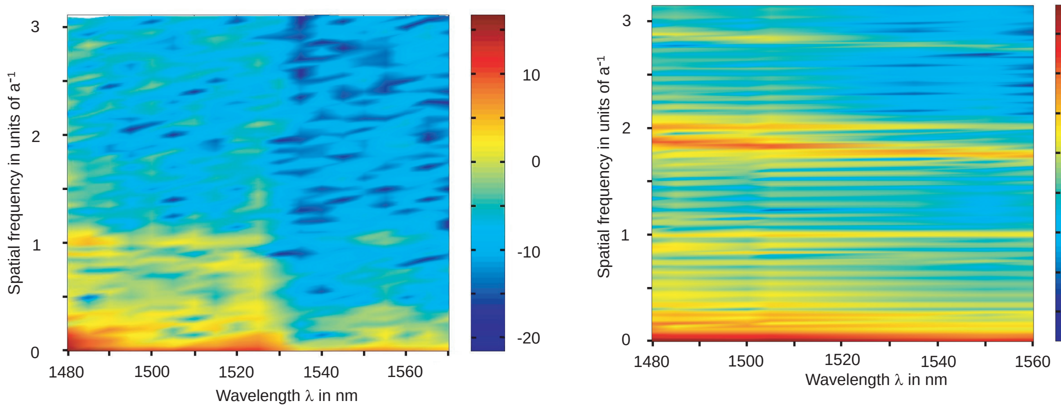

(a) FFT of the measurement data

(b) FFT of the FDTD simulation

Figure 4.15: (a) FFT for $1480 \leq \lambda \leq 1570$ nm of the W1 waveguide in figure 4.14. For example, the peak at 2 for specific wavelengths means a periodicity of $a/2$. The large peak at zero is the DC spike. The spectrum signal is in dB units. (b) shows the same data from an FDTD simulation. Note that not all wavelength of the measurement were taken into account.

The comparison of the maximum intensities over wavelength in the W1 waveguide is given in figure 4.16 where (a) shows the FDTD simulation data and (b) the measurement data. The intensities are normalized to the global maximum. Correspondence between both is a maximum relative intensity at $\lambda = 1480$ nm and a general trend of decay for increasing wavelength. Furthermore there is a minimum and an increase in intensity again, but the wavelengths are shifted with respect to each other (1550 nm in the simulation and 1535 nm in the measurement). The scale varies by one order in dB that means a factor of 10 between the simulated intensity and the intensity in the measurement.

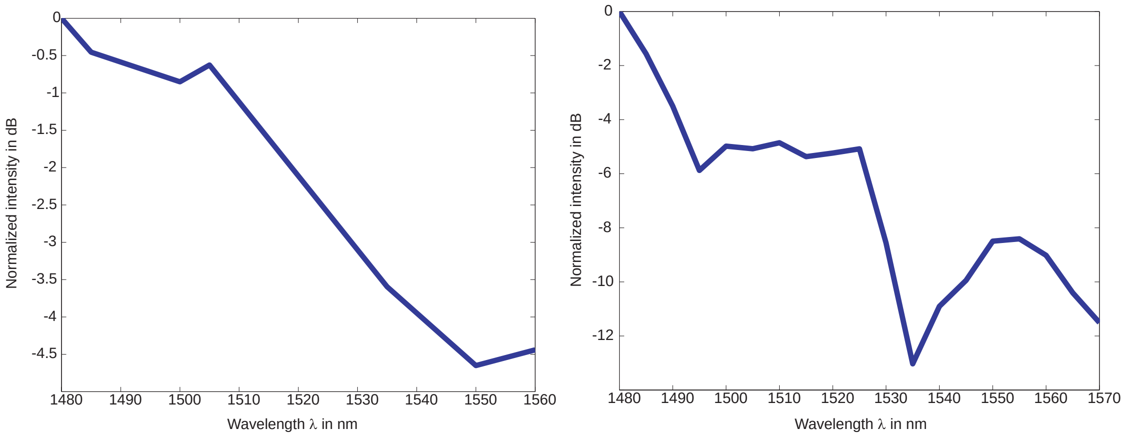

(a) Simulation (b) Measurement

Figure 4.16: The maximum intensities in the W1 waveguide normalized to the global maximum.

A shot from the 3D FDTD simulation of the W1 illustrates figure 4.17 for the corresponding wavelengths.

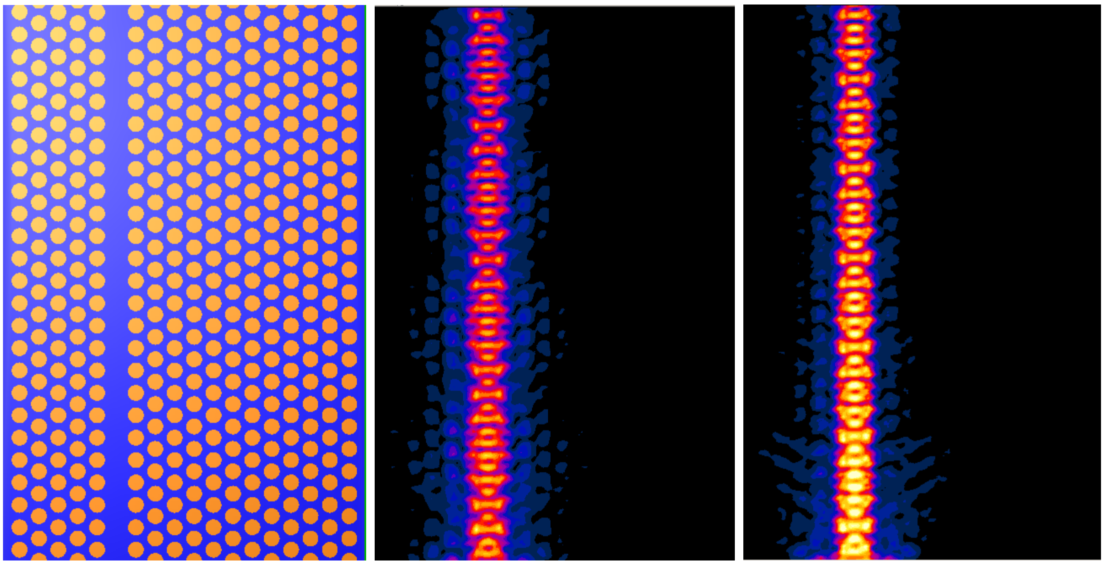

(a) Lattice (b) $\lambda = 1505$ nm (c) $\lambda = 1550$ nm

Figure 4.17: (a) The W1 waveguide and the triangular lattice without field. (b) and (c) show the root mean square of the electric field on the sample surface in TE mode. The simulation was performed by K. Rauscher [172].

For a better understanding of the intensity distribution over wavelength in the W1 waveguide in figure 4.14, the junction of the W3 disemboguing into the W1 waveguide was scanned. The scan series showed strong light scattering at the waveguide junction, also notable in constant height mode (CHM). This was a perturbation for the comparison of the signals in the W1 to the W3. To cope with that problem, the cross sections in the W1 were cut as illustrated in figure 4.18.

Figure 4.18 locates the cross sections taken inside a W3 waveguide with fixed length and outside a W1 waveguide variable in length. The W1 cross section is fixed to the end and has a total length of 69 units that are stepwise 50 times cut down by one unit in the direction of the red/blue arrow

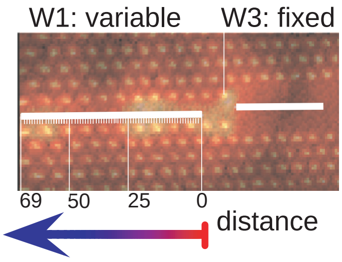

Figure 4.18: Location of the cross sections for all wavelengths in the W1 and W3. The analysis of the intensity ratio is given in figure 4.19. The original was recorded with an uncoated tip at $\lambda = 1495$ nm in TE polarization and is overlayed with the topography.

in figure 4.18. The analysis revealed small offsets between the scans at different wavelengths that is most likely due to hysteresis of the scan piezo. A plot of the results is given in figure 4.19. At $\lambda = 1535$ nm the intensity drops to the smallest value in correspondence to the fade out of the undulation pattern in figure 4.14. The same similarity is observed for the increase in intensity close to $\lambda = 1550$ nm. The measurement in figure 4.19 was recorded with a coated tip whereas the tip for figure 4.14 was not coated. Both series were taken in TE polarization.

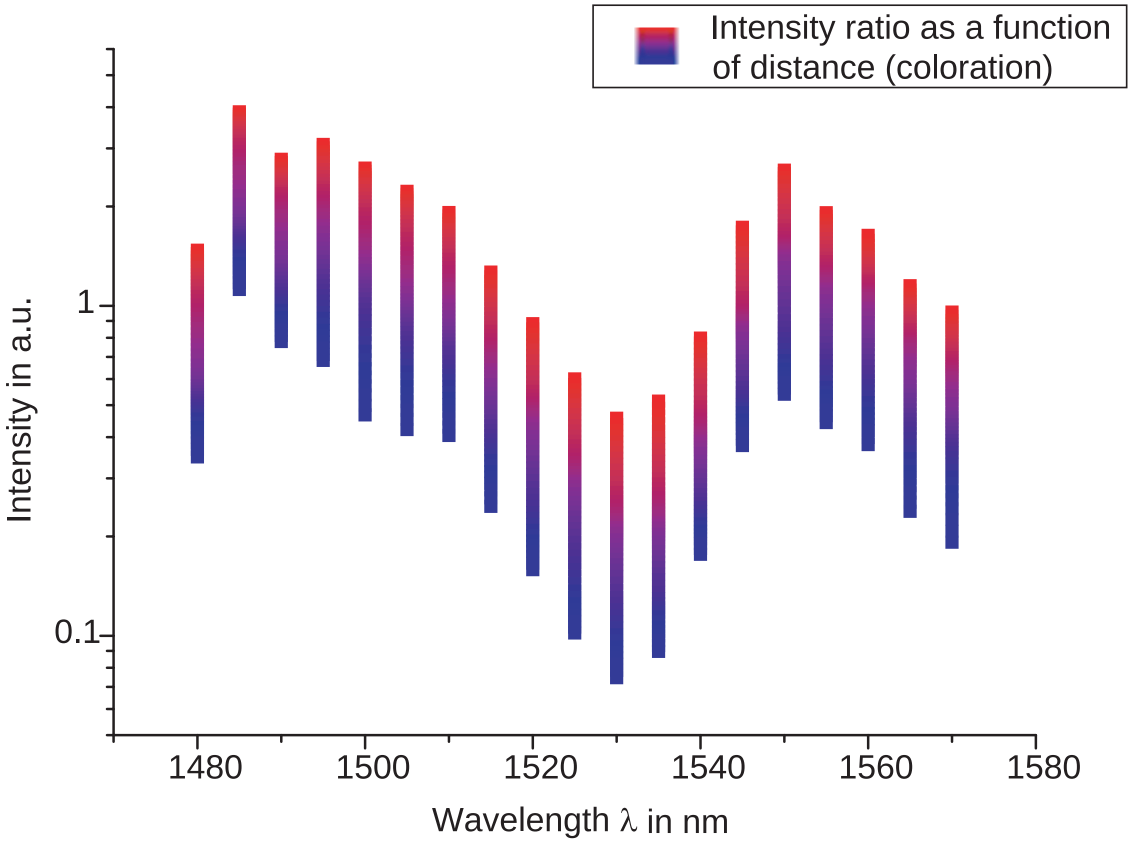

Figure 4.19: Shown is the ratio of the mean intensity in the W1 to the W3 waveguide. A single color in the vertical bars represents a single cross section as shown in figure 4.18. It shows the same trend for all wavelengths investigated by very similar coloration and length of the bars.

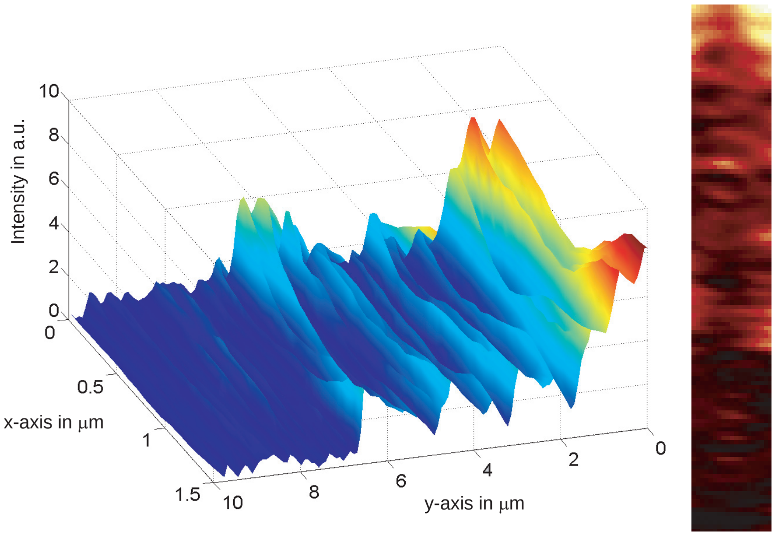

(a) 3D image of the intensity in the ridge waveguide

(b) Raw data

Figure 4.20: Data from a scan taken on the ridge waveguide in close vicinity to the W3 waveguide.

In addition to the SNOM measurements on the PHC also scans on the ridge waveguide which guides the light from the in–coupling area to the PHC have been performed with an uncoated tip. Figure 4.20 (a) shows the raw data from (a) in a 3D plot. An FFT analysis shows that there are undulations with a periodicity about 255 nm in the wavelength. In a 2D model the modes for a multilayer waveguide are calculated by the effective index approximation [173]. The calculation shows that the waveguide supports four modes that have approximately the same undulation period. A comparison of the refractive indices from the data to the reference in table 4.3 it deviates by 13 percent.

Mode	Undulation in nm	Effective refractive index
TE00	235	3.24
TE01	238	3.20
TM00	238	3.20
TM01	241	3.16
Data	256	2.98

Table 4.2: Undulations in the ridge waveguide

4.4.3 Discussion

The 3D modelling in figure 4.17 also show light undulations, clearly shown in the FFT analysis 4.15 (b). In reference to the high spatial frequencies ($> a^{-1}$) that do not appear in the FFT of the measurement data 4.15 (a), the comparison thus suggests a limitation to the optical resolution, because the SNOM was obviously not capable of resolving the high spatial frequencies.

In terms of “mechanical” resolution i.e. vibrations and the mechanics these cannot be excluded (like vibrations, noise, etc.) but are expected to be small: Acoustic noise and motion close to the optical table was avoided during scans, because the effects were immediately recorded from the oscilloscope. For the future however, a boxed design would also be imaginable in addition to avoid noise accidents and air flow. The piezo control is not expected to have a notable effect: According to specifications of the piezo [12] the resolution of 1/100 nm might be too optimistic, because generally this resolution is limited by the noise of the control system (power supply, amplifier, etc.). For example a noise of 10 millivolts in the primary power supply would limit the piezo resolution to the order of 10 nm. The dithering of the tip itself is expected to be in the picometer range [121] and therefore some orders of magnitude below the optical resolution.

The topography (see figure 4.14 (a)) shows about 20 holes. The lattice constant is well known to be $a = 450$ nm for this sample, thus suggesting a resolution of 0.32 times a. In conclusion, the resolution of the scan data does not limit the FFT. In theory, the FFT resolves 125 pixels per 10 µm what yields a resolution of a maximum 0.35 times the lattice constant a with respect to the Nyquist theorem (see appendix E). Actually, the coated tip itself can be seen as a factor of limitation: An uncoated tip collects by the taper cone [1] and therefore cannot resolve as fine details as a coated in the measurements, as it can be seen e.g. in figure 4.13. On the one hand, a coated tip has at least an aperture that is in the order of the skin depth of the metal coating, and therefore collects from a much smaller area. On the other hand, the capability of the aperture for transmission decreases and therefore reduces the signal.

In the FFT spectrum from the measurements, figure 4.15 (a), the spatial frequencies greater than the inverse lattice constant a^{-1} do not occur as distinct as in the simulated spectrum figure 4.15 (b). The spectrum shows that the optical resolution in the SNOM measurements was about $\lambda/3$, compared to the free space wavelength. This resolution is certainly below the diffraction limit of far–field microscopy. Further improvement will be required to resolve the higher spatial frequencies found in the model.

The scans concerning the W3 to W1 waveguide coupling cannot be rigorously taken as a clue for the coupling because the length of the W3 waveguide is too short rather suggesting to function as a sort of a resonator of low Q. Figure 4.19 nevertheless shows a stability of the shape by a similarity of the coloring and length of the vertical bars. The change in the light ratio passing from W3 to W1 can be put in correspondence to figure 4.14 respectively the FFT analysis 4.15 (a) because they reveal the same trend for the wavelengths relatively shifted by 5 nm.

4.4.4 Outlook

Further FDTD simulations could be performed in addition for the missing wavelengths and that also take more parameters into account i.e. deviations in the hole size uniformity, although this would be time consuming to some extend.

A rigorous analysis of the 3D FDTD simulation data could be performed that takes the tip resolution into account to fit the experimental data, but the dependence between the two is rather nonlinear therefore a simple convolution is just a model and does not yield the experimental data.

Further suggestions and improvements might be:

- Polarization dependent measurements: The setup could be extended to perform measurements with the tunable laser source in mixed polarization states to check if the black lines next to the waveguide in figure 4.14 are due to interference effects.

- Increase in wavelength tunability: In terms of dimensionless units $\omega a/2\pi c$ the wavelength range $1480 \leq \lambda \leq 1570$ nm only covers 0.29 to 0.30, which is pretty small for assignment of waveguide modes to the band structure.

- The band structure itself should be calculated. The analysis of the measurement did also not allow to link the light undulations to the Bloch harmonics and therefore to label the propagation constant of a travelling wave inside a PHC.

- To improve the quality of the PHC structures, these can be furnished with a cladding to confine the light by TIR in the vertical direction of the slab waveguide [174]. Another issue would be bridge structures that have air on both sides above and under the slab. They should show better guiding properties for symmetry reasons of the equalized index contrast. Such structures are in development [168].

- Another suggestion for improvement is the substitution of the existing positioning system by an element with an integrated measurement system. Compared to the present system, the hysteresis and creep could be reduced. Artifacts like the distortions in figure 4.13 could be avoided. Friction and hysteresis caused by connector cables [175] therefore would be compensated. According to specifications [12], temperature drift has also an effect but in comparison of time of temperature change in the lab to the scanning time this is expected to be negligible. An overnight drift of 1 micron was noticed that could be due to some mechanical creep of the micrometer heads that were used for coarse positioning the 3DP.
- Interferometric measurements that are sensitive to the light phase.

4.5 Polymer based samples

4.5.1 Photonic crystal samples from the TUHH

Another institute of collaboration is the *Technische Universität Hamburg–Harburg* that provided PHC slab waveguides of a moderate refractive index ($n \leq 2$) contrast by using polymers. In comparison to high index material like InP the optical wavelength inside the waveguide core is longer and the confinement weaker [176]. These crystals have larger core and mode dimensions that should make alignment for in–coupling easier compared to high index contrast PHCs. It is suggested, that light coupling from lensed silica fibers ($n = 1.45$) would be better mode matched and undergo less Fresnel reflection at the interfaces because of the comparable refractive indices [177]. For other reasons these materials are quite favorable i.e. very low intrinsic losses, easy processing (spincoating) and structuring of PHCs. The use of electro–optical materials would also allow the fabrication of tunable structures. The fabrication process is depicted in figure 4.21 and electron microscope images of the structures are shown in figure 4.22.

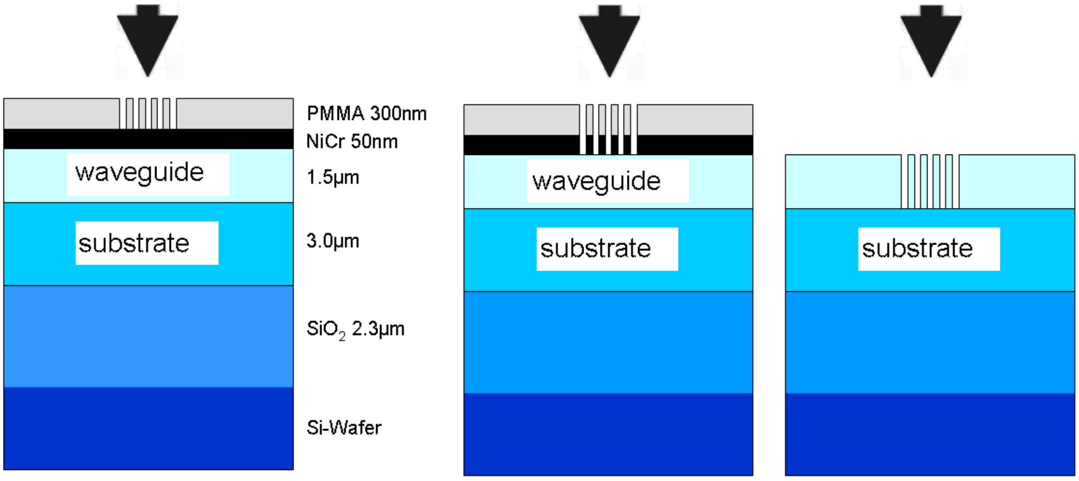

(a) E–beam and resist development (b) IBE with argon ions (c) RIE (O_2/CF_4) and wet etching

Figure 4.21: The fabrication process described in the text depicted schematically in 3 steps [178].

The PHC slab samples were fabricated (see figure 4.21 (a)–(c)) by spincoating 2.5 µm Teflon substrate on an oxidized silicon wafer (2.5 µm of oxide) and on it a Benzocyclobutene polymer (BCB) layer of 1.5 µm thickness [179]. After that, 0.5 µm of NiCr–metal as a masking layer for etching and on top a cover of 0.3 µm PMMA resist. The structuring was done by E–beam lithography and transferred into the metal mask by Ar ion beam etching (IBE). RIE (O_2/CF_4) was used for deep etching (about 2 µm) into the waveguide core and below. Finally the NiCr mask was removed by wet etching. The samples had a square lattice structure with a period of $a = 500$ nm and a hole radius of $r = 150$ nm.

Further details of the fabrication process, transmission measurements and theoretical studies can be found in the references [177, 178, 180].

Material	**Refractive Index**	**Reference**
InP	3.15	[168]
InGaAsP	3.45	[168]
Teflon	1.30	[180]
BCB	1.54	[180]

Table 4.3: Compilation of refractive indices of different materials in the NIR wavelength range

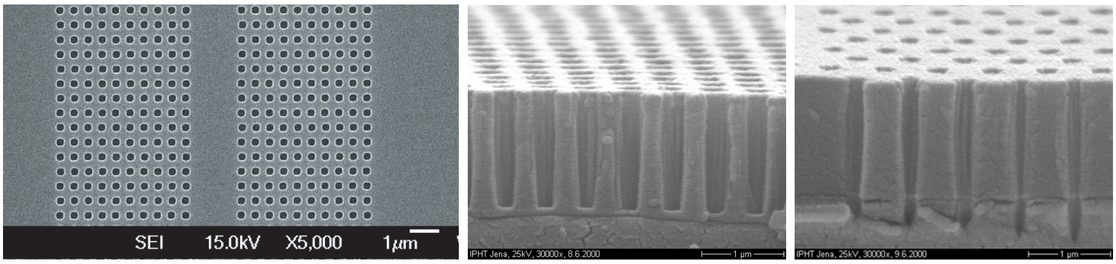

(a) 1D 10_3_10 resonator (b) Etching profile (c) Deep etching into the substrate

Figure 4.22: Electron microscope images of a resonator device and the etching of the PHC structures (TUHH). The images have been kindly provided by M. Schmidt [178, 179].

4.5.2 Investigation of the TUHH PHC samples

Basically the setup had a very similar layout, except for the method of the light in–coupling. The PHC sample was mounted onto a single mode fiber launch system for 3D fine adjustment. The setup and beam path is depicted in figure 4.23. Details on optical components are given in the tables D.1, D.2 and on devices in table C.2. Figure 2.2 illustrates schematically the servo loop for distance control.

A laser at $\lambda = 1310$ nm was used for the in–coupling. The red HeNe laser was used for alignment purposes. The waveplates allowed to adjust the laser light polarization and finally the light was focussed into a prism. Several strategies were tried to contact the prism to the wafer. A ball bearing pushed into the back of the wafer gave good contact, however the contact point was too small. Eventually an index matching fluid (Diiodomethane (CH_2I_2), for details see table D.2) was used to give optical contact over the whole prism surface and therefore assisted light coupling. Ideally the index matching fluid should satisfy the following:

- Its refractive index should be between the refractive indices of the prism and the waveguide polymer (index matching)
- It should not corrode any material (polymer, prism, glue) in its close adjacency
- It should be removable by a solvent which is neither corrosive to the polymer of the sample nor the prism

(CH_2I_2) fulfilled all requirements except one. It was found to dissolve the 2–part epoxy glue, used to hold the prism in the mount.

The angle for the in–coupling had a certain acceptance and was determined geometrically by the TIR condition at the interfaces. For the final configuration the acceptance angle ranged from $-4°$ to $-59.5°$ ($\approx 55.5°$) from top view in figure 4.23. The in–coupling could be recognized when the beam was in the plane of the waveguide slab. To visualize this, an IR viewer or the visible laser was used respectively.

Figure 4.25 shows the recorded signal for a 1D resonator, as depicted in figure 4.22 (a). The structure under investigation had a wall of seven lattice constants, a defect of two rows, then seven lattice constants. This is referred to as a 7_2_7 resonator. The transmission measurements provided by M. Schmidt in figure 4.24 show a peak at 1310 nm for TM polarization and around 1290 nm for TE. Measurements at 1310 nm have been performed where the available laser source matched the wavelength of the peak

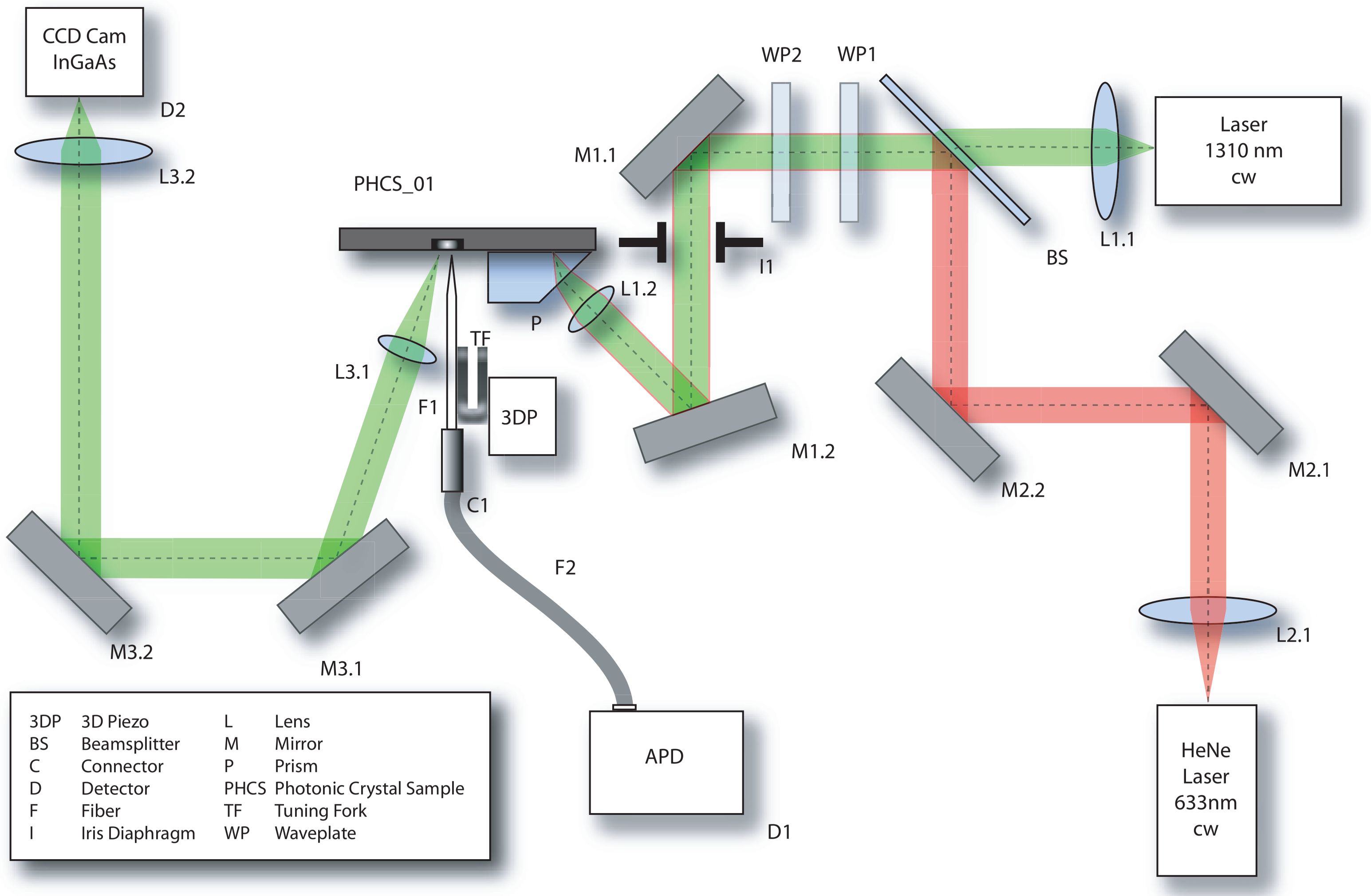

Figure 4.23: Beam path of the experimental setup in configuration for prism coupling

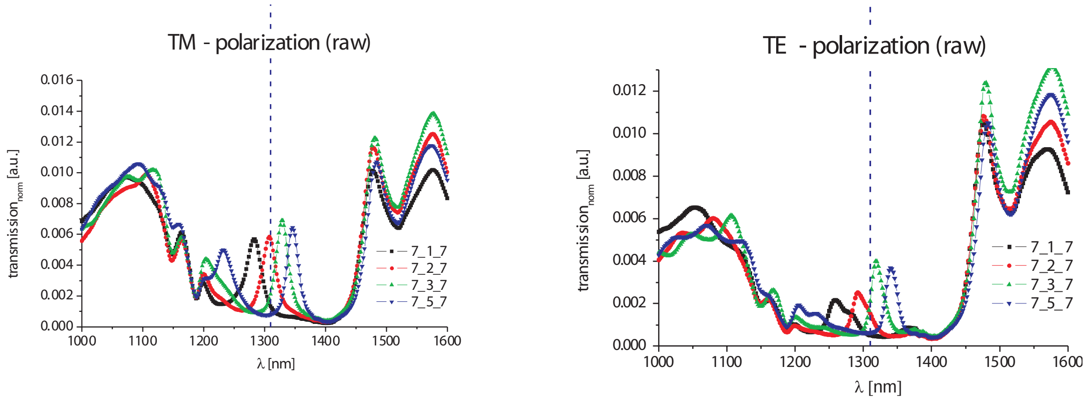

(a) TM polarization (b) TE polarization

Figure 4.24: Transmission spectra in dependence of the resonator size and polarization (from [179]).

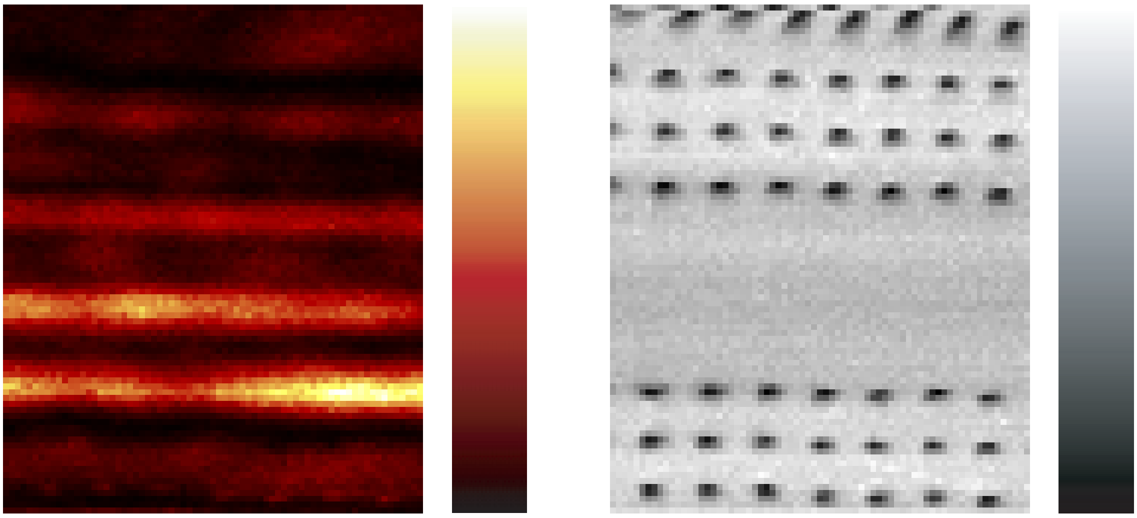

(a) Optical signal (b) Topography

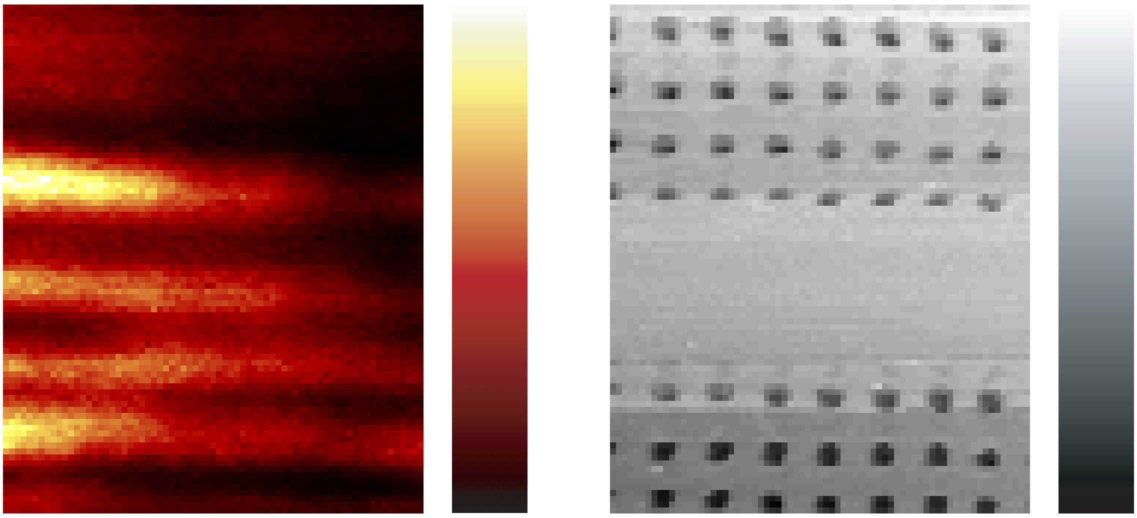

(c) Optical signal (d) Topography

Figure 4.25: (a) and (c): Optical image of an 1D 7_2_7 resonator based on a BCB polymer slab. The images were recorded with an uncoated tip at $\lambda = 1310$ nm in TM polarization.

4.5.3 Discussion

Measurements for the 7_2_7 resonator structure have been performed at $\lambda = 1310$ nm in TM polarization which matches the intensity peak in transmission at $\lambda = 1312$ nm (see figure 4.24). The resonator is expected from theoretical calculations to show two antinodes inside the resonator [179]. Figure 4.25 (a) and (c) show SNOM measurements. Bright scattering due to the holes can be distinguished in the place of the front and back row of holes of the resonator. Due to the lack of a tunable laser source, spectroscopy was not possible at this time and made the experiment inconclusive.

4.5.4 Outlook

Improvements are expected to be achieved by:

- A tunable laser source around 1250–1350 nm that matches the wavelength range of the resonances in the transmission spectra (see figure 4.24) would be favorable to allow spectroscopy and systematic measurements at the exact resonance frequency where the resonator acts as a Fabry-Perot filter (seen from the transmission spectra, figure 4.24). The quality factor Q could be measured by SNOM and compared to the results from the conventional measurement [176, 179].

- More space in a different design of the sample i.e. a ridge waveguides that lead to the PHC resonator and away could be used to manipulate the resonator properties by a second SNOM probe.

- Interferometric measurements that are sensitive to the light phase.

Zusammenfassung

Im Rahmen einer Diplomarbeit der *Universität Konstanz*, die extern an der *Eidgenössischen Technischen Hochschule Zürich* (ETH) durchgeführt wurde, stand die hochaufgelöste Untersuchung optischer Eigenschaften von photonischen Kristallen mittels Rastersonden–Nahfeldmikroskopie (SNOM) im Mittelpunkt. Die Proben photonischer Kristalle für den Telekommunikationswellenlängebereich 1.3–1.5 µm wurden von Forschungsgruppen der *Technischen Universität Hamburg–Harburg* (TUHH), sowie der ETH zur Verfügung gestellt. Die untersuchten Proben waren von unterschiedlicher Geometrie, basierend auf verschiedenen Materialien und Herstellungtechniken. Es ist Ziel, in Zukunft optische Systeme auf kleinstem Raum integrieren zu können und diese mit elektrischen und/oder fluiden Systemen zu kombinieren.

Physikalisch gesehen, hat die Lichtausbreitung in einem photonischen Kristall sehr viel Ähnlichkeit mit der Ausbreitung von Wellen in einem kristallinen Festkörper, wenn die Leitungselektronen als Wellen aufgefasst werden. Photonische Kristalle sind Strukturen mit einem räumlich periodisch modulierten Brechungsindex. Die Längenskala der Modulation ist von gleicher Größenordnung wie die Wellenlänge des Lichts. Ist die Größe des Brechungsindexkontrasts ausreichend, so verbietet Braggreflexion bestimmte Ausbreitungsrichtungen und Frequenzbereiche der Photonen. Um eine vollständige Bandlücke im Sinne aller möglichen Ausbreitungsrichtungen und Polarisationen zu erhalten, müssen jedoch noch mehr Bedingungen erfüllt sein. Zum Beispiel sind nicht alle Kristallstrukturen dafür geeignet. Die in dieser Arbeit untersuchten photonischen Kristalle sind zweidimensionale Schichtsysteme; das heißt sie besitzen nur in einer Ebene eine Bandlücke, da der herstellungstechnische Aufwand derzeit dafür geringer ist als für dreidimensionale Strukturen.

Auf der einen Seite ist man darum bemüht, möglichst perfekte photonische Kristalle herzustellen, auf der anderen Seite erlauben es gezielt eingebaute Gitterfehlstellen Licht zu lokalisieren und zwar auf einer Längenskala die kleiner als die Lichtwellenlänge ist. Beispiele für derartige Defekte sind zum Beispiel Punktdefekte, welche als frequenzselektive Filter wirken können. Liniendefekte können benutzt werden, um daraus Wellenleiter zu bilden.

Die herkömmliche Mikroskopie bildet das Licht ab, welches von einer Probe weggestreut wird. Ihre Auflösung ist beschränkt durch Lichtbeugung und kann deswegen nicht die Einzelheiten der Muster offenbaren, welche das eingesperrte Licht in Defektstellen photonischer Kristalle hat.

Die zur Untersuchung gebrauchten Nahfeldsonden wurden selbst hergestellt, indem ein CO_2–Laser eine entmantelte Glasfaser lokal erhitzte und eine Maschine diese mit bestimmten Zugparametern entzweite. Die so hergestellten Faserspitzen und ihre Form wurden sowohl unter einem optischen und einem Elektronenmikroskop geprüft, als auch ihre elektrischen und optischen Eigenschaften in einem eigens dafür aufgebauten Testsystem systematisch kontrolliert, und die Zugparameter variiert. Verschiedene Metallbeschichtungen der Faserspitzen wurden in einer Bedampfungsanlage ebenfalls selbst durchgeführt. Eine alternative Kontrolle der Faserspitzen war das Abrastern einer Probe von AFM Spitzen die eine Höhe von 10 nm hatten und somit die Topographie der Nahfeldsonde lieferten.

Bei der Probe von der TUHH handelte es sich um einen eindimensionalen Resonator auf Polymerbasis. Das von der Theorie vorhergesagte und simulierte Stehwellenmuster wurde jedoch im Resonator nicht beobachtet. Die dabei verwendete Laserwellenlänge lag 2 nm nebem der Resonanzfrequenz, bei welcher der Resonator als Fabry–Perot Filter wirkt. Da zu dem Zeitpunkt der Messungen noch keine in der Wellenlänge durchstimmbare Laserquelle zur Verfügung stand, konnten keine spektroskopischen Messungen an der Probe durchgeführt werden. Generell hat sich bei dieser Untersuchung gezeigt, daß die Lichteinkopplung über ein Prisma in das Schichtsystem und die Detektion im Nahfeld durchführbar sind.

Für die Proben photonischer Kristalle von der ETH stand im Laufe der Messungen eine durch-

stimmbare Laserquelle zur Verfügung. Messungen an einer ersten Testprobe, bei der aufgrund der noch nicht optimierten Herstellung keine Bandlücke erwartet wurde, bestätigte dies. Dennoch zeigten die Aufnahmen des Nahfeldes, dass die Probe aufgrund der Beschaffenheit des Brechungsindex das Licht leiten kann. Für die zweite Probe wurde die geometrische Anordnung der photonischen Kristalle auf der Probe modifiziert, um störendes Streulicht von der Einkopplung zu reduzieren. Der Laserfokus ist beschränkt durch Beugung und überlappt den Einkopplungsbereich, welcher aufgrund des hohen Brechungsindex dieser Probe kleiner als das Limit der Beugung ist. Für die Messungen dieser Probe wurden folgende Ziele erreicht:

- Die aufgenommenen Bilder zeigen eine Auflösung, die unter dem Beugungslimit ist.
- Die Transmission an Verbindungen zwischen einem W3 und einem W1 Wellenleiter wurde studiert. Die Zahl steht für die Anzahl der Liniendefekte, die direkt nebeneinander liegen und so einen Wellenleiter bilden. Die Analyse zeigt, dass ein Intensitätsminimum für eine spezifische Wellenlänge existiert, welches allerdings nicht mit dem Ergebnis einer dreidimensionalen Simulation ist. Die Simulation, nach der Methode der *Finite–Difference Time–Domain* wurde in einer zusammenarbeitenden Gruppe durchgeführt.
- Die Änderung der optischen Moden innerhalb des Wellenleiters wurden als Funktion der Wellenlänge aufgezeichnet. Im Vergleich mit einer Simulation zeigte sich in der Datenanalyse, daß die optische Auflösung etwa ein Drittel der Wellenlänge betrug.
- Messungen der Lichtmodulation im Wellenleiter, welcher auf der Probe zum photonischen Kristall hinführt konnte zur Bestimmung des effektiven Brechungsindex verwendet werden. Der erhaltene Wert stimmt mit dem Ergebnis eines Modells zu etwa 13 Prozent überein.

Acknowledgement

First of all, I would like to thank my parents. They let me chose the way by myself, potentiated my education and supported me during all the time of my studies, especially in the last year of my thesis when it became absolutely necessary.

I am grateful to Vahid who offered me the chance to do my diploma thesis in his group and to my encouraging examiner Mrs. Scheer and Mr. Marzlin from the University of Constance for their acceptance of my work and for making it possible.

Further I would like to thank all members and former members of the nano–optics group of the ETH *Laboratory of Physical Chemistry* for the good time I had there. Thank you, Juliane, Lavinia, Fereshteh, Carmen, Alois, Gert Z., Thomas, Ulf, Bob, Christian, Patrik, Klas, Sergei, Jan Z., Rob, Johannes, Gert W., Jan Z., Phillip and Parijat. Especially my colleagues in the lab, Ben and Femius, who taught me a load of useful things whenever I had a question . . . Thanks for your advices and in the end especially Ben also for some proof reading. Ilja — maybe one day I will call you by your given name when you call me on the phone, but I told you that it is hard for me — THANKS for everything !!! It is more than you might will guess. A special thank is also reserved for Hannes for his excellent software written by himself. ScanHaSee was very useful for image analysis. And Hannes' cooperation concerning any "changes" in the program was fruitful.

I would like to extend my thank to Robert Wüest of the ETH *Electronics Laboratory* for the kind collaboration and sample preparation, Katherina Rauscher of the ETH *Laboratory for Electromagnetic Fields and Microwave Electronics* for recent simulations of the experimental data and Markus Schmidt of the TUHH branch *Materials in Electrical Engineering and Optics* for providing the polymer PHC samples.

For their great support and for their help with broken devices I thank the electronic specialists at the ETH Konrad Boss, Andreas Arnold and Peter Nyfeller and also Stefan Eggert from the University of Constance for his cooperation with the Loop–Amplifier.

Another big thank goes to Bruno, the head of the workshop. I had the impression for any part I got from you that you brought the famous Swiss precision to the top neither when you were busy nor on Friday afternoon. Thanks a lot !

I also would like to thank the *"Rebhüsli group"* for the great time we had together in Zürich. I wish we would have had more time together, but the little time we spend together was great indeed. Although I believe that some of you might suspect me to live in my lab. And at last but of more importance than the order might suggest, I want to thank my friends, especially Maria, Renate, Gerhard, Thomas L. and Betty.

The Miller indices

Bragg reflection was first studied for X–ray diffraction by atoms and was later also used for layered media and gratings [68]. To assign reflections to different lattice planes of the direct lattice these can be distinguished by the crystallographic Miller indices (hkl), whose advantage is the total equivalence to the use of the reciprocal lattice vectors. This becomes clear for instance in section 3.3.4. A more thorough look on the topic can be found in the literature [181].

The Miller indices, generically denoted by (hkl), can be assigned by the following procedure:

(i) The intercepts of the face along the crystallographic axes have to be determined in terms of unit cell dimensions.

(ii) The reciprocals of these values have to be taken.

(iii) All fractions have to be cleared.

(iv) At last, the remaining values have to be reduced to lowest terms.

For an example, see figure A.1. The axis intercepts are $\mathbf{a}_1 = 3$, $\mathbf{a}_2 = 2$, and $\mathbf{a}_3 = 2$:

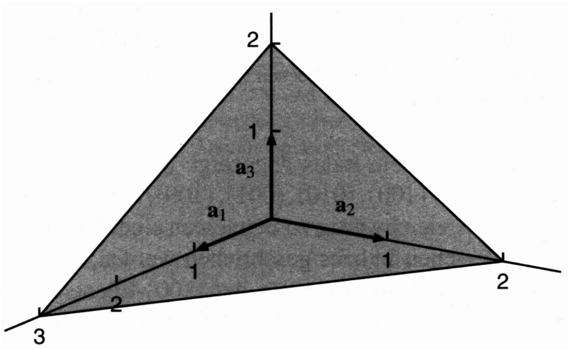

Figure A.1: The plane intersects the axes $\mathbf{a}_1$, $\mathbf{a}_2$, $\mathbf{a}_3$ at $3a_1$, $2a_2$, $2a_3$. (taken from [61]).

The Miller indices read (233), calculated from:

- Determine axes intercepts: 3, 2, 2
- Take reciprocals: $\frac{1}{3}$, $\frac{1}{2}$, $\frac{1}{2}$
- Clear fractions (i.e. multiply by 6): $2, 3, 3$
- Reduce to lowest terms (already there).

A Miller index becomes zero, if the plane does not intersect the corresponding direct lattice vector (that means interception at infinity). Negative indices for negative axes intercepts/directions are highlighted by a line drawn over it. To indicate whole families of planes in the direct lattice the specific notation {100} addresses the planes (100), (010) and (001). In the reciprocal lattice, square brackets are used for the directions: Here, the corresponding notation ⟨100⟩ indicates [100], [010], [001] and their reciprocals [$\bar{1}$00], [0$\bar{1}$0], [00$\bar{1}$]. Four Miller indices are used for the special case of hexagonal lattices.

The general {hkl} planes in the crystal lattice directly correspond to the points in the reciprocal lattice with the coefficients h, k and l (v_i in equation (3.24)). Its associated reciprocal lattice vector is perpendicular to the planes in real space.

Appendix B

Artifacts

Generally speaking, in measurements there are always artifacts. If they are negligible or not, depends on the situation how much the measurement disturbs the system compared to the ideal case when it does not. In imaging with lens systems for example one has to deal with artifacts that are due to shortcomings of the lenses or the system itself in terms of limitations.

Referred to SNOM imaging, there is also a couple of issues that make the matter more complicated. For example the topographic induced contrast in the recorded optical image could mislead to the impression of a higher resolution that could have been achieved with the same probe that scanned over a flat surface. It is due to a change in the phase difference. One has to take care of the correlations between the optical and topographical images, for example see figure B.1. In addition to the topography contrast various other mechanisms can take influence for example birefringence, different material species, index of refraction, fluorescence, reflectivity, magnetic stress, etc.

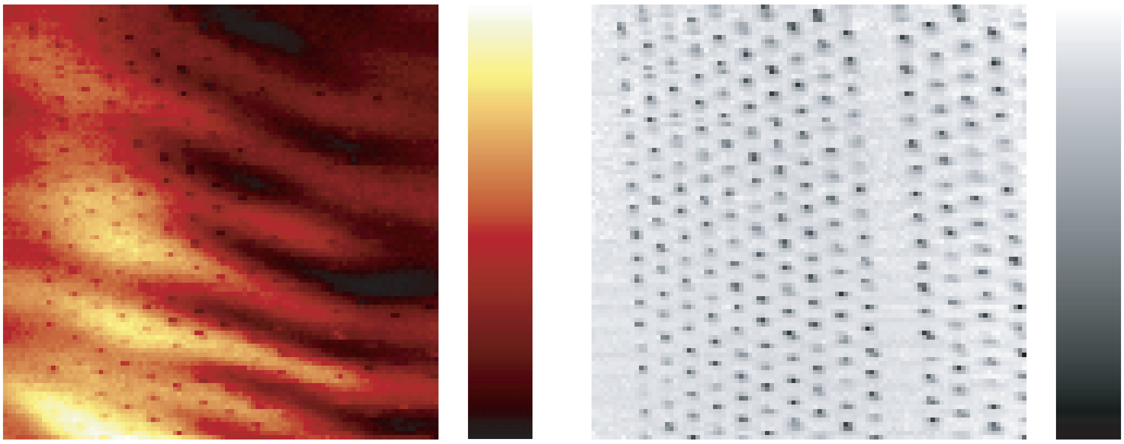
(a) Optical signal (b) Topography

Figure B.1: The scan was recorded on a test sample (ETH) without PBG in TE polarization at $\lambda = 1550$ nm with an uncoated tip. The optical signal shows the holes from the topography as an induced artifact.

The dependence between the optical and topographical image is rather nonlinear and a simple convolution is just a model. To measure the absolute resolution there is need for well–defined test samples and a precise control. It should be kept in mind that the light intensity, the polarization, the force feedback, time and the wavelength dependence contribute to the image contrast (E.g. see figure B.2: The holes appear bright *and* dark.). A detailed description is beyond this work. Further reading can be found in [1, 182–186].
Figure B.3 shows the effects of the non–linearities of the piezo scanner: The image is distorted.

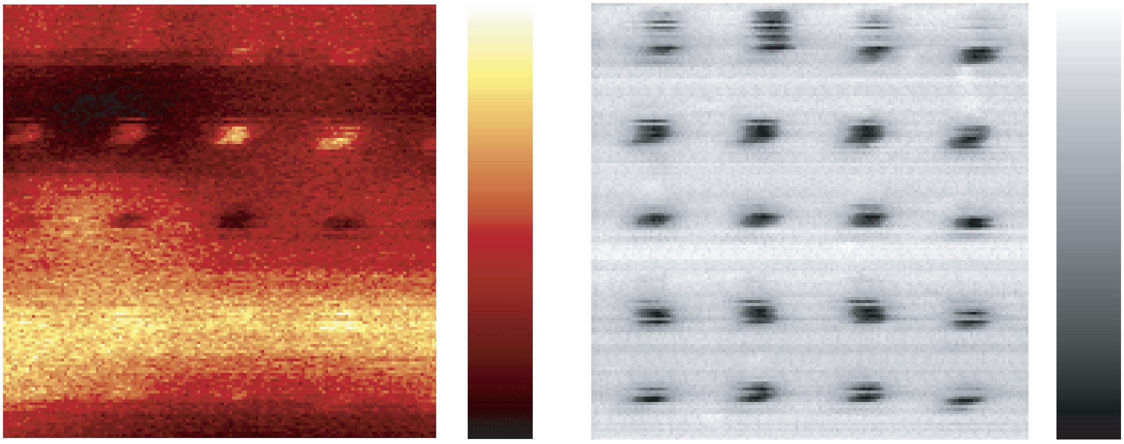

(a) Optical signal

(b) Topography

Figure B.2: The scan was recorded with an uncoated tip on a row of holes from a 1D 3–7–3 resonator (BCB, TUHH) at $\lambda = 1310$ nm (TE). The image contrast changes for the holes: They appear bright *and* dark in the optical signal.

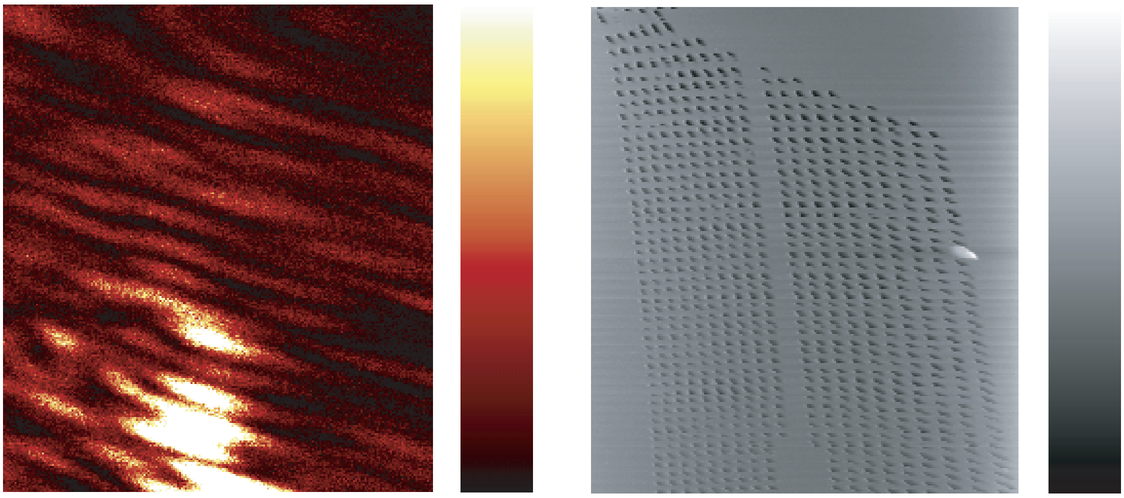

(a) Optical signal

(b) Topography

Figure B.3: The straight W1 (ETH) waveguide was scanned with an uncoated fiber tip at $\lambda =$ 1550 nm (TM). The optical image is slightly enhanced in contrast. The topography is seriously affected by the non–linearities of the piezo scanner that distort the image: The lattice should show a triangular symmetry and the crystal area rectangular.

Appendix C

Devices

The tables give a survey of the devices that have been used in the experimental setup (C.2) and in the test bench (C.1), where the fiber tips were glued onto the tuning forks. The tips have been tested there optically and and electrically. For a schematic sketch of the setup see e.g. figure 4.9 on page 34, figure 4.23 on page 47 respectively. See 2.2 for a schematic draw of the control system on page 6. The test stage is in principle build in the same way, but only used on testing purpose.

Manufacturers	Model	Description
JDS Uniphase	1507 Novette™	HeNe laser, 633 nm, 0.8 mW
EG&G™	7260 DSP	DSP lock-in amplifier
Stanford Research Systems	DS345	function/arbitrary waveform generator, frequency range: 1 µHz–30.2 MHz
Hameg	HM1507–3	two–channel analog-/digital oscilloscope, 150 MHz (200 MSa/sec)[1]

Table C.1: List of devices of the test bench

Manufacturers	Model	Description
Thorlabs Inc.	DET410	high–speed detector (PIN diode, InGaAs)[2]
id Quantique	id200	low noise single-photon detector, spectral wavelength range 1.1–1.6 µm, (APD, InGaAs/InP)
Stanford Research Systems	SR400	two–channel gated photon counter
Mitsubishi®	ML725B11F	laser diode (MQW/DFB, InGaAsP), 1.31 µm, 6 mW[3]
Mitsubishi®	ML925B11F	laser diode (MQW/DFB, InGaAsP), 1.55 µm, 6 mW[3]
Hewlett–Packard®	HP 8168D	tunable laser source (Fabry Perot–laser, InGaAsP), wavelength range 1.48–1.57 µm, <1.6 mW
CR Laser/Aerotec	CR–115B,	HeNe laser 633 nm, 2.6 mW

(Devices in the experimental setup)

continued on next page ...

---

[1] 10^6 samples per second (M = Mega).

[2] To cope with the problem of SNR, a more efficient (sensitive) detector had to be applied.

[3] Both of the laser diodes were combined with the driver iC-WK2D by Roithner Lasertechnik company.

... continued from previous page

Manufacturers	Model	Description
EG&G™/Princeton Applied Research	5301A/5317	two–phase lock-in amplifier/differential preamplifier
Hewlett–Packard®	HP 33120A	function/arbitrary waveform generator, 15 Mhz
Hameg	HM205–3	two–channel storage oscilloscope, 20 MHz
Hameg	HM407–2	two–channel analog-/digital oscilloscope, 40 MHz(100 MSa/sec)[4]
Indigo® Systems Corp.	Merlin™ NIR	thermoelectric cooled, near–wavelength infrared high–performance camera, sensitivity range 0.9–1.68 µm, 6 Mpixels/sec[5], NTSC/PAL, (FPA 320x256 matrix, InGaAs)
Bit Flow Inc.	Road Runner	frame grabber board (RUN-PCI-12), Talon Ultra data analysis software
piezosystem jena GmbH	3–D 100 NV	3D positioning system (TRITOR series), 150 V, max. range 100 µm

Table C.2: List of devices of the setup

---

[4] 10^6 samples per second (M = Mega).

[5] Mega pixels sampled per second.

Appendix D

Optical components

The optical components according to the different setup configurations are listed in the tables below. All the lenses had broadband ARCs of various types not specified in the list.

Setup	Distributor	Part Number	Focal Length	NA
L1.1	Melles–Griot	06GLC001	6.50 mm	0.615
L1.2	Thorlabs	A397-C-X	11.00 mm	0.30
L2.1	n/a	n/a	100.00 mm	0.149
L3.1	Melles–Griot	01LAL011	40.00 mm	0.188
L3.2	Thorlabs	LA1172–C	400.00 mm	0.032

Table D.1: Lenses in the experimental setup configuration 01

Setup	Distributor	Part Number	Properties
BS	n/a	n/a	50:50 beamsplitter
M1.x	R&G Co.	101212	dielectric mirror/ARCs @ 1300–1600 nm
M2.x	divers	n/a	silver mirror
M3.x	divers	n/a	silver mirror
P	R&G Co.	AR-90 SF6	prism, La6SFN, $n = 1.77$ @ 1310 nm
oil	divers	n/a	immersion oil (CH_2I_2), $n = 1.7025$ @ 1310 nm
WP1	Thorlabs	WPQ05M–1310	$\lambda/4$ waveplate @ 1310 nm
WP2	Thorlabs	WPH05M–1310	$\lambda/2$ waveplate @ 1310 nm

Table D.2: Optical components in the experimental setup configuration 01

Continued on the next page.

Setup	Distributor	Part Number	Focal Length	NA
L1.1	Melles–Griot	06GLC001	6.50 mm	0.615
L1.2	Thorlabs	C330TM–C	3.10 mm	0.68
L2.1	n/a	n/a	100.00 mm	0.149
L3.1	Melles–Griot	01LAL011	40.00 mm	0.188
L3.2	Thorlabs	LA1172–C	400.00 mm	0.032

Table D.3: Lenses in the experimental setup configuration 02

Setup	Distributor	Part Number	Properties
BS	self–made	n/a	50:50 beamsplitter, Au onto Cr coated coverslip
M1.x	R&G Co.	101212	dielectric mirror/ARCs @ 1300–1600 nm
M2.x	divers	n/a	silver mirror
M3.x	divers	n/a	silver mirror
PBS	Melles–Griot	03PBS083	polarizing beamsplitter cube @ 1550 nm
WP1	Thorlabs	WPQ05M–1550	$\lambda/4$–waveplate @ 1550 nm
WP2	Thorlabs	WPH05M–1550	$\lambda/2$–waveplate @ 1550 nm

Table D.4: Optical components in the experimental setup configuration 02

Appendix E

Program listings

For data analysis and evaluation several program listings amongst other things for Matlab® (and Mathematica®) have been written within the scope of this thesis. An example will be listed for a fast Fourier Transform (FFT), with respect to the Nyquist theorem, of an optical signal calibrated to the topography. It is printed on the following page for a better survey.

The Nyquist theorem is defined by:

> *An analog signal waveform may be uniquely reconstructed without error from samples taken at equal time intervals. The sampling rate must be equal to, or greater than, twice the highest frequency component in the analog signal.*

```
%%% input
 Filename_1   =  ’Filename cross–section topography’;
 Filename_2   =  ’Filename cross–section optical’;

%%% process

%%% topography and offset params
 x_off    =  [109 0;0 0;0 0];  % ref x + difference between the cross--sections
 y        =  [416 170];        % ref y
 x_step   =  18;
 slant    =  -12;

 for b        =  2:max(length(x_off(:,1)))
 x_off(b,1)   =  x_off(b-1,1) + x_step;
 end;

 x_off(:,2)          =  x_off(:,1) + slant;         % pix difference corresponds to Xsection slant
 topo_1              =  load([filename_1,num2str(x_off(1,1)),’,’,num2str(y(1,1)),’)-(’,num2str(x_off(1,2)),’,’,num2str(y(1,2)),’).txt’]);
 topo_2              =  load([filename_1,num2str(x_off(2,1)),’,’,num2str(y(1,1)),’)-(’,num2str(x_off(2,2)),’,’,num2str(y(1,2)),’).txt’]);
 topo                =  (topo_1 + topo_2)/2;
 nsamples_topo       =  size(topo,1);
 distance_topo       =  abs(topo(1,1)-topo(nsamples_topo,1));
 sample_freq_topo    =  nsamples_topo/distance_topo;

 fft_topo               =  fftshift(abs(fft(topo(:,2)-mean(topo(:,2)))));
 freq_topo              =  linspace(-sample_freq_topo/2, sample_freq_topo/2, nsamples_topo);
 [val_topo,dex_topo]    =  max(fft_topo);
 topo_cal               =  abs(freq_topo(dex_topo));

%%% optics (inside wg)
 x_off    =  [115 0;0 0;0 0];  % ref x + difference between the cross--sections
 y        =  [416 171];        % ref y
 x_step   =  3;
 slant    =  -12;
```

```
 for b          =   2:max(length(x_off(:,1)))
 x_off(b,1)     =   x_off(b-1,1) + x_step;
 end;

 x_off(:,2)          =   x_off(:,1) + slant;         % pix difference corresponds to cross--section slant
 opt_w1_1            =   load([filename_2,num2str(x_off(1,1)),’,’,num2str(y(1,1)),’)-(’,num2str(x_off(1,2)),’,’,num2str(y(1,2)),’).txt’]);
 opt_w1_2            =   load([filename_2,num2str(x_off(2,1)),’,’,num2str(y(1,1)),’)-(’,num2str(x_off(2,2)),’,’,num2str(y(1,2)),’).txt’]);
 opt_w1_3            =   load([filename_2,num2str(x_off(3,1)),’,’,num2str(y(1,1)),’)-(’,num2str(x_off(3,2)),’,’,num2str(y(1,2)),’).txt’]);
 opt                 =   (opt_w1_1 + opt_w1_2 + opt_w1_3)/3;
 nsamples_opt        =   size(opt,1);
 distance_opt        =   abs(opt(1,1)-opt(nsamples_opt,1));
 sample_freq_opt     =   nsamples_opt/distance_opt;

 fft_opt             =   fftshift(abs(fft(opt(:,2)-mean(opt(:,2)))));         % get rid of the dc spike
 freq_opt            =   linspace(-sample_freq_opt/2, sample_freq_opt/2,nsamples_opt);
 [val_opt,dex_opt]   =   max(fft_opt);

%%% plot fft optical signal (cal) at lambda (inside)
 fig_name    =   get(0,’CurrentFigure’);   figure(’Name’,[’FFT of the optical signal (normalized to topo) inside’])
plot(freq_opt/topo_cal, (fft_opt))

%%% optics (outside wg)
 x_off     =   [103 0;0 0;0 0];   % ref x + difference between the cross--sections
 y         =   [416 171];         % ref y
 x_step    =   45;
 slant     =   -12;

 for b          =   2:max(length(x_off(:,1)))
 x_off(b,1)     =   x_off(b-1,1) + x_step;
 end;

 x_off(:,2)   =   x_off(:,1) + slant;         % pix difference corresponds to cross--section slant
 opt_w1_1     =   load([filename_2,num2str(x_off(1,1)),’,’,num2str(y(1,1)),’)-(’,num2str(x_off(1,2)),’,’,num2str(y(1,2)),’).txt’]);
 opt_w1_2     =   load([filename_2,num2str(x_off(2,1)),’,’,num2str(y(1,1)),’)-(’,num2str(x_off(2,2)),’,’,num2str(y(1,2)),’).txt’]);
```

```
  opt                 =   (opt_w1_1 + opt_w1_2)/2;
  nsamples_opt        =   size(opt,1);
  distance_opt        =   abs(opt(1,1)-opt(nsamples_opt,1));
  sample_freq_opt     =   nsamples_opt/distance_opt;
  fft_opt             =   fftshift(abs(fft(opt(:,2)-mean(opt(:,2)))));        % get rid of the dc spike
  freq_opt            =   linspace(-sample_freq_opt/2, sample_freq_opt/2,nsamples_opt);
  [val_opt,dex_opt]   =   max(fft_opt);

%%% plot fft optical signal (cal) at lambda (outside)
  fig_name   =   get(0,'CurrentFigure');   figure('Name',['FFT of the optical signal (normalized to topo) outside'])
plot(freq_opt/topo_cal, (fft_opt))
result2(:,1) = (freq_opt')/topo_cal ; result2(:,2) = fft_opt ; lambda = 1550; lambda_txt = num2str(lambda);
save([lambda_txt,'_wg_w1_(TE)_fft.txt'],'result2','-ascii','-tabs');

end;
```

Appendix F

Abbreviations

Abbreviation	Description	Page
1D, 2D and 3D	**1**–, **2**– and **3**–**d**imensional	15
3DP	**3**–**d**imensional **p**iezo scanner	34
AD	**a**nno **D**omini (Latin)	3
AFM	**a**tomic **f**orce **m**icroscope	5
ARC	**a**nti–**r**eflection **c**oating	15
APD	**a**valanche **p**hoto**d**iode	34
BCB	**B**enzo**c**yclo**b**utene (polymer)	45
bcc	**b**ody–**c**entered **c**ubic	19
C	**c**entered (unit cell: additional point in the center of each end)	19
CCD	**c**harge **c**oupled **d**evice	34
CGM	**c**onstant **g**ap width **m**ode	8
CGS	**c**entimeter **g**ram **s**econd (system of unit)	15
CHM	**c**onstant **h**eight **m**ode	8
CPC	**c**ompound **p**arabolic **c**oncentrator	30
cw	**c**ontinous **w**ave (laser)	47
DFB	**d**istributed **f**eed**b**ack	15
DNA	**d**eoxyribo**n**uclein **a**cid	5
DSP	**d**igital **s**ignal **p**rocessing	59
EFM	**e**lectric **f**orce **m**icroscope	4
EM	**e**lectron **m**icroscope	4
ETH	Swiss Federal Institute of Technology (**E**idgenössische **T**echnische **H**ochschule)	32
F	**f**ace–centered (unit cell: additional point in the center of each face)	19
fcc	**f**ace–**c**entered **c**ubic	19
FFT	**f**ast **F**ourier **t**ransform	36
FMM	**f**orce **m**odulation **m**icroscope	4
FDTD	**f**inite–**d**ifference **t**ime–**d**omain	25
FTIR	**f**rustrated **t**otal **i**nternal **r**eflection	5
FPA	**f**ocal **p**lane **a**rray	60
FWHM	**f**ull–**w**idth at **h**alf–**m**aximum	23
hcp	**h**exagonal **c**lose–**p**acked	19
I	**i** (unit cell, body–centered: additional point in the center)	19
IBE	**i**on **b**eam **e**tching	45
IC	**i**ntegrated **c**ircuit	1
ICP	**i**nductively **c**oupled **p**lasma (etching)	33
IR	**i**nfra**r**ed	46
MFM	**m**agnetic **f**orce **m**icroscope	4

continued on next page ...

. . . continued from previous page

Abbreviation	Description	Page
MOCVD	**m**etal **o**rganic **c**hemical **v**apor **d**eposition	32
MQW	**m**ultiple **q**uantum **w**ell	59
MTF	**m**odulation **t**ransfer **f**unction[1]	10
NA	**n**umerical **a**perture	11
NFO	**n**ear–**f**ield **o**ptics	5
NIR	**n**ear–**i**nfra**r**ed	33
NSOM	**s**canning **n**ear–**f**ield **o**ptical **m**icroscope	1
NTSC	**n**ational **t**elevision **s**ystem **c**ommittee (TV format)	60
P	**p**rimitive (unit cell, simple)	19
PAL	**p**hase **a**lternation **l**ine (European TV format)	60
PBG	**p**hotonic **b**and **g**ap	14
PCF	**p**hotonic **c**rystal **f**iber	22
PEC	**p**roximity–**e**ffect **c**orrection	33
PECVD	**p**lasma–**e**nhanced **c**hemical **v**apor **d**eposition	33
PHC	**ph**otonic **c**rystal	1
PID	**P**roportional–**D**erivative–**I**ntegral	6
pixel	**pic**ture **el**ement	60
PMMA	**p**oly**m**ethyl**m**eth**a**crylate (resist)	33
pt	**p**ulling **t**ime	28
PTM	**p**hoton **t**unnelling **m**icroscope	5
PSTM	**p**hoton **s**canning **t**unnelling **m**icroscope	5
R	**r**hombohedral (unit cell: hexagonal class only)	19
RIE	**r**eactive **i**on **e**tching	33
sc	**s**imple **c**ubic	19
SEM	**s**canning **e**lectron **m**icroscope	4
SHG	**s**econd-**h**armonic **g**eneration	31
SLD	**s**ingle **l**ine **d**efect	23
SMF	**s**ingle **m**ode **f**iber	27
SNR	**s**ignal–to–**n**oise **r**atio	36
SNOM	**s**canning **n**ear–**f**ield **o**ptical **m**icroscope	5
SPM	**s**canning **p**robe **m**icroscope	4
STEM	**s**canning **t**ransmission **e**lectron **m**icroscope	4
STM	**s**canning **t**unnelling **m**icroscope	5
TE	**t**ransverse **e**lectric (s-polarized wave[2])	22
TEM	**t**ransmission **e**lectron **m**icroscope	4
TIR	**t**otal **i**nternal **r**eflection	22
TM	**t**ransverse **m**agnetic (p-polarized wave[2])	22
TV	**t**ele**v**ision	68
VCSEL	**v**ertical **c**avity **s**urface **e**mitting **l**asers	31
WGM	**w**hispering–**g**allery **m**odes	31
WP	**w**ave**p**late	61

Table F.1: List of abbreviations

---

[1] A mathematical function that expresses the ability of an optical or electronic device to transfer signals faithfully as a function of the spatial or temporal frequency of the signal. The MTF is the ratio of percentage modulation of a sinusoidal signal leaving to that entering the device over the range of frequencies of interest. For square wave signals also known as CTF [187].

[2] With respect to the plane of incidence.

List of Figures

List of Tables

Bibliography

[1] M. A. Paesler and P. J. Moyer, *Near–Field Optics: Theory, Instrumentation and Applications.* New York: John Wiley & Sons, Inc., 1996.

[2] H. Belyus, "Die Geschichte der Brille (The history of spectacles)," http://www.optiker.at/archiv/brillengeschichte/brilleng.htm, June 2000.

[3] J. Kramer, "Oldest Optical Device ? The Nimrud Lens," available from: http://bpccs.com/lcas/Articles/nimrud.htm, August 2002, ref: BBC News Science Editor Dr. David Whitehouse.

[4] D. W. Pohl, in *Advances in Optical and Electron Microscopy*, C. J. R. Sheppard and T. Mulvey, Eds. Academic Press, 1991, pp. 243–312.

[5] E. Abbé, "Beiträge zur Theorie der Mikroskope und der mikroskopischen Wahrnehmung," *Archiv für Mikroskopische Anatomie*, vol. **9**, p. 413, 1873.

[6] V. Sandoghdar, "Trends and developments in scanning near–field optical microscopy," in *Nanometer Scale Science and Technology*, ser. Proceedings of the International School of Physics "Enrico Fermi" Course CXLIV, M. Allegrini, N. Garcia, and O. Marti, Eds., vol. **144**. Amsterdam: IOS Press, 2001, pp. 65–119.

[7] D. W. Pohl, "Near–field optics and the surface plasmon polariton," in *Near–Field Optics and Surface Plasmon Polaritons*, S. Kawata, Ed. Springer Verlag, 2001, pp. 1–13.

[8] S. Kawata, K. Tanaka, and N. Takahashi, *Nano–Optics.* Berlin: Springer–Verlag, 2002, ch. 2 Electromagnetism Theory and Analysis for Near–Field Nano–Optics, pp. 35–59.

[9] M. Labardi, P. G. Gucciardi, and M. Allegrini, "Near–field optical microscopy," *Rivista del Nuovo Cimento*, vol. **23**, no. 4, pp. 1–35, 2000.

[10] J. W. P. Hsu, "Near–field scanning optical microscopy studies of electronic and photonic materials and devices," *Materials Science and Engineering: R: Reports*, vol. **33**, no. 1, pp. 1–50, 2001.

[11] J. J. Greffet and R. Carminati, "Image formation in near–field optics," *Progress in Surface Science*, vol. **56**, no. 3, pp. 133–237, 1997.

[12] *piezoline*, piezosystem jena GmbH, DE–07745 Jena, 1995,
available from: http://www.piezojena.com/img_db/dl_mg_1040388237.pdf.

[13] G. Binnig and H. Rohrer, "Scanning tunnelling microscopy," *Helvetica Physica Acta*, vol. **55**, pp. 726–735, 1982.

[14] G. Binnig, H. Rohrer, C. Gerber, and E. Weibel, "Surface studies by scanning tunneling microscopy," *Physical Review Letters*, vol. **49**, no. 1, pp. 57–61, 1982.

[15] G. Binnig, C. F. Quate, and C. Gerber, "Atomic force microscope," *Physical Review Letters*, vol. **56**, pp. 930–933, 1986.

[16] J. K. Gimzewski and C. Joachim, "Nanoscale science of single molecules using local probes," *Science*, vol. **283**, no. 5408, pp. 1683–1688, 1999.

[17] J. A. Stroscio and D. M. Eigler, “Atomic and molecular manipulation with the scanning tunneling microscope,” *Science*, vol. **254**, no. 5036, pp. 1319–1326, 1991.

[18] D. W. Pohl, W. Denk, and M. Lanz, “Optical stethoscopy: Image recording with resolution $\lambda/20$,” *Applied Physics Letters*, vol. **44**, no. 7, pp. 651–653, 1984.

[19] A. Lewis, M. Isaacson, A. Muray, and A. Harootunian, “Scanning optical spectral microscopy with 500 Å spatial–resolution,” *Biophysical Journal*, vol. **41**, p. A405, 1983.

[20] A. Lewis, M. Isaacson, A. Harootunian, and Muray, “Development of a 500 Å spatial resolution light microscope: I. light is efficiently transmitted through $\lambda/16$ diameter apertures,” *Ultramicroscopy*, vol. **13**, no. 3, pp. 227–231, 1984.

[21] D. McMullan, “Scanned optical microscopes,” in *The prehistory of scanned image microscopy*, ser. Proceedings of the Royal Microscopical Society, vol. **25**, 1990, pp. 127–131.

[22] E. H. Synge, “A suggested method for extending the microscopic resolution into the ultramicroscopic region,” *Phil. Mag.*, vol. **6**, pp. 356–362, 1928.

[23] ——, “An application of piezoelectricity to microscopy,” *Phil. Mag.*, vol. **13**, pp. 297–300, 1932.

[24] E. A. Ash and G. Nicholls, “Super–resolution aperture scanning microscope,” *Nature*, vol. **237**, no. 5357, pp. 510–513, 1972.

[25] E. J. Ambrose, “Surface contact microscope for the study of cell movements,” *Nature*, vol. **178**, no. 4543, p. 1194, 1956.

[26] C. W. McCutchen, “Optical systems for observing surface topography by frustrated total internal reflection + by interference,” *Review of Scientific Instruments*, vol. **35**, no. 10, pp. 1340–1345, 1964.

[27] J. M. Guerra, M. Srinivasarao, and R. S. Stein, “Photon tunneling microscopy of polymeric surfaces,” *Science*, vol. **262**, pp. 1395–1400, 1993.

[28] J. M. Guerra, “Photon tunneling microscopy,” *Applied Optics*, vol. **29**, no. 26, pp. 3741–3752, 1990.

[29] R. C. Reddick, R. J. Warmack, and T. L. Ferrell, “New form of scanning optical microscopy,” *Physical Review B*, vol. **39**, no. 1, pp. 767–770, 1989.

[30] D. Courjon, K. Sarayeddine, and M. Spajer, “Scanning tunneling optical microscopy,” *Optics Communications*, vol. **71**, pp. 23–28, 1989.

[31] R. Toledo-Crow, P. C. Yang, Y. Chen, and M. Vaez-Iravani, “Near–field differential scanning optical microscope with atomic force regulation,” *Applied Physics Letters*, vol. **60**, no. 24, pp. 2957–2959, 1992.

[32] E. Betzig, P. L. Finn, and J. S. Weiner, “Combined shear force and near–field scanning optical microscopy,” *Applied Physics Letters*, vol. **60**, no. 20, pp. 2484–2486, 1992.

[33] E. Betzig and R. J. Chichester, “Single molecules observed by near-field scanning optical microscopy,” *Science*, vol. **262**, pp. 1422–1425, 1993.

[34] P. G. Gucciardi, M. Labardi, S. Gennai, F. Lazzeri, and M. Allegrini, “Versatile scanning near–field optical microscope for material science applications,” *Review of Scientific Instruments*, vol. **68**, no. 8, pp. 3088–3092, 1997.

[35] U. Dürig, H. R. Steinauer, and N. Blanc, “Dynamic force microscopy by means of the phase–controlled oscillator method,” *Journal of Applied Physics*, vol. **82**, pp. 3641–3651, 1997.

[36] A. G. T. Ruiter, J. A. Veerman, K. O. van der Werf, and N. F. van Hulst, "Dynamic behavior of tuning fork shear–force feedback," *Applied Physics Letters*, vol. **71**, no. 1, pp. 28–30, 1997.

[37] J. Maps, "Atomic force microscopy of thermal insulation materials with aerogels, summary of research," http://www.jmaps.d.umn.edu/research/afm–nasa/report–col.pdf, July 2002, ref. [6] of this document should be Franz J. Giessibl, Applied Physics Letters **73**(1998)3956–3958.

[38] R. D. Grober, J. Acimovic, J. Schuck, D. Hessman, P. J. Kindlemann, J. Hespanha, A. S. Morse, K. Karrai, I. Tiemann, and S. Manus, "Fundamental limits to force detection using quartz tuning forks," *Review of Scientific Instruments*, vol. **71**, no. 7, pp. 2776–2780, 2000.

[39] B. Hecht, H. Heinzelmann, and D. W. Pohl, "Combined aperture SNOM/PSTM: best of both worlds?" *Ultramicroscopy*, vol. **57**, pp. 228–234, 1995.

[40] V. Sandoghdar, B. Buchler, P. Kramper, S. Götzinger, O. Benson, and M. Kafesaki, *Photonic Crystals — Advances in Design, Fabrication and Characterization.* Berlin: Wiley–VCH Verlag, 2004, ch. 11 Scanning near–field optical studies of photonic devices, pp. 215–237.

[41] K. Iizuka, *Elements of Photonics: In Free Space and Special Media*, 1st ed. New York: John Wiley & Sons, 2001, vol. **1**.

[42] G. A. Massey, "Microscopy and pattern generation with scanned evanescent waves," *Applied Optics*, vol. **23**, no. 5, pp. 658–660, 1984.

[43] J. M. Vigoureux, F. Depasse, and C. Girard, "Superresolution of near–field optical microscopy defined from properties of confined electromagnetic waves," *Applied Optics*, vol. **31**, no. 16, pp. 3036–3045, 1992.

[44] J. M. Vigoureux and D. Courjon, "Detection of nonradiative fields in light of the heisenberg uncertainty principle and the rayleigh criterion," *Applied Optics*, vol. **31**, no. 16, pp. 3170–3177, 1992.

[45] S. Wegscheider, "Optische Strukturierung von Oberflächen ohne Beugungsbeschränkung," Ph.D. dissertation, University of Constance, Germany, 1998.

[46] C. Hettich, 2003, private communication.

[47] K. Karrai and R. D. Grober, "Piezoelectric tip-sample distance control for near field optical microscopes," *Applied Physics Letters*, vol. **66**, no. 14, pp. 1842–1844, 1995.

[48] E. Hecht, *Optics*, 4th ed. Reading: Pearson Addison–Wesley, 2001.

[49] M. Born and E. Wolf, *Principles of Optics: Electromagnetic Theory of Propagation, Interference and Diffraction of Light*, 6th ed. New York: Pergamon Press Inc., 1993.

[50] H. Volkmann, "Ernst Abbe and his work," *Applied Optics*, vol. **5**, no. 11, pp. 1720–1731, 1966.

[51] J. Bardeen and W. H. Brattain, "The transistor, a semi–conductor triode," *Physical Review*, vol. **74**, no. 2, pp. 230–231, 1948.

[52] J. D. Joannopoulos, R. D. Meade, and J. N. Winn, *Photonic Crystals.* Princeton: Princeton University Press, 1995.

[53] S. E. Mann, I. N. Miaoulis, and P. Y. Wong, "Spectral imaging, reflectivity measurements, and modeling of iridescent butterfly scale structures," *Optical Engineering*, vol. **40**, no. 10, pp. 2061–2068, 2001.

[54] U. Grüning, V. Lehmann, and U. Eberl, "Photonische Bandstruktur in Schmetterlingsflügeln," *Physikalische Blätter*, no. 7, p. 664, 1996.

[55] H. Ghiradella, “Light and color on the wing: structural colors in butterflies and moths,” *Applied Optics*, vol. **30**, no. 24, pp. 3492–3500, 1991.

[56] A. Sweeney, C. Jiggins, and S. Johnson, “Polarized light as butterfly mating material,” *Nature*, vol. **423**, pp. 31–23, 2003.

[57] L. P. Biró, Z. Bálint, K. Kertész, Z. Vértesy, G. I. Márk, Z. E. Horváth, J. Balázs, D. Méhn, I. Kiricsi, V. Lousse, and J.-P. Vigneron, “Role of photonic–crystal–type structures in the thermal regulation of a lycaenid butterfly sister species pair,” *Physical Review E*, vol. **67**, pp. 21 907(1–7), 2003.

[58] V. P. Bykov, “Spontaneous emission in a periodic structure,” *Sov. Phys. JETP*, vol. **35**, pp. 269–273, 1972.

[59] E. Yablonovitch, T. J. Gmitter, and R. Bhat, “Inhibited and enhanced spontaneous emission from optically thin AlGaAs/GaAs double heterostructures,” *Physical Review Letters*, vol. **61**, no. 22, pp. 2546–2549, 1988.

[60] S. John, “Strong localization of photons in certain disordered dielectric superlattices,” *Physical Review Letters*, vol. **58**, no. 23, pp. 2486–2489, 1987.

[61] C. Kittel, *Introduction to Solid State Physics*, 7th ed. New York: John Wiley & Sons, 1996.

[62] N. W. Ashcroft and N. D. Mermin, *Solid State Physics*, 1st ed. Fort Worth: Saunders College, 1976.

[63] A. F. Koenderink, “Emission and transport of light in photonic crystals,” Ph.D. dissertation, University of Twente, The Netherlands, 2003, available from: http://www.tn.utwente.nl/cops/pdf/theses/koenderink.pdf.

[64] S. Noda and T. Baba, *Roadmap on Photonic Crystals.* Boston: Kluwer Academic Publishers, 2003, ch. 1 Physical and Experimental Background of Photonic Crystals, pp. 1–12.

[65] M. Lončar, A. Scherer, and Y. Qui, “Nanocavity lasers detect chemicals,” *Laser Focus World*, vol. **39**, no. 5, pp. 89–91, 2003.

[66] M. Woldeyohannes and S. John, “Coherent control of spontaneous emission near a photonic band edge,” *Journal of Optics B: Quantum and semiclassical Optics*, vol. **5**, pp. R43–R82, 2003.

[67] F. K. Kneubühl and M. W. Sigrist, *Laser*, 5th ed. Stuttgart: Teubner, 1999.

[68] A. Yariv and P. Yeh, *Optical Waves in Crystals : Propagation and Control of Laser Radiation.* New York: John Wiley & Sons, 1983.

[69] Z.-Y. Li, X. Zhang, and Z.-Q. Zhang, “Disordered photonic crystals understood by a perturbation formalism,” *Physical Review B*, vol. **61**, no. 23, pp. 15 738–15 748, 2000.

[70] J. D. Jackson, *Classical Electrodynamics*, 3rd ed. New York: John Wiley & Sons, Inc., 1998.

[71] N. Bloembergen, *Nonlinear Optics*, 4th ed. Singapore: World Scientific Pub Co., 1996.

[72] P. W. Atkins, *Physical Chemistry*, 7th ed. W H Freeman & Co., 2001.

[73] L. P. Bouckaert, R. Smoluchowski, and E. Wigner, “Theory of Brillouin zones and symmetry properties of wave functions in crystals,” *Physical Review*, vol. **50**, pp. 58–67, 1936.

[74] F. Bloch, “Über die Quantenmechanik der Elektronen in Kristallgittern,” *Zeitschrift für Physik*, vol. **52**, pp. 555–600, 1929.

[75] G. Floquet, “Sur les équations différentielles linéaries à coefficients périodiques,” *Ann. École Norm. Sup.*, vol. **12**, pp. 47–88, 1883.

[76] A. Birner, "Optische Wellenleiter und Mikroresonatoren in zweidimensionalen photonischen Kristallen aus makroporösem Silizium," Ph.D. dissertation, Martin–Luther–University Halle–Wittenberg, Germany, 2000, available from: http://sundoc.bibliothek.uni-halle.de/diss–online/00/00H127/prom.pdf.

[77] R. D. Meade, A. M. Rappe, K. D. Brommer, J. D. Joannopoulos, and O. L. Alerhand, "Accurate theoretical analysis of photonic band–gap materials," *Physical Review B*, vol. **48**, no. 11, pp. 8434–8437, 1993.

[78] ——, "Erratum: Accurate theoretical analysis of photonic band–gap materials," *Physical Review B*, vol. **55**, no. 23, p. 15942, 1997.

[79] K. M. Ho, C. T. Chan, and C. M. Soukoulis, "Existence of a photonic gap in periodic dielectric structures," *Physical Review Letters*, vol. **65**, no. 25, pp. 3152–3155, 1990.

[80] H. S. Sözüer and J. W. Haus, "Photonic bands: Convergence problems with the plane–wave method," *Physical Review B*, vol. **45**, no. 24, pp. 13 962–13 972, 1992.

[81] R. D. Meade, O. L. Alerhand, and J. D. Joannopoulos, *Handbook of Photonic Band Gap Materials*. JAMteX I.T.R., 1993.

[82] K. Iizuka, E. of Photonics: For Fiber and I. Optics, Eds. New York: John Wiley & Sons, 2001, vol. **2**.

[83] S. I. Bozhevolnyi, V. S. Volkov, T. Søndergaard, A. Boltasseva, P. I. Borel, and M. Kristensen, "Near–field imaging of light propagation in photonic crystal waveguides: Explicit role of Bloch harmonics," *Physical Review B*, vol. **66**, pp. 235 204(1–9), 2002.

[84] M. Lončar, D. Nedeljković, T. P. Pearsall, J. Vukčović, A. Scherer, S. Kuchinsky, and D. C. Allan, "Experimental and theoretical confirmation of Bloch–mode light propagation in planar photonic crystal waveguides," *Applied Physics Letters*, vol. **80**, no. 10, pp. 1689–1691, 2002.

[85] Y. Pochi, A. Yariv, and E. Marom, "Theory of bragg fiber," *Journal Of The Optical Society Of America*, vol. **68**, no. 9, pp. 1196–1201, 1978.

[86] T. A. Birks, P. J. Roberts, P. S. J. Russel, D. M. Atkin, and T. J. Shepherd, "Full 2D photonic bandgaps in silica/air structures," *Electronics Letters*, vol. **31**, no. 22, pp. 1941–1943, 1995.

[87] T. Hasegawa, *Roadmap on Photonic Crystals*. Boston: Kluwer Academic Publishers, 2003, ch. 3.11 Photonic Crystal Fibers, pp. 129–137.

[88] S. Noda and T. Baba, Eds., *Roadmap on Photonic Crystals*. Boston: Kluwer Academic Publishers, 2003, ch. 5.6 Examples of variuos Photonic Crystal Applications: Fibers, pp. 212–216.

[89] T. Baba, *Roadmap on Photonic Crystals*. Boston: Kluwer Academic Publishers, 2003, ch. 3.3 2D Photonic Crystal made of Semiconductors: General Features, pp. 50–65.

[90] E. Yablonovitch, T. J. Gmitter, and K. M. Leung, "Photonic band structure: The face-centered–cubic case employing nonspherical atoms," *Physical Review Letters*, vol. **67**, no. 17, pp. 2295–2298, 1991.

[91] K. M. Ho, C. T. Chan, and C. M. Soukoulis, "Existence of a photonic gap in periodic dielectric structures," *Physical Review Letters*, vol. **65**, no. 25, pp. 3152–3155, 1990.

[92] S. Noda and T. Baba, *Roadmap on Photonic Crystals*. Boston: Kluwer Academic Publishers, 2003, ch. 3.2 The Present Status of Photonic Crystal Development: Summary of Structures and Researches, pp. 46–49.

[93] V. Kuzmiak and A. A. Maradudin, "Localized defect modes in a two–dimensional triangular photonic crystal," *Physical Review B*, vol. **57**, no. 24, pp. 15 242–15 250, 1998.

[94] ——, “Erratum: Localized defect modes in a two–dimensional triangular photonic crystal,” *Physical Review B*, vol. **59**, no. 19, p. 12693, 1999.

[95] A. Yariv, *Optical electronics*, 3rd ed. New York: Holt, Rinehart and Winston, 1985.

[96] B. E. A. Saleh and M. C. Teich, *Fundamentals of Photonics*, 2nd ed. New York: John Wiley & Sons, 1991.

[97] S. Fan, J. N. Winn, A. Devenyi, J. C. Chen, R. D. Meade, and J. D. Joannopoulos, “Guided and defect modes in periodic dielectric waveguides,” *Journal Of The Optical Society Of America B*, vol. **12**, no. 7, pp. 1267–1272, 1995.

[98] M. Notomi, K. Yamada, A. Shinya, J. Takahashi, C. Takahashi, and I. Yokohama, “Extremely large group–velocity dispersion of line–defect waveguides in photonic crystal slabs,” *Physical Review Letters*, vol. **87**, no. 25, pp. 253 902(1–4), 2001.

[99] A. R. McGurn, “Photonic crystal circuits: A theory for two– and three–dimensional networks,” *Physical Review B*, vol. **61**, no. 19, pp. 13 235–13 249, 2000.

[100] ——, “Photonic crystal circuits: Localized modes and waveguide couplers,” *Physical Review B*, vol. **65**, no. 7, pp. 75 406(1–11), 2002.

[101] S. Noda and T. Baba, Eds., *Roadmap on Photonic Crystals.* Boston: Kluwer Academic Publishers, 2003, ch. 5.4 Examples of variuos Photonic Crystal Applications: Resonators and Filters, pp. 187–192.

[102] ——, *Roadmap on Photonic Crystals.* Boston: Kluwer Academic Publishers, 2003, ch. 5.5 Examples of variuos Photonic Crystal Applications: Waveguides, pp. 192–212.

[103] S. Noda and T. Baba, *Roadmap on Photonic Crystals.* Boston: Kluwer Academic Publishers, 2003, ch. 6 Technology Roadmap on Photonic Crystal, pp. 243–249.

[104] M. Agio and C. M. Soukoulis, “Ministop bands in single–defect photonic crystal waveguides,” *Physical Review E*, vol. **64**, no. 5, pp. 55 603(1–4), 2001.

[105] K. S. Yee, “Numerical solution of initial boundary value problems involving maxwell’s equations in isotropic media,” *IEEE Transactions on Antennas and Propagation*, vol. **AP–14**, no. 3, pp. 302–307, 1966.

[106] A. Taflove, *Computational Electrodynamics: The Finite–Difference Time–Domain Method.* Boston: Artech House, 1995.

[107] Z. P. Liao, H. L. Wong, B. P. Yang, and Y. F. Yuan, “A transmitting boundary for transient wave analysis,” *Scientia Sinica A*, vol. **27**, no. 10, pp. 1063–1076, 1984.

[108] M. Agio, E. Lidorikis, and C. M. Soukoulis, “Impurity modes in a photonic crystal: Coupling efficiency and Q factor,” *Journal Of The Optical Society Of America B*, vol. **17**, no. 12, pp. 2037–2042, 2000.

[109] M. Qiu and S. He, “Numerical method for computing defect modes in two–dimensional photonic crystals with dielectric or metallic inclusions,” *Physical Review B*, vol. **61**, no. 19, pp. 12 871–12 876, 2000.

[110] P. Kramper, “Mikroskopie und Spektroskopie an photonischen Kristallen: Einschluss von Licht auf Subwellenlängen-Bereiche,” Ph.D. dissertation, University of Constance, Germany, 2002, available from: http://www.ub.uni–konstanz.de/kops/volltexte/2003/943/.

[111] *Operation Manual P–2000 Micropipette Puller*, Novato, U.S.A., rev. 2.0/111199.

[112] M. Vorwerk, “Einzelmoleküldetektion mit dem optischen Nahfeldmikroskop,” Master’s thesis, University of Constance, Germany, 1996.

[113] G. A. Valaskovic, M. Holton, and G. H. Morrison, "Parameter control, characterization, and optimization in the fabrication of optical fiber near–field probes," *Applied Optics*, vol. **34**, no. 7, pp. 1215–1228, 1995.

[114] H. A. Bethe, "Theory of diffraction by small holes," *The Physical Review, Second Series*, vol. **66**, no. 7, pp. 163–182, 1944, available from: http://www.its.caltech.edu/~mankei/ee150sp03/Bethe_diffraction_small_hole_PR_1944.pdf.

[115] C. J. Bouwkamp, "Diffraction theory," *Reports on progress in physics*, vol. **17**, no. 1, pp. 35–100, 1954, available from: http://www.its.caltech.edu/~mankei/ee150sp03/~ ~Bouwkamp_diffraction_theory_Rep_Phys_1954.pdf.

[116] ——, "On bethe's theory of diffraction by small holes," *Philips Research Reports*, vol. **5**, no. 5, pp. 321–332, 1950, available from: http://www.its.caltech.edu/~mankei/ee150sp03/Bouwkamp_on_Bethe_Philips_1954.pdf.

[117] L. Novotny and D. W. Pohl, "Light propagation in scanning near–field optical microscopy," in *Photons and local probes*, ser. NATO ASI series. Series E, Applied sciences, O. Marti and R. Möller, Eds., vol. **300**. Dordrecht: Kluwer Academic Publishers, 1995, pp. 21–33, Proceedings of the NATO Advanced Research Workshop on Photons and Local Probes, Reichenau, Germany, September 11-17, 1994.

[118] B. I. Yakobson and M. A. Paesler, "Kinetics, morphology and pulling regimes for sensing tips in near–field microscopy," *Ultramicroscopy*, vol. **57**, pp. 241–245, 1995.

[119] S. Madsen, N. C. R. Holme, P. S. Ramanujam, S. Hvilsted, J. M. Hvam, and S. J. Smith, "Optimizing the fabrication of aluminum–coated fiber probes and their application to optical near–field lithography," *Ultramicroscopy*, vol. **71**, pp. 65–71, 1998.

[120] F. J. Giessibl, S. Hembacher, M. Herz, J. Mannhart, and C. Schiller, "Rastersondenmikroskopie," http://www.physik.uni–augsburg.de/exp6/research/sxm/sxm_d.shtml, November 2003.

[121] K. Karrai and I. Tiemann, "Interfacial shear force microscopy," *Physical Review B*, vol. **62**, no. 19, pp. 13 174–13 181, 2000.

[122] A. G. T. Ruiter, "Near–field optical microscopy: Towards the molecular scale," Ph.D. dissertation, University of Twente, The Netherlands, 1997, available from: http://www.ub.utwente.nl/webdocs/tn/1/t0000001.pdf.

[123] C. S. Fokas, "Untersuchung heterogen katalysierter Reaktionen mittels Scanning Near Field Optical Microscopy," Ph.D. dissertation, Eidgenössische Technische Hochschule Zürich, Switzerland, 2002, available from: http://e–collection.ethbib.ethz.ch/show?type=diss&nr=14740.

[124] T. Kalkbrenner, 2003, private communication.

[125] T. L. Cloninger, S. Balasubramaniam, B. D. Boudreau, J. Raja, and R. J. Hocken, "A simple technique for screening near–field probes," *Ultramicroscopy*, vol. **57**, pp. 223–227, 1995.

[126] M. A. Bopp, "Optische Nahfeldmikroskopie an evaneszenten Wellen und einzelnen Farbstoffmolekülen," Ph.D. dissertation, University of Basel, Switzerland, 1996.

[127] B. I. Yakobson and M. A. Paesler, "Tip optics for illumination nsom: extended–zone approach," *Ultramicroscopy*, vol. **57**, pp. 204–207, 1995.

[128] H. Hinterberger and R. Winston, "Efficient light coupler for threshold cerenkov counters," *Review Of Scientific Instruments*, vol. **37**, no. 8, pp. 1094–1095, 1966.

[129] V. K. Baranov, Russian certificate of authorship 167327, 1967.

[130] R. Levisetti, D. Park, and R. Winston, “Corneal cones of limulus as optimized light concentrators,” *Nature*, vol. **253**, no. 5487, pp. 115–116, 1975.

[131] T. Yatsui and M. Ohtsu, “High–throughput probes for near–field optics and their applications,” in *Progress in Nano–Electro–Optics* **I**: *Basics and Theory of Near–Field Optics*, M. Ohtsu, Ed. Springer Verlag, 2003, pp. 1–28.

[132] A. G. Choo, H. E. Jackson, U. Thiel, G. N. De Brabander, and J. T. Boyd, “Near field measurements of optical channel waveguides and directional couplers,” *Applied Physics Letters*, vol. **65**, no. 8, pp. 947–949, 1994.

[133] B. C. Buchler, P. Kramper, M. Kafesaki, C. M. Soukoulis, and V. Sandoghdar, “Near–field optical investigations of photonic crystal microresonators,” 2004, to appear in IEICE Transactions.

[134] J. C. Knight, N. Dubreuil, V. Sandoghdar, J. Hare, V. Lefèvre-Seguin, J. M. Raimond, and S. Haroche, “Characterizing whispering–gallery modes in microspheres by direct observation of the optical standing–wave pattern in the near field,” *Optics Letters*, vol. **21**, no. 10, pp. 698–700, 1996.

[135] Knight, J. C. and Dubreuil, N. and Sandoghdar, V. and Hare, J. and Lefèvre–Seguin, V. and Raimond, J. M. and Haroche, S., “Mapping whispering–gallery modes in microspheres with a near–field probe,” *Optics Letters*, vol. **20**, no. 14, pp. 1515–1517, 1995.

[136] S. Bourzeix, J. M. Moison, F. Mignard, F. Barthe, A. C. Boccara, C. Licoppe, B. Mersali, M. Allovon, and A. Bruno, “Near–field optical imaging of light propagation in semiconductor waveguide structures,” *Applied Physics Letters*, vol. **73**, no. 8, pp. 1035–1037, 1998.

[137] M. L. M. Balistreri, J. P. Korterik, L. Kuipers, and N. F. van Hulst, “Local observations of phase singularities in optical fields in waveguide structures,” *Physical Review Letters*, vol. **85**, no. 2, pp. 294–297, 2000.

[138] M. L. M. Balistreri, H. Gersen, J. P. Korterik, L. Kuipers, and N. F. van Hulst, “Tracking femtosecond laser pulses in space and time,” *Science*, vol. **294**, no. 5544, pp. 1080–1082, 2000.

[139] C. Lienau, A. Richter, A. Klehr, and T. Elsaesser, “Near–field scanning optical microscopy of polarization bistable laser diodes,” *Applied Physics Letters*, vol. **69**, pp. 2471–2473, 1996.

[140] I. Hörsch, R. Kusche, O. Marti, B. Weigl, and K. J. Ebeling, “Spectrally resolved near–field mode imaging of vertical cavity semiconductor lasers,” *Journal of Applied Physics*, vol. **79**, pp. 3831–3834, 1996.

[141] M. L. M. Balistreri, J. W. Klunder, F. C. Blom, A. Driessen, H. W. J. M. Hoekstra, J. P. Korterik, L. Kuipers, and N. F. van Hulst, *Optics Letters*, vol. **24**, no. 24, pp. 1829–1831, 1999.

[142] G. H. Vander-Rhodes, B. B. Goldberg, M. S. Ünlü, S.-T. Chu, and B. E. Little, “Internal spatial modes in glass microring resonators,” *IEEE Journal of Selected Topics in Quantum Electronics*, vol. **6**, pp. 46–53, 2000.

[143] J. D. Mills, C. W. J. Hillman, W. S. Brocklesby, and B. H. Blott, “Evanescent field imaging of an optical fiber bragg grating,” *Applied Physics Letters*, vol. **75**, no. 26, pp. 4058–4060, 1999.

[144] E. B. McDaniel, J. W. P. Hsu, L. S. Goldner, R. J. Tonucci, E. L. Shirley, and G. W. Bryant, “Local characterization of transmission properties of a two–dimensional photonic crystal,” *Physical Review B*, vol. **55**, no. 16, pp. 10 878–10 882, 1997.

[145] G. W. Bryant, E. L. Shirley, L. S. Goldner, E. B. McDaniel, J. W. P. Hsu, and R. J. Tonucci, "Theory of probing a photonic crystal with transmission near–field optical microscopy," *Physical Review B*, vol. **58**, no. 4, pp. 2131–2141, 1998.

[146] E. Flück, N. F. van Hulst, W. L. Vos, and L. Kuipers, "Near–field optical investigation of three–dimensional photonic crystals," *Physical Review E*, vol. **68**, pp. 15 601(R)1–4, 2003.

[147] G. H. Vander-Rhodes, M. S. Ünlü, B. B. Goldberg, J. M. Pomeroy, and T. F. Krauss, "Characterisation of waveguide microcavities using high–resolution transmission spectroscopy and near–field scanning optical microscopy," *IEE Proceedings–Optoelectronics*, vol. **145**, no. 6, pp. 379–383, 1998.

[148] P. L. Phillips, J. C. Knight, B. J. Mangan, P. S. J. Russell, M. D. B. Charlton, and G. J. Parker, "Near–field optical microscopy of thin photonic crystal films," *Journal of Applied Physics*, vol. **85**, no. 9, pp. 6337–6342, 1999.

[149] A. L. Campillo, J. W. P. Hsu, C. A. White, and A. Rosenberg, "Mapping the optical intensity distribution in photonic crystals using a near–field scanning optical microscope," *Journal of Applied Physics*, vol. **89**, no. 5, pp. 2801–2807, 2001.

[150] D. R. Smith, R. Dalichaouch, N. Kroll, S. Schultz, S. L. McCall, and P. P. M., "Photonic band structure and defects in one and two dimensions," *Journal of the Optical Society of America B*, vol. **10**, no. 2, pp. 314–321, 1993.

[151] S. I. Bozhevolnyi, V. S. Volkov, J. Arentoft, A. Boltasseva, T. Søndergaard, and M. Kristensen, "Direct mapping of light propagation in photonic crystal waveguides," *Optics Communications*, vol. **212**, pp. 51–55, 2002.

[152] P. Kramper, A. Birner, M. Agio, C. M. Soukoulis, F. Müller, U. Gösele, J. Mlynek, and V. Sandoghdar, "Direct spectroscopy of a deep two–dimensional photonic crystal microresonator," *Physical Review B*, vol. **64**, pp. 33 102(1–4), 2001.

[153] P. Kramper, M. Kafesaki, C. M. Soukoulis, A. Birner, F. Müller, R. Wehrspohn, U. Gösele, J. Mlynek, and V. Sandoghdar, "Near–field visualization of light confinement in a photonic crystal microresonator," *Optics Letters*, vol. **29**, no. 2, pp. 174–176, 2004.

[154] D. Gérard, L. Berguiga, F. de Fornel, L. Salomon, C. Seassal, X. Letartre, P. Rojo-Romeo, and P. Viktorovitch, "Near–field probing of active photonic–crystal structures," *Optics Letters*, vol. **27**, no. 3, pp. 173–175, 2001.

[155] D.-J. Shin, S.-H. Kim, J.-K. Hwang, H.-Y. Ryu, H.-G. Park, D.-S. Song, and Y.-H. Lee, "Far– and near–field investigations on the lasing modes in two–dimensional photonic crystal slab lasers," *IEEE Journal of Quantum Electronics*, vol. **38**, no. 7, pp. 857–866, 2002.

[156] K. Okamoto, M. Lončar, T. Yoshie, A. Scherer, Y. Qiu, and P. Gogna, "Near-field scanning optical microscopy of photonic crystal nanocavities," *Applied Physics Letters*, vol. **82**, no. 11, pp. 1676–1678, 2003.

[157] S. Götzinger, S. Demmerer, O. Benson, and V. Sandoghdar, "Mapping and manipulating whispering gallery modes of a microsphere resonator with a near–field probe," *Journal of Microscopy*, vol. **202**, no. 1, pp. 117–121, 2001.

[158] M. Vaez-Iravani and R. Toledo-Crow, "Phase contrast and amplitude pseudoheterodyne interference near field scanning optical microscopy," *Applied Physics Letters*, vol. **62**, no. 10, pp. 1044–1046, 1993.

[159] J. N. Walford, K. A. Nugent, A. Roberts, and R. E. Scholten, "Three–dimensional phase imaging with a scanning optical–fiber interferometer," *Applied Optics*, vol. **38**, no. 16, pp. 3508–3515, 1999.

[160] T. V. Dolgova, A. I. Maidykovski, M. G. Martemyanov, A. A. Fedyanin, O. A. Aktsipetrov, G. Marowsky, V. A. Yakovlev, and G. Mattei, “Giant microcavity enhancement of second–harmonic generation in all–silicon photonic crystals,” *Applied Physics Letters*, vol. **81**, no. 15, pp. 2725–2727, 2002.

[161] T. V. Dolgova, A. I. Maidykovski, M. G. Martemyanov, A. A. Fedyanin, O. A. Aktsipetrov, G. Marowsky, V. A. Yakovlev, G. Mattei, N. Ohta, and S. Nakabayashi, “Giant optical second–harmonic generation in single and coupled microcavities formed from one–dimensional photonic crystals,” *Journal of the Optical Society of America B*, vol. **19**, no. 9, pp. 2129–2140, 2002.

[162] B. Hecht, Talk: Manipulation of light on the nanometer scale, June 2003.

[163] http://www.photonics.ee.ethz.ch/, November 2003.

[164] R. Wüest, P. Strasser, M. Jungo, F. Robin, D. Erni, and H. Jäckel, “An efficient proximity–effect correction method for electron–beam patterning of photonic–crystal devices,” *Microelectronic Engineering*, vol. **67–68**, pp. 182–188, 2003.

[165] P. Strasser, R. Wüest, F. Robin, D. Erni, and H. Jäckel, “Towards a technology for 2D photonic crystals in InP,” in *Bulletin SPG/SSP, SPS-Annual Meeting*, vol. **20**. Basel: University of Basel, March 2003, p. 87.

[166] W. J. Tropf, T. J. Harris, and M. E. Thomas, *Electro–Optics Handbook*, 2nd ed. McGraw–Hill, 2000, ch. 11. Optical Materials: Visible and Infrared, pp. 11.1–11.82.

[167] R. Wüest, C. Hunziker, F. Robin, P. Strasser, D. Erni, and H. Jäckel, “Limitations of proximity–effect correction for electron–beam patterning of photonic crystals,” *SPIE Proceedings*, vol. **5277**, 2003.

[168] R. Wüest, 2003, private communication.

[169] L. C. Andreani and M. Agio, “Photonic bands and gap maps in a photonic crystal slab,” *IEEE Journal of Quantum Electronics*, vol. **38**, no. 7, pp. 891–898, 2002.

[170] R. D. Winn, Joshua N.and Meade and J. D. Joannopoulos, “Two–dimensional photonic band–gap materials,” *Journal of Modern Optics*, vol. **41**, no. 2, pp. 257–273, 1994.

[171] P. I. Borel, L. H. Frandsen, M. Thorhauge, A. Harpøth, Y. X. Zhuang, M. Kristensen, and H. M. H. Chong, “Efficient propagation of TM polarized light in photonic crystal components exhibiting band gaps for TE polarized light,” *Optics Express*, vol. **11**, no. 15, pp. 1757–1762, 2003.

[172] K. W. Rauscher, 2004, private communication.

[173] M. Hammer, http://wwwhome.math.utwente.nl/˜hammer/, September 2003.

[174] M. Lončar, T. Doll, J. Vukčović, and A. Scherer, “Experimental and theoretical confirmation of Bloch–mode light propagation in planar photonic crystal waveguides,” *Journal of Ligthwave Technology*, vol. **18**, no. 10, pp. 1402–1411, 2000.

[175] S. Vorndran, “Tracking nanoposition advances,” *Photonic Spectra*, pp. 90–97, March 2003.

[176] M. Schmidt, G. Boettger, C. Liguda, A. Petrov, K. Mellert, M. Eich, M. Huebner, W. Morgenroth, and H. G. Meyer, “Tunable polymer photonic crystals,” in *Linear and Nonlinear Optics of Organic Materials III*, ser. Proceedings of the SPIE The International Society for Optical Engineering, M. G. Kuzyk, M. Eich, and R. A. Norwood, Eds., vol. **5212**. Piscataway, NJ: IEEE, November 2003, pp. 171–183.

[177] G. Böttger, C. Liguda, M. Schmidt, and M. Eich, “Improved transmission characteristics of moderate refractive index contrast photonic crystal structures,” *Applied Physics Letters*, vol. **81**, no. 14, pp. 2517–2519, 2002.

[178] M. Schmidt, G. Böttger, C. Liguda, A. Petrov, and M. Eich, “Moderate refractive index photonic crystal slab waveguides,” Poster, 2003.

[179] M. Schmidt, 2003, private communication.

[180] C. Liguda, , G. Böttger, A. Kuligk, R. Blum, M. Eich, H. Roth, J. Kunert, W. Morgenroth, H. Elsner, and H. G. Meyer, “Polymer photonic crystal slab waveguides,” *Applied Physics Letters*, vol. **78**, no. 17, pp. 2334–2436, 2001.

[181] C. M. Wolfe, N. Holonyak, Jr., and G. E. Stillman, *Physical Properties of Semiconductors.* New Jersey: Prentice Hall, 1989.

[182] B. Hecht, H. Bielefeldt, Y. Inouye, D. W. Pohl, and L. Novotny, “Facts and artifacts in near–field optical microscopy,” *Journal of Applied Physics*, vol. **81**, no. 6, pp. 2492–2498, 1997.

[183] E. Betzig and J. K. Trautman, “Near–field optics: Microscopy, spectroscopy, and surface modification beyond the diffraction limit,” *Science*, vol. **257**, no. 5067, pp. 189–195, 1992.

[184] S. I. Bozhevolnyi, “Topographical artifacts and optical resolution in near–field optical microscopy,” *Journal of the Optical Society of America B*, vol. **14**, no. 9, pp. 2254–2259, 1997.

[185] V. Sandoghdar, S. Wegscheider, S. Krausch, and J. Mlynek, “Reflection scanning near–field optical microscopy with uncoated fiber tips: How good is the resolution really ?” *Journal of Applied Physics*, vol. **81**, no. 6, pp. 2499–2503, 1997.

[186] M. Labardi, S. Patanè, and M. Allegrini, “Artifact-free near–field optical imaging by apertureless microscopy,” *Applied Physics Letters*, vol. **77**, no. 5, pp. 621–623, 2000.

[187] N. Y. M. Society, *Glossary of Microscopical Terms & Definitions*, 2nd ed. Microscope Publications, 1989.

[188] K. Aoki, T. Baba, T. Hasegawa, H. Kosaka, M. Koshiba, H. Masuda, H. Misawa, H. T. Miyazaki, S. Noda, M. Notomi, T. Sato, and M. W. Takeda, *Roadmap on Photonic Crystals*, S. Noda and T. Baba, Eds. Boston: Kluwer Academic Publishers, 2003.